UNIVERSITAT POLITÈCNICA DE CATALUNYA BARCELONATECH

Multiscale materials design of hard coatings for improved fracture resistance and thermal stability

Phani Kumar Yalamanchili

In this thesis, I show how to improve fracture resistance and thermal stability of Si, and Al containing transition metal nitride hard coatings, by manipulating the coating structure over multiple length scales.

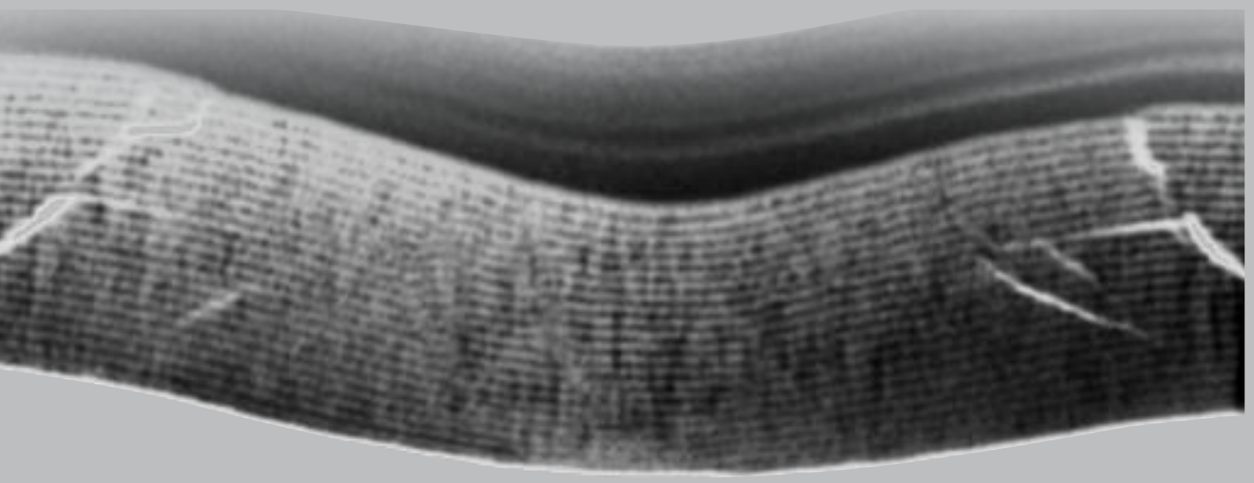

UNIVERSITAT POLITÈCNICA DE CATALUNYA BARCELONATECH

UNIVERSITAT POLITÈCNICA DE CATALUNYA BARCELONATECH

Phani Kumar Yalamanchili

Multiscale materials design of hard coatings for improved fracture resistance and thermal stability

2016

Linköping Studies in Science and Technology
Dissertation No. 1759

Multiscale materials design of hard coatings for improved fracture resistance and thermal stability

Phani Kumar Yalamanchili

UNIVERSITAT POLITÈCNICA DE CATALUNYA BARCELONATECH

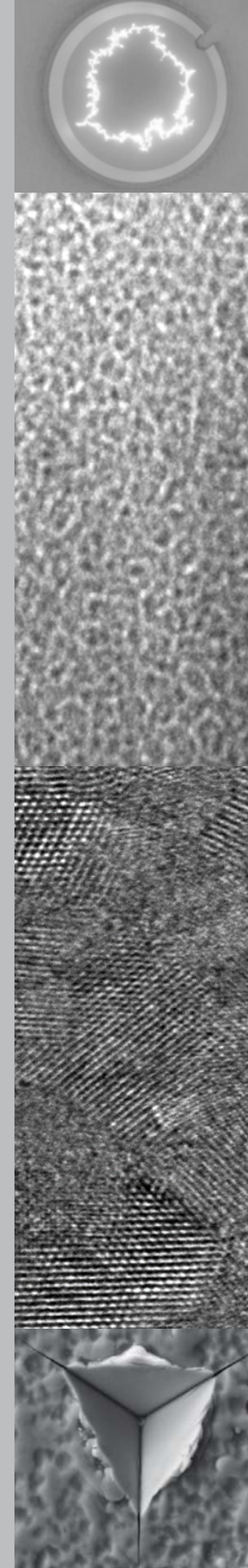

Linköping Studies in Science and Technology

Dissertation No. 1759

Multiscale materials design of hard coatings for improved fracture resistance and thermal stability

Phani Kumar Yalamanchili

LINKÖPING UNIVERSITY

UNIVERSITAT POLITÈCNICA DE CATALUNYA

Departamento de Ciencia de los Materiales e Ingeniería Metalúrgica,
Universitat Politècnica de Catalunya,
08034 Barcelona, Spain.

Part of

the Joint European Doctoral Programme in Materials Science and Engineering (DocMase) in collaboration with

Nanostructured Materials
Department of Physics, Chemistry and Biology (IFM)
Linköping University
SE- 581 83 Linköping, Sweden.

Under the supervision of

Prof. Magnus Odén
Dr. Emilio Jiménez-Piqué

Cover image (top to bottom) shows high speed photograph of arc evaporation of Zr cathode, TEM image and indentation-induced surface cracking of ZrAlN nanocomposite film.

High speed photograph is courtesy of B. Syed

ISBN 978-91-7685-779-3
ISSN 0345-7524
Printed by LiU- Tryck, Linköping 2016

Abstract

Physical vapor deposited hard coatings comprised of cubic (c) transition metal (TM)-Al-N, and (TM)-Si-N are the current workhorse materials for a large number of metal cutting and wear resistant applications to fight against the extreme conditions of temperature and stress simultaneously. In spite of a high degree of sophistication in terms of material choice and microstructural design, a lower fracture resistance and limited thermal stability of the coatings remains a technological challenge in the field. The lower fracture resistance of the coating is an inherent material property. Limited thermal stability in the TM-Al-N system is associated with the transformation of metastable c -AlN to its stable wurtzite (w*)*-AlN phase at a temperature above 900 ^{o}C resulting an undesirable hardness drop.

The current work shows how to overcome these challenges by manipulating the coating material at different length scales, i.e. microstructure, crystal and interface structure, and alloy design. The endeavor of multiscale materials design is achieved by converging a deeper material and process knowledge to result specific structural modification over multiple length scales by alloying transition metal nitrides with AlN and SiN_x as following.

Microstructure variation is achieved in ZrN coating by alloying it with SiN_x, where the surface segregated SiN_x breaks down the columnar structure and evolves a self-organized nanocomposite structure with a hardness variation from 37 ±2 GPa to 26 ±1 GPa. The indentation induced fracture studies reveal crack deflection for the columnar coating, likely along the column boundaries. The crack deflection offers additional energy dissipative mechanisms that make the columnar structured coating more fracture resistant, which is not the case for the nanocomposite coating in spite of its lower hardness.

Crystal structure of AlN is varied between stable wurtzite structure to metastable cubic structure in the ZrAlN alloy by adapting a multilayer structure and tuning the layer thickness. The multilayer consisting c-AlN layer shows a hardness of 34 ±1 GPa and a twofold enhancement in the critical force to cause an indentation induced surface crack compared to the multilayer containing w-AlN in spite of a lower hardness for the later case. The higher fracture resistance is discovered to be caused by stress- induced transformation of AlN from its metastable cubic structure to its thermodynamically stable wurtzite structure associated with a molar volume

expansion of 20% that builds up local compressive stress zones delaying the onset and propagation of the cracks. This is in fact the first experimental data point for the stress-induced transformation toughening in a hard coating.

The current work also demonstrates a concept of improving the thermal stability of the TM-Al-N by modifying the interface structure between w-AlN and c-TMN. A popular belief in the field is that AlN in its stable wurtzite structure is detrimental to coating hardness, and hence the current material design strategy is to force AlN in metastable cubic phase that confines the application temperature (~ 900 °C). In contrast, here it is shown that the w-AlN offers a high hardness provided if it is grown (semi-)coherent to c-TMN. This is experimentally shown for the multilayer system of TiN/ZrAlN. The interface structure between the c-TiN, c-ZrN and w-AlN is transformed from incoherent to (semi-)coherent structure by tuning the growth conditions under a favorable crystallographic template. Furthermore, the low energy (semi-) coherent interface structure between *w*-AlN and c- TiN, c- ZrN display a high thermal stability, causing a high and more stable hardness up to an annealing temperature of 1150 °C with a value of 34± 1.5 GPa. This value is 50 % higher compared to the state-of-the-art monolithic and multilayered Ti-Al-N and Zr-Al-N coating containing incoherent *w*-AlN.

Finally, an entropy based alloy design concept is explored to form a thermodynamically stable solid solution in the TM-Al-N material system that has a positive enthalpy of mixing. Multi-principal element alloys of (AlTiVCrNb)N are formed in a near ideal cubic solid solution. The high configurational entropy in the alloy is predicted to overcome positive enthalpy of mixing, there by an entropy stabilized solid solution formation is expected at a temperature above 1000 K. However, at elevated temperature, optimization between the minimization of interaction energy and maximization of configurational randomness causes precipitation of AlN in its stable wurtzite structure and the cubic solid solution is only confined between TiN, CrN, VN and NbN that have a low enthalpy of mixing.

In summary, this work provides technological solutions to the two outstanding issues in the field. A significant enhancement in fracture resistance of the coating is achieved with appropriate material choice and microstructural design by invoking crack deflection and stress induced transformation toughening mechanisms. A remarkable thermal stability enhancement of the TM-Al-N coating is achieved by a new

structural archetype consisting *c*-TMN and thermodynamically stable *w*-AlN with a low energy (semi-)coherent interface structure.

Populärvetenskaplig sammanfattning

Bakgrund

Material har en avgörande betydelse för nästan all form av ingenjörsvetenskap och teknologi och några exempel från en oändlig lista är nickelbaserade superlegeringar i jetmotorer som tål temperaturer upp till 1400 °C, avancerat högfasthetsstål som räddar passagerares liv vid höghastighetsolyckor, kiselbaserad hybridceller som omvandlar solenergi samt biokompatibla material som ersätter skadade människoorgan. För att framställa dessa material till önskad fysisk form, behövs emellertid bra skärverktyg och detta inte bara för att säkerhetsställa geometrisk precision, utan i större utsträckning för att få de bearbetade materialytorna att kvarstå i sitt bästa möjliga metallurgiska tillstånd. För att tillgodose dessa behov, måste ett skärverktyg kunna motstå extrema förhållanden i termer av att temperaturen och trycket är högt samtidigt. Det i sin tur medför att en fortgående innovation av material för skärverktyg behövs.

För några år gjordes i Sverige upptäckten att skärverktyg belagda med kvävebaserade keramiska beläggningar med en tjocklek på några mikrometer och som är framställda med en teknik som benämns fysisk förångningsdeposition resulterar i en förlängning av verktygets livslängd upp till tio gånger och därtill förbättrades ytintegriteten hos de bearbetade materialen det vill säga att de slutgiltiga komponenterna är mer säkra och pålitliga. Detta förorsakade ett nytt forskningsområde som benämns hårda beläggningar.

Hårda beläggningar som är en blandning av en kubisk (*c*) övergångsmetallnitrid (TMN) och *c*-AlN såsom *c*-Ti-Al-N, *c*-Cr-Al-N och *c*-Zr-Al-N är i dagsläget vanligt förekommande i tillämpningar för skärande bearbetning av metall och för att motstå nötning under de extrema förhållanden som uppstår vid hög temperatur och högt tryck. Trots att framtagningsprocessen av dessa material är förfinad när det gäller materialval samt design av mikrostruktur, kvarstår det ändock tekniska utmaningar och dessa är att förbättra den låga brottsegheten och den begränsade termiska stabiliteten. Brottseghet är en inneboende egenskap hos ett material medan den begränsade termiska stabiliteten leder till att den metastabila fasen *c*-AlN transformeras till den stabila fasen wurtzite (*w)*-AlN och det i sin tur leder till en oönskad minskning av hårdhet vid temperaturer över 900 °C.

Avhandlingens viktigaste bidrag och resultat

Denna avhandling visar hur utmaningarna kan övervinnas genom att en beläggning kan designas på olika längskalor och dessa utgörs av beläggningens mikro-, kristall- och gränsskiktsstruktur och vidare visas hur legeringssammansättningen kan designas. Det åstadkoms genom att kombinera en djupare materialkännedom med djupare förståelse av syntesprocesserna och i kontexten för denna avhandling innebär det att strukturen ändras på olika längdskalor genom att övergångsmetallnitrider legerades med AlN och SiN_x.

För att förbättra motståndskraften mot sprickbildning i en beläggning undersöks två olika yttre mekanismer för att härda ett material och den ena är att avböjda sprickbildningen och den andra är spänningsinducerad fastransformation. Utmaningen består i att initiera dessa mekanismer i beläggningar tunnare än 3 mikrometer. Mikrostrukturen hos beläggningarna varieras mellan en kolumnär struktur och en struktur bestående av nanokompositer genom att kiselinnehållet i legeringen Zr-Si-N anpassas. Den kolumnära strukturen uppvisar en högre motståndskraft mot sprickbildning trots att dessa hårdhet är högre jämfört med strukturen bestående av nanokompositer. Det är en direkt följd av att den förstnämnda strukturen möjliggör avböjning av sprickor och detta sker mest sannolikt längs med korngränserna, vilket resulterar i energidissipation och vidare sker detta inte överhuvudtaget i den sistnämnda strukturen. För att aktivera den spänningsinducerade fastransformationen, varierades kristallstrukturen hos AlN mellan metastabil kubisk fas och termodynamiskt stabil w-AlN i legeringen ZrAlN genom att flerskiktsbeläggningar användes och där skiktens tjocklek avgjorde strukturen. Flerskiktsbeläggningen bestående av lager av *c*-AlN uppvisade en väldigt hög motståndskraft mot sprickbildning trots sina höga hårdhet om 34 ±1 GPa och detta var till följd av fastransformationen från metastabilt w-AlN till stabilt kubiskt AlN under höga materialspänningar. Fastransformation resulterade i en 20 % ökning av molvolymen, vilket i sin tur bygger upp områden med lokala tryckspänningar som fördröjer utbredningen av sprickorna. Detta resultat visas för första gången i denna avhandling.

Vidare i syfte att förbättra den termiska stabiliteten hos TM-Al-N har två olika tillvägagångssätt undersökts och det första är modifiera gränsskikt och den andra är att designa legeringar genom att ändra deras entropi. I forskningsfältet anses det

utbrett att AlN i sin stabila fas är inte är förmånlig för en beläggnings hårdhet och därför har strategin för materialdesign länge varit att växa c-AlN. Här visas motsatsen det vill säga att w-Aln kan vara gynnsamt för hårdheten och det är under förutsättning att det låts växa semikoherent med c-TMN, vilket visas experimentellt for flerskiktsbeläggningssystemet TiN/ZrAlN. Strukturen hos gränsskiktet mellan c-TiN, c-ZrN and w-AlN transformeras från icke koherent till semikoherent genom att flerskiktsbeläggningens arkitektur och tillväxtförhållandena varieras. Det semikoherenta gränsskiktet mellan *c*-TiN, *c*-ZrN och *w*-AlN som har lägre energi uppvisade en högre termisk stabilitet med följden att hårdheten blir högre och håller sig stabil vid värmebehandling upp till 1150 °C och dess värde är 34 ±1,5 GPa. Detta är cirka 50 % högre än vad en tidigare studier visat för värmebehandling vid samma temperatur av monolitiska beläggningar och flerskiktsbeläggningar bestående av TiAlN och ZrAlN och som innehållit *w*-AlN. Avslutningsvis har termodynamiskt stabila fasta TM-Al-N lösningar tagits fram genom att designen av legeringarna baserats på att entropin maximerats. Flerkomponentslegeringen (AlTiVCrNb)N bildas i form av en nästan ideal fast lösning med B1 struktur och som karaktäriseras av konfigurationsslumpmässighet. Emellertid kommer det optimerade tillståndet som uppstår då blandningsentalpin minimeras samtidigt som konfigurationsslumpmässigheten maximeras förorsaka utfällning av *w*-AlN och den fasta lösningen kommer enbart att bestå av TiN, CrN, VN och NbN efter värmebehandling vid hög temperatur.

Sammanfattningsvis bidrar avhandlingen till de tekniska lösningarna av två viktiga problem inom det aktuella fältet. En signifikant förbättring av motståndskraften mot sprickor i beläggningarna har uppnåtts genom lämpligt materialval och design av mikrostruktur har framkallat avböjning av sprickbildning och härdning genom tryckinitierad fastransformation. En märkbar förbättring av den termiska stabiliteten hos TM-Al-N beläggningar har erhållits genom att en ny grundstruktur bestående av *c*-TMN och termodynamiskt stabil *w*-AlN med ett semikoherent gränsskikt med låg energi har tagits fram.

Resumen

Los recubrimientos duros formados por metales de transición (TM) cúbicos -AlN, y -SiN depositados mediante fase de vapor (CVD) son materiales extensamente utilizados en gran número de aplicaciones de corte y de desgaste bajo condiciones extremas de temperatura y solicitaciones mecánicas. A pesar de un alto grado de sofisticación en cuanto a la selección del material y el diseño microestructural, la baja resistencia a la fractura y la limitada estabilidad térmica sigue siendo un importante reto tecnológico. La baja resistencia a la fractura es una propiedad inherente del material. La limitada estabilidad térmica en el sistema TM-AlN está asociada con la transformación de la fase AlN metaestable cúbica (c) a la fase estable wurtzita (w) a una temperatura por encima de 900 ºC, que resulta en una caída de dureza indeseable.

En esta tesis doctoral se muestra como la manipulación del material a diferentes escalas puede ayudar a superar estas dificultades, mediante el cambio microestructural, la estructura cristalina y el diseño de materiales mediante la aleación de nitruros de metal con AlN y SiN_x.

La variación microestructural en los recubrimientos de ZrN se controla mediante la aleación con SiN_x, ya que la segregación superficial de SiN_x rompe la estructura columnar y evoluciona a un nanocompuesto autoorganizado con una dureza de entre 37 ±2 GPa y 26 ±1 GPa. Las grietas producidas por indentación muestran la existencia de deflexión de grieta, lo que proporciona un mecanismo de disipación de energía adicional, haciendo de este material más resistente a la generación de grieta.

La estructura cristalina del recubrimiento de AlN se varía entre la fase estable wurtzita y la fase cúbica estable ZrAlN mediante el control de la estructura y el espesor de la arquitectura multicapa. El recubrimiento multicapa formado por la fase c-AlN presenta una dureza de 34 ±1 GPa y una resistencia a la generación de grietas por indentación dos veces mayor comparado con el recubrimiento multicapa formado por w-AlN, aunque éste presente una dureza menor. La mayor resistencia a fractura está causada por la transformación inducida por tensión de AlN desde la fase cúbica metaestable a la fase wurtzita termodinámicamente estable acompañada de una expansión molar del 20%, resultando en una generación de tensiones compresivas que retarda la generación y propagación de grietas. Esta es la primera vez que se

reporta la existencia de transformación catalizada por tensión en recubrimientos duros.

En esta tesis también se demuestra el concepto de mejorar la estabilidad térmica de los recubrimientos basados en TM-Al-N mediante la modificación de la estructura interfacial entre las fases w-AlN y c-TMN. En general la existencia de AlN en su fase estable wurtzita puede ser detrimental para la dureza, y por lo tanto se suele depositar el material en la fase cúbica, lo que limita la temperatura de utilización (~ 900 ºC). Aquí se muestra que la fase w-AlN puede ofrecer una gran dureza si crece semi-coherentemente a una fase c-TMN. Esto se muestra experimetnalmente para el sistema multicapa TiN/ZrAlN. La estructura interfacial entre las fases c-TiN, c-ZrN y w-AlN se transforma desde una estructura (semi-)coherente mediante el control de las condiciones de deposición y crecimiento. Además, la interfaz (semi-) coherente de baja energía entre c-TiN, c-ZrN y w-AlN resulta en una alta estabilidad térmica con una dureza mayor de 34± 1.5 GPa y más estable hasta temperaturas de recocido de 1150ºC. Esta dureza es un 50%mayor de la dureza reportada para recubrimientos monolíticos y multicapas de Ti-Al-N y Zr-Al-N que contengan fase incoherente de w-AlN.

Finalmente, el concepto de aleaciones de alta entropía se utiliza para depositar una solución sólida termodinámicamente estable del sistema TM-Al-N que presenta una entalpía de mezcla positiva. Elementos de aleación multi-principales de (AlTiVCrNb)N se utilizan para formar una solución sólida cúbica . La alta entropía configuracional en la mezcla es mayor que la entalpía, por lo que se espera una formación de solución sólida estabilizada a temperaturas mayores de 1000K. Sin embargo, a temperaturas elevadas, la optimización entre la minimización de la energía de interacción y la maximización del desorden configuracional causa la precipitación de AlN en su estructura wurtzita estable, y la solución sólida cúbica está únicamente confinada entre TiN, CrN , VN y NbN que tienen baja entalpía de mezcla.

En resumen, esta tesis presenta soluciones tecnológica a dos retos importantes en el campo. Se consigue una mejora significativa en la resistencia a fractura en los recubrimientos mediante la selección de materiales y el diseño microestructural mediante mecanismos de deflexión de grieta y transformación de fase asistida por tensión. Así mismo, se aumenta la estabilidad térmica de recubrimientos TM-Al-N mediante una nueva microestructura consistente en c-TMN y w-AlN

termodinámicamente estable con una estructura interfacial (semi-)coherente de baja energía.

Preface

This is a summary of my doctoral studies between March 2012 to May 2016 in the framework of the Joint European Doctoral Program in Material Science and Engineering (DocMASE). During these four years the main focus has been to explore the research theme of *multiscale materials design of hard coatings for improved fracture resistance and thermal stability of hard coatings*. The key results are presented in the appended papers and the materials science background is presented in the introduction part.

This work has been performed in the group of Nanostrucured Materials at the Department of Physics, Biology and Chemistry (IFM) at Linköping University, Sweden and the Departamento de Ciencia de los Materiales e Ingeniería Metalúrgica, Universitat Politècnica de Catalunya, Spain, together with SECO Tools AB. The work has been supported by DocMASE, and the Swedish foundation for strategic research (SSF) through the grant Designed Multicomponent Coatings (MultiFilms). This work is a continuation of my Licentiate thesis, *ZrN based Nanostructured Hard Coatings, Structure- Property Relationship* (Licentiate thesis No. 1664, Linköping Studies in Science and Technology (2016)).

Kumar Yalamanchili

Linköping, Sep 2016

Acknowledgements

I would like to thank everyone who supported me along the way, especially my sincere gratitude to:

Magnus Odén, my supervisor, thank you for giving me the opportunity in the group, and for your continuous support for me to understand the dynamics of both Science and life.

Emilio. Jiménez-Piqué, Supervisor at UPC, thank you for all the help during my UPC stay. I really like the way you think about Science, and it always inspires me.

Naureen Ghafoor, my co-supervisor, thank you for helping me to improve the fine details always.

Mats Johansson Jöesaar, thank you for many inputs, from the frustrating FIB lift out to the never understood entropy concepts, and for the depositions at SECO tools.

Jon Andersson, thank you for several depositions at SECO tools, and the very interesting questions you always ask, I will miss them. I hope one day we realize the unfinished business of entropy stabilized hard coatings.

Bilal Syed, You definitely made my PhD more enjoyable with several intense discussions on both Science and life, I will miss them. Thank you for all the help, especially at the end.

Fei Wang, surely you are a fantastic collaborator, I really hope to work with you again. **Ferenc Tasnadi,** I learned from you how to care for Science in spite of troubling situations. Thank you both for teaching me first principle calculation basics.

Isabella Schramm, thank you for teaching me atom probe tomography and for several discussions. I will surely remember the discussions on *behavior similarities between humans and materials*.

Jenifer Barrirero, and **Hisham Aboulfadl** thank you for the nice collaboration in atom probe.

Lina Rogström, you always have answers to many questions, and thank you for all the discussions.

Torkel Stenqvist, thank you for several discussions related to Al processing, I am always amused by your ability to talk on very diverse topics.

Robert Pilemalm, thank you for several inputs on Swedish systems, for the Swedish translation, and being a good friend.

Aylin Atakan, Jennifer Ullbrand, Ana Chaar, Katherine Calamaba, Peter Mäkie, Emma Björk, Eric, My Duong and Klara Asp Grönhagen you definitely made the nanostructured group more pleasant. Thank you for the nice company and several inputs.

Niklas Norrby, Zhu Jianqiang, Axel Knutsson, and Rikard Forsén, I have certainly gained a lot from the solid foundations you laid to deal with the complicated procedures in the lab, from DSC sample preparation to the very sophisticated TEM analysis, thank you.

Kostas Sarakinos, and Sankara Pillay, thank you for all the very interesting discussions on the fascinating structures you have made.

Therese Dannetun, and Thomas Lingefelt, without your technical and administrative support this work will never be finished, thank you.

My **friends** and **colleagues** in **Nanoscale engineering, Plasma& Coating physics, and Thin film** groups, thanks for being very helpful, any time and every time.

Joan Joseph, and **CIEFMA** group members, thank you for helping me during my stay at UPC.

Family and **Friends**, especially my wife **Madhu** for being very kind, patient, and caring during the frustrating periods of PhD.

Finally to all the **visible and invisible people and forces** who made the foundations to demystify the art and science of materials and taught me how to use it for the benefit of the mankind.

Included publications

Paper I

Structure, deformation and fracture of arc evaporated Zr–Si–N hard films

K. Yalamanchili, R. Forsén, E. Jiménez-Piqué, M.P. Johansson Jöesaar, J.J. Roa, N. Ghafoor, M. Odén

Surface & Coatings Technology 258 (2014) 1100–1107

Paper II

Influence of microstructure and mechanical properties on the tribological behavior of reactive arc deposited Zr-Si-N coatings at room and high temperature

K. Yalamanchili, *E.* Jiménez-Piqué, L. Pelcastre, KD Bakoglidis, J.J. Roa, M. P. Johansson Jöesaar, B. Prakash, N. Ghafoor and M. Odén

Surface & Coatings Technology 304 (2016) 393 – 400

Paper III

Tuning hardness and fracture resistance of $ZrN/Zr_{0.63}Al_{0.37}N$ nanoscale multilayers by stress-induced transformation toughening

K. Yalamanchili, I.C. Schramm, E. Jiménez-Piqué , L. Rogström, F. Mucklich, M. Odén and N. Ghafoor

Acta Materialia 89 (2015) 22–31

Paper IV

Growth and thermal stability of TiN/ZrAlN: Effect of internal interfaces

K. Yalamanchili, F. Wang, H. Aboulfadl , J. Barrirero , L. Rogström , E. Jiménez-Pique , F. Mücklich , F. Tasnadi, M. Odén, N. Ghafoor

Accepted in Acta Materialia

Annexure I

Exploring high entropy alloy concept in (AlTiVNbCr)N alloy

K. Yalamanchili, F. Wang, I.C. Schramm, J.M. Andersson, M. P. Johansson Jöesaar, F. Tasnadi, N. Ghafoor, and M. Odén

Submitted

Related but not included paper

Annexure II

Intrinsic size effects and role of coherent interfaces on pre- and post- yield behavior of TiN/ZrAlN nanolaminates in micropillar compression.

N. Ghafoor, K. Yalamanchili, C. Davis, W.J. Clegg, J. Barrirero, F. Mücklich, M. Odén

In manuscript

Contributions to the included publications

All the papers included in this thesis, I took major part in designing, and depositing the coatings. I have done all the structural characterization (except APT), mechanical property evaluation of the coatings, and finally I wrote first draft of all the papers.

Symbols and abbreviations

a	Lattice parameter
B	Bulk modulus
b	Interatomic distance
BF	Bright-field
C	Cubic structure
c	length of the crack
CVD	Chemical vapor deposition
d_0	Strain-free plane spacing
d_{hkl}	Plane spacing for *hkl* planes
DSC	Differential scanning calorimetry
E	Elastic modulus
EDS	Energy dispersive x-ray spectroscopy
ERDA	Elastic recoil detection analysis
FIB	Focused ion beam
G	Gibbs free energy
H	Hardness
ΔH	Enthalpy of mixing
HAADF	High angle annular dark field
HEA	High entropy alloy
hkl	Miller index
H_{mix}	Enthalpy of mixing
HR	High-resolution
h_t	Total penetration depth
I	Intensity
k_{Ic}	Fracture toughness in crack I mode opening
P	Load
PVD	Physical vapor deposition
S	Contact stiffness
SITT	Stress induced transformation toughening
S_{mix}	Entropy of mixing
$S_{config.}$	Configurational entropy of mixing
$S_{vib.}$	Vibrational entropy of mixing
SEM	Scanning electron microscopy

STEM	Scanning transmission microscopy
T	Temperature
TEM	Transmission electron microscopy
TG	Thermogravity
XRD	X-ray diffraction
W	Wurtzite structure

α	Indenter constant
ε	Strain
2θ	Scattering angle
λ	Wavelength
ν	Poisson ratio
σ	Stress
ϕ	Rotation angle
ψ	Tilt angle

Table of contents

1.Introduction to hard coatings and open questions to the current work

Coatings extend the capabilities of bulk form materials by rendering new structural, functional and mechanical properties. Hard coatings are a few micron (5-20 um) thin overlay of refractory materials with a typical hardness of 30 - 50 GPa. Whether it is noticed or not, these coatings are regularly applied on precision component and tool surfaces with an objective to enhance their durability, to reduce the frictional force, and most importantly to enhance the surface quality of the work piece.

1.1 History of hard coatings

The field of hard coatings began around 1969 when Krupp & Sandvik almost simultaneously witnessed a significant enhancement in chemical and abrasive wear resistance of metal cutting tool by applying few micron thin coating of TiC, deposited by thermally activated chemical vapor deposited (CVD) process. This had an immediate influence on the cutting tool industry [1]. However, the coatings suffered from undesirable tensile residual stresses, micro cracks and substrate embrittlement due to a high growth temperature of thermal CVD process (> 900 ^{o}C). Furthermore, the high growth temperature has restricted the free choice of the tool material. To overcome these challenges, a brand new TiN coating processed by physical vapor deposited (PVD) process at a temperature less than 500 ^{o}C was introduced around 1982 which soon became the industrial standard for sharp and tough cutting edge [2].

1.2 Material Science of PVD hard coatings and open questions

Plasma based PVD processes such as magnetron sputtering and arc deposition techniques form coatings with a predicted quench rate of 10^{10} K/s at the growth front. The cooling rates are at least seven fold higher compared to the typical bulk form metallurgical processes [3]. A high degree of non-equilibrium processing conditions combined with the compositional freedom of PVD process have resulted in an explosion of new coating materials. Today in the market there are at least 100

different coating options [4] consisting of a wide range of refractory materials such as nitrides, carbides, borides and oxides. Here, the discussion is confined only to nitride hard coatings which can be broadly classified into three categories as schematically shown in Fig. 1.1, (a) metastable cubic solid solution of transition metal (TM)-Al-N, (b) nanocomposite structure in (TM)-Si-N, and (c) nanoscale multilayer.

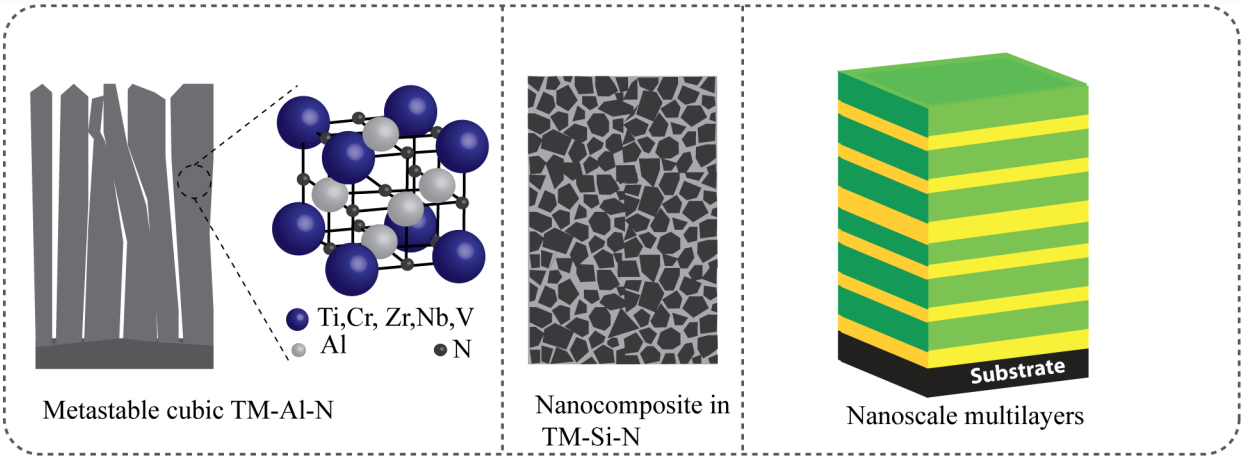

Figure 1.1. Schematic representation of material design in nitride hard coatings

1.2a Metastable c-TM-Al-N:

Metastable c-Ti-Al-N, and c-Cr-Al-N coatings are backbone for several tooling applications. Even though AlN is immiscible to c-TiN, and c-CrN with mixing enthalpy between 0.06 and 0.2 eV/atom [5,6], the kinetically limited growth conditions in the PVD process form a metastable cubic solid solution up to 70 at. % of Al [7,8]. The combined effect of superior oxidation resistance [9] and high hardness of the cubic solid solution in the range of 30 - 35 GPa results in superior wear resistance [10]. In addition, the metastable cubic solid solution displays a self-hardening behavior in $Ti_{0.33}Al_{0.67}N$ coating [11] at a temperature between 800 °C and 900 °C. This is a direct consequence of formation of a self-organized nanoscale isostructural domains of c-TiN, and metastable c-AlN in a coherent lattice with spatial fluctuation in shear modulus [11].

However, at elevated temperature above 900 °C which is the working temperature for several cutting and forming applications, AlN assume its thermodynamically stable wurtzite structure [11,12]. The w-AlN phase formation has been reported to cause material softening [11,12] that leads to an accelerated abrasive wear of the

coating at elevated temperature[13,14]. This issue of limited thermal stability of metastable c-TM-Al-N coatings is a long standing challenge both from scientific and application point of view which is an open question to the current work.

1.2b Nanocomposite Ti-Si-N:

Veprek et al., have proposed that when a highly immiscible material system such as TiN and SiN_x with Gibbs free energy of mixing around 3 - 4 eV/atom are co-deposited under appropriate growth conditions, the SiNx gets surface segregated during the growth [15]. This causes breakdown of the columnar structure and instead evolves into a self-organized nanocomposite structure consisting of 5 nm TiN crystals wrapped by a monolayer thick SiN_X phase as shown in Fig. 1.1 [15]. The nanocomposite of Ti-Si-N has been reported to have a hardness higher than 40 GPa which is attributed to the combined effect of (a) confined dislocation motion in the nanoscale crystals, and (b) simultaneously suppressing grain boundary mediated deformation mechanism by the SiN_x tissue phase [15–17]. Following this success, several other Me-Si-N systems such as, W-Si-N [18], Zr-Si-N [19], Cr-Si-N[20] and Al-Si-N [21] are explored for similar hardness enhancement. Even though a nanocomposite structure could be achieved in a wide range of Me-Si-N systems, the hardness enhancement is missing for some systems, for example Zr-Si-N[19] which remains as an open question.

1.2c Nanoscale multilayer:

Nanoscale multilayer consists of alternate layers of two different materials. When the multilayers are formed with an optimal material selection and layer thickness (~ 2 and 10 nm), a hardness of more than 40 GPa can be achieved. Successful examples are TiN/VN [22], TiN/NbN [23], and CrN/AlN [24]. Even though the hardness enhancement in a multilayer structure is a well-known phenomenon, it is not known how the layered architecture affects the fracture resistance which is explored in the current work.

Hard coatings often display brittle behavior, and the typical fracture toughness (K_{IC}) of nitride coatings(CrN, CrN/Si_3N_4) is only about 2.5 MPa$\sqrt{m}$ [25,26]. This is an inherent material characteristic associated with strong ionic and covalent bonding between metallic and nonmetallic atoms. By increasing the free metallic content in

the alloy, the fracture toughness of the coating may be enhanced, but with a significant drop in hardness, as observed in the case of alloying Ni to Ti-Si-N [27]. Hence the challenge is to achieve higher fracture resistance without any compromise in the hardness value.

For the bulk form ceramic materials this task is typically achieved by activating extrinsic toughening mechanisms involving crack deflection and crack tip shielding. These energy dissipative mechanisms reduce the driving force for crack propagation that leads to enhanced fracture toughness, and K_{IC} values even up to 30 MPa$\sqrt{m}$ has been claimed [28]. However, activating such extrinsic toughening mechanisms in few micron thin nitride coating is a challenging task which is explored in the current work.

In summary, lower fracture resistance of hard coatings, and limited thermal stability of the TM-Al-N coatings are the open questions to the current work. The following two examples illustrate an urgent need to solve these material challenges.

1.3 Case studies

1.3a Case 1: Surface integrity of machined components: Figure 1.2b shows a cross-sectional view back scattered scanning electron micrograph (SEM) revealing microstructural modification of Inconel 718 alloy after a broaching operation.

The SEM micrograph reveals severe plastic deformation near surface and subsurface regions. A high magnification micrograph (not shown here) reveal microcracks and depletion of nanoscale coherent precipitates of γ''(Ni_3Nb)[29]. Residual stress measurement reveals tensile stresses on the deformed surface region.

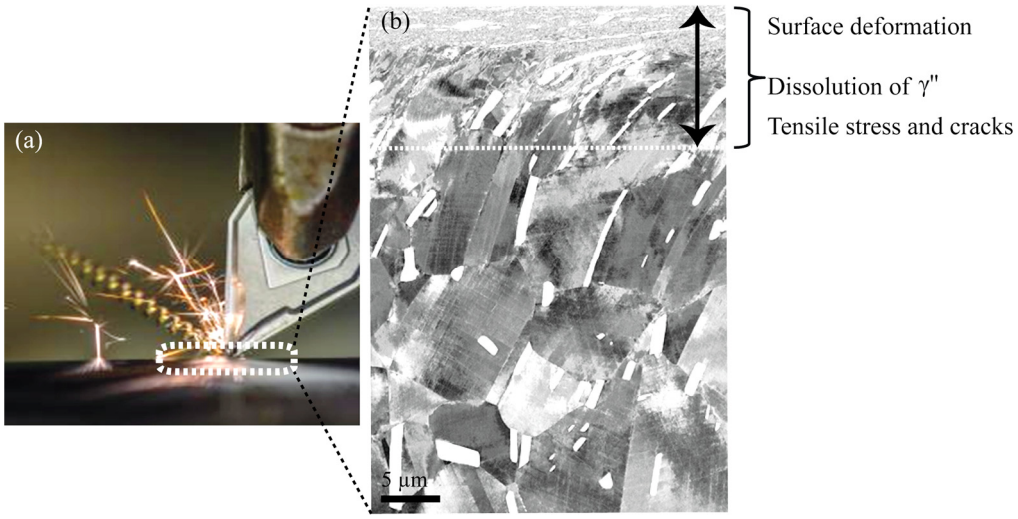

Figure 1.2(a) metal cutting, and corresponding (b) cross-sectional view back scattered electron micrograph of work piece (Inconel 718 alloy) revealing surface and subsurface microstructural modification. Image: courtesy of Zhe Chen.

In summary, the Inconel 718 alloy intended for the gas turbine disc application has undergone significant metallurgical destruction on the surface and the subsurface region caused by the broaching operation. Similarly, machining is the final stage of the manufacturing cycles for several other critical components, and any surface damage at this stage may lead to premature component failure with a high penalty. A possible solution to this problem is to keep the cutting edge sharper for a long time by increasing the thermal stability of the coating.

1.3b Case 2: Poor fracture resistance and cohesive failure of the coating:

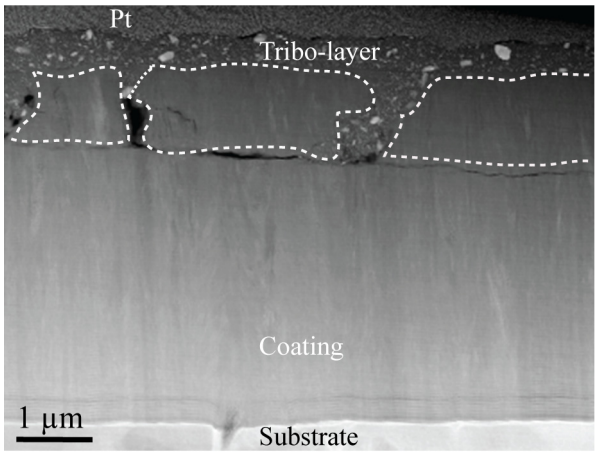

Figure 1.3. Cross-sectional view TEM micrograph of Zr-Si-N coating, after subjecting to wear test.

Figure 1.3 shows a cross-sectional view electron micrograph of Zr-Si-N coating, after subjecting to reciprocating sliding wear at a temperature of 500 °C. The micrograph reveals several vertical and lateral cracks causing coating delamination, and massive coating material loss. Furthermore, the fragmented pieces of coating may act as a source of abrasive particles which results in tool destruction and impaired product surface quality. This is a more severe problem for forming tools as the fragments are continuously recycled [30]. A high fracture resistance of the coating is desired to overcome these issues.

1.4 Aim and outline of the thesis

State-of-the-art hard coatings are characterized with lower fracture resistance and limited thermal stability in the TM-Al-N alloys. This thesis explores technical solutions to both these issues by manipulating the coating material at different length scale, i.e. microstructure, crystal and interface structure, and alloy design. The endeavor of multiscale materials design is achieved by converging a deeper material and process knowledge to result specific structural modification over multiple length scales by alloying transition metal nitrides with AlN and SiN_x.

This thesis consists of two parts. The first part includes an introduction to hard coatings, open questions, material science background, materials and methods, and finally the summary, and proposed future work. The second part contains appended papers.

References:

[1] H.M. Ortner, P. Ettmayer, H. Kolaska, The history of the technological progress of hardmetals, Int . J Refract Metals Hard Mater 44 (2014) 148-159.

[2] M. Sjiistrand, Advances in coating technology for metal cutting tools, Metal Powder Report (2001) 24-30.

[3] M. Ohring, Materials Science of Thin Films 2 nd edition, Academic Press (2001).

[4] K.J. Brookes, A. Lümkemann, PLATIT – pioneers in physical vapour deposition, Met. Powder Rep. 68 (2013) 24–27.

[5] B. Alling, T. Marten, I.A. Abrikosov, A. Karimi, Comparison of thermodynamic properties of cubic Cr1-x Alx N and Ti1-x Alx N from first-principles calculations, J. Appl. Phys. 102 (2007) 044314.

[6] D. Holec, R. Rachbauer, L. Chen, L. Wang, D. Luef, P.H. Mayrhofer, Surface & Coatings Technology Phase stability and alloy-related trends in Ti – Al – N , Zr – Al – N and Hf – Al – N systems from first principles, Surf. Coat. Technol. 206 (2011) 1698–1704.

[7] T. Ikeda, S. Satoh, Phase formation and characterization of hard coatings in the Ti-Al-N system prepared by the cathodic arc ion plating method, Thin Solid Films. 195 (1991) 99–110.

[8] A.E. Reiter, V.H. Derflinger, B. Hanselmann, T. Bachmann, B. Sartory, Investigation of the properties of Al1-xCrxN coatings prepared by cathodic arc evaporation, Surf. Coatings Technol. 200 (2005) 2114–2122.

[9] Y.C. Chim, X.Z. Ding, X.T. Zeng, S. Zhang, Oxidation resistance of TiN, CrN, TiAlN and CrAlN coatings deposited by lateral rotating cathode arc, Thin Solid Films. 517 (2009) 4845–4849.

[10] A. Inspektor, P.A. Salvador, Architecture of PVD coatings for metalcutting applications: A review, Surf. Coatings Technol. 257 (2014) 138–153.

[11] P.H. Mayrhofer, A. Hörling, L. Karlsson, J. Sjölén, T. Larsson, C. Mitterer, L. Hultman, Self-organized nanostructures in the Ti-Al-N system, Appl. Phys. Lett. 83 (2003) 2049–2051.

[12] H. Willmann, P.H. Mayrhofer, P.O.Å. Persson, A.E. Reiter, L. Hultman, C. Mitterer, Thermal stability of Al – Cr – N hard coatings, Scr. Mater. 54 (2006) 1847–1851.

[13] A. Höling, L. Hultman, M. Odén, J. Sjölén, L. Karlsson, Mechanical properties and machining performance of Ti1-xAlxN-coated cutting tools, Surf. Coatings Technol. 191 (2005) 384–392.

[14] A. Knutsson, M.P. Johansson, L. Karlsson, M. Odén, Thermally enhanced mechanical properties of arc evaporated Ti 0.34Al0.66 N/TiN multilayer coatings, J. Appl. Phys. 108 (2010) 0–7.

[15] S. Veprek, Recent search for new superhard materials : Go nano ! J. Vac. Sci. Technol. A. 31(2014) 050822.

[16] J. Patscheider, T. Zehnder, M. Diserens, Structure-performance relations in nanocomposite coatings, Surf. Coat. Technol. 146 (2001) 201–208.

[17] J. Patscheider, Nanocomposite Hard Coatings for Wear Protection, MRS bulletin. March (2003) 180–183.

[18] T. Fu, Z.F. Zhou, K.Y. Li, Y.G. Shen, Structure, stress and hardness of sputter deposited nanocomposite W-Si-N coatings, Surf. Coatings Technol. 200 (2005) 2525–2530.

[19] M. Nose, W. A. Chiou, M. Zhou, T. Mae, M. Meshii, Microstructure and mechanical properties of Zr–Si–N films prepared by rf-reactive sputtering, J. Vac. Sci. Technol. A. 20 (2002) 823.

[20] G. Zhang, L. Wang, S.C. Wang, P. Yan, Q. Xue, Structure and mechanical properties of reactive sputtering CrSiN films, Appl. Surf. Sci. 255 (2009) 4425–4429.

[21] A. Pélisson, M. Parlinska-Wojtan, H.J. Hug, J. Patscheider, Microstructure and mechanical properties of Al–Si–N transparent hard coatings deposited by magnetron sputtering, Surf. Coatings Technol. 202 (2007) 884–889.

[22] U. Helmersson, S. Todorova, S.A. Barnett, J.E. Sundgren, L.C. Markert, J.E. Greene, Growth of single-crystal TiN/VN strained-layer superlattices with extremely high mechanical hardness, J. Appl. Phys. 62 (1987) 481–484.

[23] M. Shinn, L. Hultman, S.A. Barnett, Growth, structure, and microhardness of epitaxial TiN / NbN superlattices, J. Mater. Res. 7 (1992) 901-911.

[24] J.K. Park, Y.J. Baik, The crystalline structure, hardness and thermal stability of AlN/CrN superlattice coating prepared by D.C. magnetron sputtering, Surf. Coatings Technol. 200 (2005) 1519–1523.

[25] A. Wang, G. Yu, J. Huang, Fracture toughness measurement on TiN hard coatings using internal energy induced cracking, Surface & Coatings Technology. 239 (2014) 20–27.

[26] S. Liu, J.M. Wheeler, P.R. Howie, X.T. Zeng, J. Michler, W.J. Clegg, Measuring the fracture resistance of hard coatings, Appl. Phys. Lett. 102 (2013) 1–5.

[27] S. Zhang, D. Sun, Y. Fu, Y.T. Pei, J.T.M. De Hosson, Ni-toughened nc-TiN/a-SiNx nanocomposite thin films, Surf. Coatings Technol. 200 (2005) 1530–1534.

[28] A.G. Evans, Perspective on the Development of high-toughness ceramics, J. Am. Ceram. Soc. 73 (1990) 187–206.

[29] Z. Chen, Surface Integrity of Broached Inconel 718 and Influence of Thermal Exposure, Licentiate thesis No.1676, Linköping 2014.

[30] B. Podgornik, S. Hogmark, O. Sandberg, Hard Pvd Coatings and Their Perspectives in Forming Tool Applications, Proceedings of the 6 th International Tooling Conference- The use of Tool Steels: Experience and Research (2002) 881-891.

2. Multiscale materials design to improve hardness and fracture toughness

Following chapter provides a brief introduction to various strengthening and toughening mechanisms induced by manipulating the coating material at different length scales, i.e. microstructure, crystal and interface structure, and alloy design.

2.1 Hardness

Hardness is a measure of resistance to the localized plastic deformation of a material. Indentation induced plastic deformation in cubic transition metal nitride (TMN) coatings is carried by dislocation glide on the slip system of {110} <1-10> at room temperature [1]. The gliding dislocation can be hindered both by intrinsic and extrinsic barriers. Intrinsic barriers include consequential breakage and remake of an electron pair bond at the core of dislocation, known as *Peierls-Nabarro* stress [2]. Whereas the extrinsic barriers includes several micro- and nanoscale features. Following section provides a brief introduction to several strengthening mechanisms at various length scales both by intrinsic and extrinsic factors related to the current work.

2.1a. Microstructure (grain size):

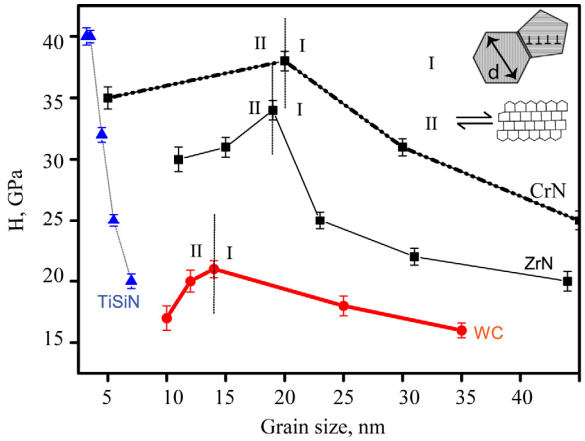

Figure 2.1. Hardness variation as a function of grain size for various TMN coatings. Data is taken from [7–9]. Inset image schematically represents the likely deformation mechanisms in region I and II.

The word microstructure is a broad term that includes several microscale features such as, grain size, morphology and precipitates etc. Here, it is confined to the grain size effects which could be systematically tuned either by changing the coating growth conditions, [3] or by the selective alloy addition as shown in paper I.

About Sixty years ago, Hall [4] and Petch [5] have independently found that the strength of mild steel can be enhanced significantly by simply reducing the grain size.

This has led to an important observation that grain boundaries are effective obstacles to the dislocation glide, with an inverse square root relation between the yield strength and grain size ($\sigma_y \propto d^{-½}$) for a wide range of materials. Figure 2.1 shows the hardness variation as a function of grain size for several TMN coatings displaying a typical Hall-Petch behavior in region I. However, when the grain size is less than a critical value, the material softens with an inverse Hall-Petch relationship as shown in Fig. 2.1 region II. For TM nitrides and carbides the transition from region I to II is typically observed at a grain size of 15- 20 nm. This has been attributed to the transition in deformation mechanisms, i.e. switching from dislocation mediated plasticity to grain boundary mediated plasticity [6].

In contrast to this, Ti-Si-N nanocomposite coatings [9] display grain size strengthening even up to 3 nm with a steep increase in the hardness as shown in Fig. 2.1. This has been attributed to the high interface strength between TiN and SiNx, suppressing grain boundary sliding [9]. Based on this idea, Zr-Si-N nanocomposite coatings are grown in paper I and the grain size strengthening effects are investigated by probing indentation induced deformation mechanisms as a function of grain size variation.

2.1b. Microstructure (multilayer architecture):

Coatings can be grown either with a uniform composition (monolithic) or in the form of multilayer consisting alternative layers of different materials. Interestingly, for several multilayer systems hardness can be tuned as a function of their layer thickness with three distinct regions (Fig 2.2). Region I in Fig. 2.2 shows the inverse relation between hardness and layer thickness up to about 15 nm, where the layer interfaces are likely to offer boundary strengthening similar to the Hall-Petch type behavior. In contrast, region II displays a sharp rise in hardness at a layer thickness between 3 and 5 nm, but only for selective material systems such as TiN/VN, and TiN/NbN (Fig. 2.2).

Several mechanisms have been proposed to explain the strengthening effects in region II such as, metastable phase formation, coherency strengthening and Koehler strengthening [10,11], but it is agreed that Koehler strengthening is primarily responsible for this phenomenon [12]. According to Koehler, when a dislocation glides through the multilayer with difference in shear modulus, it experiences a

repulsive force from the layer with high shear modulus and the dislocations are essentially trapped in the layer with lower shear modulus [13]. This results in material strengthening, provided the layers are sufficiently thin enough to prevent the operation of new dislocation sources [13].

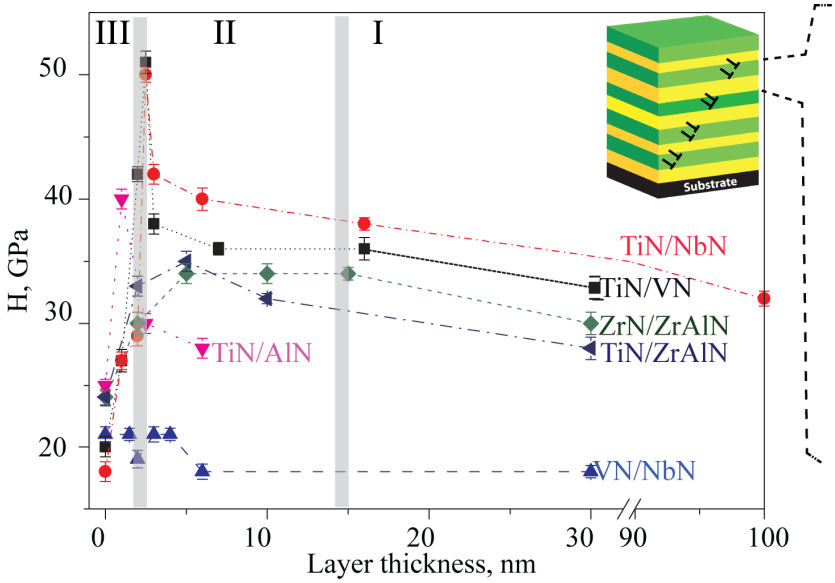

Material system	ΔGb², %
c-TiN/c-NbN	9
c-TiN/c-VN	18
c-TiN/c-AlN	15
c-VN/c-NbN	3
c-ZrN/w-AlN	50

Figure 2.2. Hardness variation as a function of layer thickness, data is taken from [14–17]. *Difference in the value of Gb^2 between different layers in the multilayer.*

Figure 2.2 shows the difference in the dislocation line energy in the multilayer which is proportional to ΔGb^2 between the two different layers, where G is shear modulus and b is burgers vector. The multilayer of VN/NbN displays the lowest ΔGb^2 with a value of 3%, and explains why this material system does not show hardness enhancement. On the other hand, the multilayer of TiN/VN shows relatively higher ΔGb^2 with a value of 18% explaining their high hardness. The estimation shows a highest value of ΔGb^2 (50 %) for the multilayer of c-ZrN/w-AlN. Based on this observation, in paper III it is expected that the multilayer of ZrN/ZrAlN, consisting nanoscale domains of (semi-) coherent c-ZrN and w-AlN display a significant hardness enhancement. In contrast to this prediction, these multilayers show only moderate hardness enhancement (Fig. 2.2), and the reason for this anomaly is not known.

Finally in region III (Fig. 2.2), when the layer thickness is lower than 3nm, the chemical intermixing at layer interfaces becomes prominent that dilutes the fluctuations in shear modulus causing a lower Koehler strengthening. More detailed results about the chemical intermixing at the layer interfaces are presented in paper IV.

Metallic multilayers also display a layer thickness dependent flow stress variation similar to what has been shown in Fig. 2.2 [18]. A. Misra et al., have attributed the flow stress variation to the layer thickness dependent deformation mechanisms [18], i.e. a dislocation pileup based Hall-Petch model at sub-micrometer length scales. This is followed by a confined layer slip of single dislocation at a layer thickness between few tens of nanometer and few nm, where the flow stress reaches the maximum value. Finally, when the layer thickness is less than the critical value (~ 2 nm) the material softens as a consequence of interfaces cutting. i. e. interface barrier to slip transmission decreases as the dislocation core dimension approaches the layer thickness. Nevertheless, it is not known if similar layer thickness dependent deformation behavior is also active in TMN coatings.

2.1c. Crystal and interface structure:

Crystal structure defines the specific and unique geometrical pattern of atomic arrangement in a material, which influence the material hardness by modifying the slip system, burgers vector and frictional stress for dislocation motion. BN is a classic example, where by changing the crystal structure from hexagonal to cubic structure modifies its application scope from a soft lubricant to a hard cutting tool. For the bulk form materials, most often such structural transformations can only be achieved under extreme conditions of pressure and temperature [19]. However, the non-equilibrium processing conditions and size confinement effects in the PVD process enable similar structural transformation even at ambient conditions[20]. Well known examples are coatings consisting of TaN and AlN displaying a higher hardness when they are formed in metastable cubic structure compared to their thermodynamically stable hexagonal structure [21,22]. Nevertheless, recent studies suggest that the hardness enhancement is not an inherent effect of metastable phase formation, but a consequence of the modified interface structure in the material [23].

Interface implies to a boundary between two different phases in a material. For the PVD coatings, the key microstructural feature is often few tens of nanometers, causing a significantly higher volume fraction of interfaces. For example, at a grain size of 5 nm, the volume fraction of atoms located near the interfaces can be as high as 50 % [24]. As a consequence of this, the interface structure plays a dominant role in determining the mechanism of plastic deformation [25], thereby the hardness of the coating.

Figure 2.3 schematically illustrates two different type of interface structures and their likely deformation mechanisms. Incoherent interfaces do not have any continues atomic registry across the boundary, which make them weak in shear. This favors interface mediated deformation by causing sliding along the interfaces, when the interface volume is sufficiently high, as shown in Fig. 2.3a. This generates regions of high plasticity that leads to a reduced hardness similar to what has been observed for Zr-Si-N nanocomposite coating in paper I. In contrast, a continuous atomic registry of the coherent interfaces (Fig. 2.3b) make them more resistant to shear sliding, instead dislocation driven plasticity is favored. Furthermore, a difference in shear modulus across the coherent interface generates Koehler strengthening [13] and the structural misfit across the interface generate coherency strengthening [26] causing a higher hardness. This aspect of hardness enhancement by modifying the interface structure in a nanostructured material is explored in paper IV, to solve a long standing challenge of limited thermal stability in the TM-Al-N coatings which is presented in chapter 6.

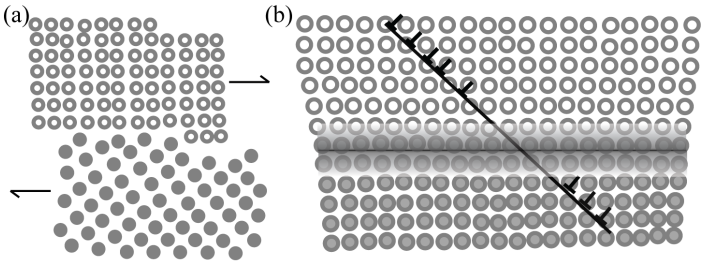

Figure 2.3. Schematic illustration: (a) incoherent interface and interface mediated deformation, and (b) coherent interface and dislocation mediated plasticity.

2.1d. Alloy design:

Hardness enhancement of several TMN coatings as a function of solute concentration is shown in Figure. 2.4, the data points are selectively taken, where the hardness enhancement is primarily attributed to solid solution strengthening. It is evident that Si offers a significantly higher solid solution strengthening compared to Al. However, it is not known whether the hardness enhancement is an intrinsic or extrinsic effect.

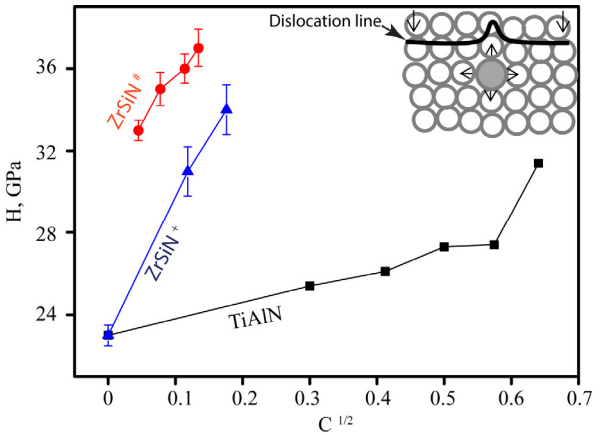

Figure 2.4. Hardness variation of TMN coatings as a function of square root of solute concentration $C^{0.5}$ [29,30]. Coatings grown by sputtering^{+} and cathodic arc evaporation$^{\#}$. Inset image schematically illustrates the dislocation-solute interaction.

Intrinsic factors include solute-induced local change of chemical bonding and valance electron concentration (VEC). Solute atoms that form covalent bonding and an optimal VEC [27] are shown to increase frictional stress for the dislocation glide. While the extrinsic factors include modulus and size effects. The former is caused by a difference in shear modulus (G), while the later is caused by size mismatch between the solute and the host lattice creating either a spherical or tetragonal lattice distortion. Spherical distortion effectively interacts with only edge dislocation, while the tetragonal distortion interact with both edge and screw dislocation resulting significantly higher hardness [28]. For metals, the tetragonal distortion can only be induced by interstitial solute elements, such as carbon in iron. In contrast, for ceramic materials the tetragonal distortions are reported even for substitutional solid solution, such as divalent solute ions in a monovalent ionic crystal [28]. Perhaps, similar effects might be possible in TMN alloys.

An important limitation to solid solution strengthening is that the solute element creating a high lattice distortion is also likely to have a lower solid solubility under equilibrium conditions and thus not suitable for elevated temperature applications. To address this issue, an entropy based alloy design [31] is explored in paper V. The idea is to form an entropy stabilized solid solution between the elements with a significant atomic size difference that leads to a high solid solution strengthening and high hardness at elevated temperature, further details are presented in chapter 7.

2.2 Fracture toughness

Toughness is the ability of a material to resist both crack initiation and propagation, while fracture toughness (K_{IC}) is the ability to resist crack propagation. TMN coatings display a generic inverse relationship between hardness and fracture toughness in spite of a high degree of sophistication in terms of material choice and microstructural design as illustrated in Fig. 2.5. Hence, the challenge in the current work is to improve fracture toughness without sacrificing hardness.

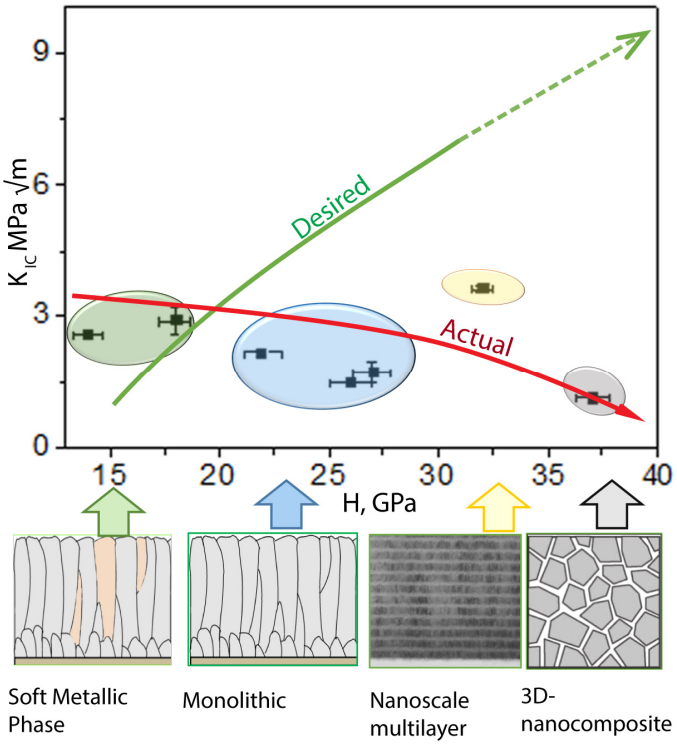

Figure 2.5. Fracture toughness (K_{IC}) variation as a function of hardness enhancement for different TMN monolithic and multilayer coatings. Data points are taken from [33–36]

The development of hard coatings with enhanced fracture resistance has remained as a challenging task, one of the reasons is the difficulty in getting a reliable K_{IC} value in a few micron thin coating. Recently, several techniques have been proposed to measure reliable K_{IC} values of these coatings, further details are presented in chapter 5. The K_{IC} values of typical hard coatings, such as TiN, CrN, and CrN/Si_3N_4 have been reported between 1.2 and 3.3 MPa√m indicating that they are highly brittle [32,33]. This work explores several toughening mechanisms by modifying the coating material across multiple length scales, i.e. microstructure and crystal structure.

The following section provides a brief introduction to several intrinsic and extrinsic toughening mechanisms relevant to the current work. Intrinsic toughening mechanisms are inherent material property induced by changes in electronic structure and chemical bonding. Recent studies have shown that the toughness of TMN alloys could be varied by tuning the valence electron concentration. For example, alloying of TaN, MoN and WN to CrN, TiN and VN have been reported to cause weakening of Me-N bonds across the slip plane, thereby an enhanced plasticity and fracture resistance [37–40].

In contrast, extrinsic toughening mechanisms operate along the crack front with the primary objective of reducing the driving force for the crack growth.

2.2a. Ductile phase toughening:

A ductile phase is included in the hard coating to relax the stress field in the vicinity of the crack tip. It has been shown that the Ni addition to Ti-Si-N coating increases the K_c from 1.15 MPa √m to 2.6 MPa √m but with a significant drop in the hardness value from 30 GPa to 15 GPa [41].

2.2b. Crack deflection:

Stress intensity ahead of the crack tip can be reduced up to 50% by deflecting the crack away from the maximum tensile stress direction [2]. A crack may be diverted at the interface, if the adhesion energy of the interface is sufficiently lower than the cohesive energy of the material [42]. The indentation-induced fracture studies of ZrN/ZrAlN multilayer reveal that the incoherent interfaces between the layers offer the pathway for the crack deflection causing additional energy dissipation as shown in Fig. 2.6.

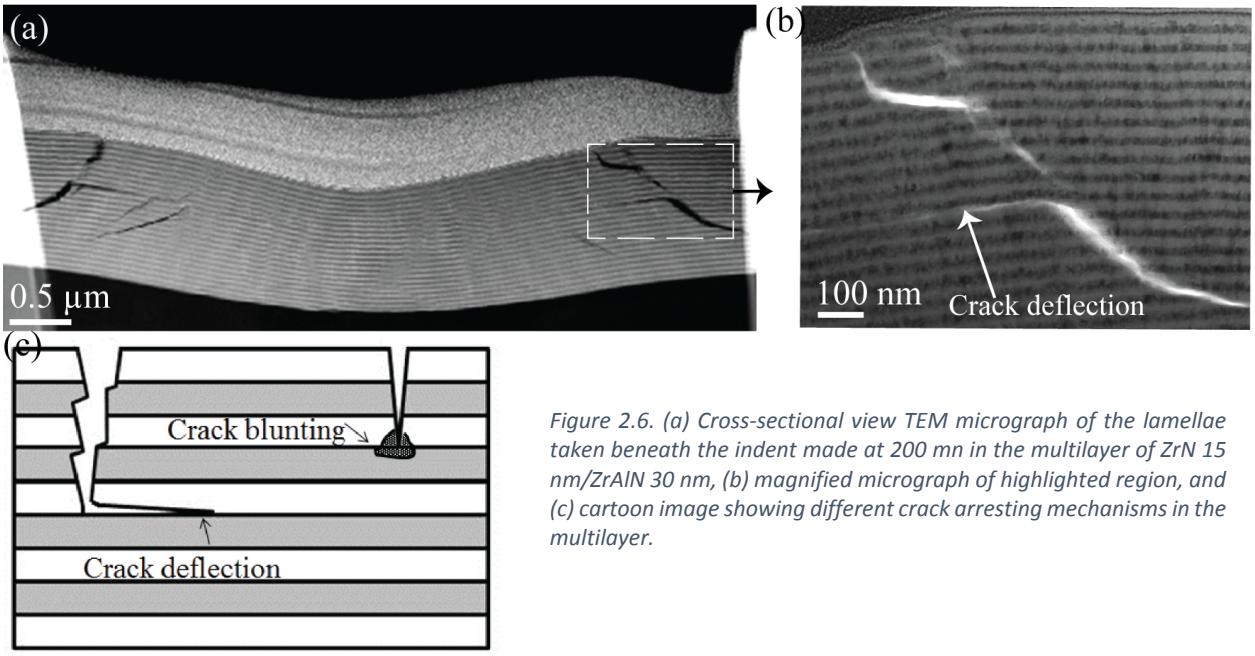

Figure 2.6. (a) Cross-sectional view TEM micrograph of the lamellae taken beneath the indent made at 200 mn in the multilayer of ZrN 15 nm/ZrAlN 30 nm, (b) magnified micrograph of highlighted region, and (c) cartoon image showing different crack arresting mechanisms in the multilayer.

In case of monolithic coatings, grain boundaries being the regions with lower shear strength, they are likely to offer the pathway for the crack deflection. As a result, fracture resistance of the bulk form ceramic materials is shown to be improved by reducing the grain size up to a critical limit of 100 µm similar to the Hall-Petch

relation for hardness [43]. This phenomenon of modifying the fracture resistance by inducing the microstructural variation is explored in Zr-Si-N coating (paper I). The microstructure is varied between columnar and nanocomposite structure, and their fracture resistance is investigated by indentation technique, as presented in Fig. 2.7.

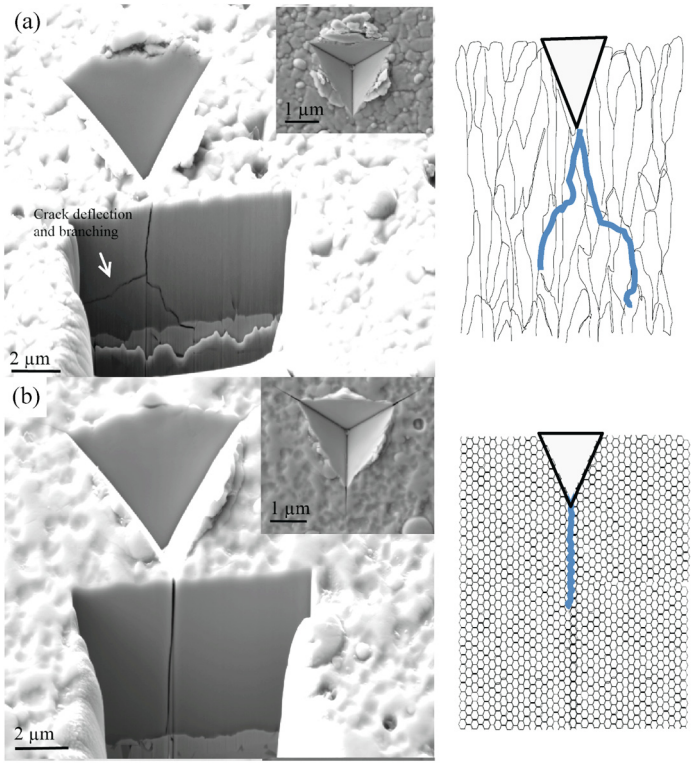

Figure 2.7. SEM micrograph of FIB cut cross-section after indentation of Zr-Si-N coating at a penetration depth of 3000 nm, inset image shows plan view before FIB cut. (a) 0.2 at.% Si, columnar structure, and (b) 6.3 at.% Si nanocomposite structure. Right side cartoon image shows crack propagation path.

SEM micrographs combined with the cartoon image in Fig. 2.7 indicate that the columnar structure offers a pathway for crack deflection presumably along the columnar boundaries, and causes additional energy dissipation. This results in high fracture resistance for the columnar structured coating (inset image in Fig. 2.7 a). In contrast, the nanocomposite structure did not show any visible crack deflection (Fig. 2.7b) that leads to a lower fracture resistance of the coating (in set image in Fig. 2.7 b), and the reasons are discussed in paper I.

2.2c. Stress- induced transformation toughening:

Stress concentration at the crack tip can be reduced by the volume dilatation around the crack by stress induced phase transformation of metastable phases. A well-known example is partially stabilized ZrO_2 [44,45]. When a crack propagate through the matrix of partially stabilized ZrO_2, stress field surrounding the crack tip transforms ZrO_2 from the metastable tetragonal to monoclinic phase. This phase transformation

is associated with a volume expansion of 4%, creating local compressive stresses that hinder crack propagation and results in K_{IC} value higher than 8 MPa $\sqrt{m}$ [46].

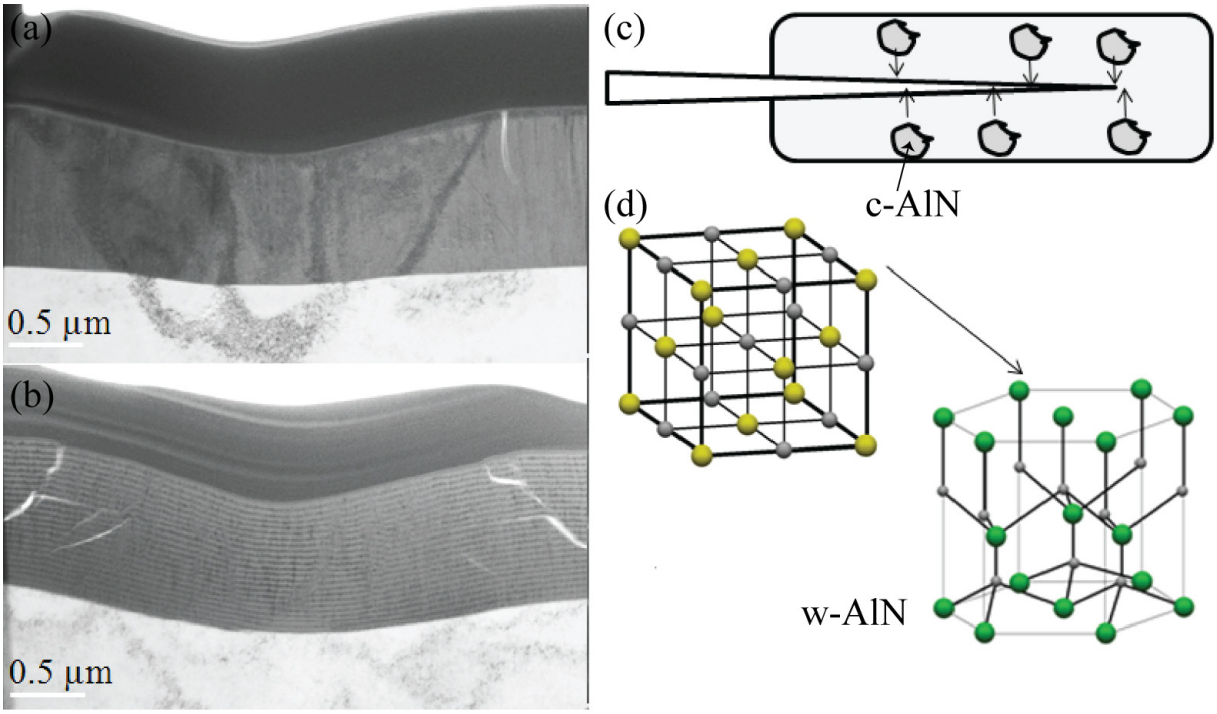

Figure 2.8. Cross-sectional view TEM micrograph of thin lamellae taken beneath the indent made at a force of 200mN in ZrN/ZrAlN multilayers with ZrAlN layer thickness of (a) 2 nm and (b) 30 nm. (c) Schematic illustration of arresting crack propagation by volume dilation around the crack due to, (d) stress induced transformation of c- AlN

However, it is not known, if such toughening mechanisms can be activated in hard coatings. Paper III explores this phenomenon and provides the first experimental evidence for the stress induced transformation toughening in TMN coatings, briefly presented in Fig. 2.8.

Multilayers of ZrN/ZrAlN are deposited, growth conditions and layer thickness are modified such that ZrAlN forms nanoscale domains of c- ZrN and AlN. AlN is formed in a metastable cubic structure for thin layers (Fig. 2.8a) and stable wurtzite structure for thick layers (Fig. 2.8b). The indentation induced fracture studies of the multilayer reveal a higher fracture resistance for the multilayer comprising c-AlN. The higher fracture resistance is discovered to be a consequence of stress induced transformation of c-AlN to w-AlN (Fig. 2.8d) associated with a molar volume expansion about 20% [47]. This causes local compressive stress zones that postpone both crack initiation and propagation, schematically shown in Fig. 2.8 c.

2.2d. Contact shielding:

Fiber reinforced bulk form ceramic materials have been shown to invoke energy dissipative mechanisms such as crack deflection, crack bridging and fiber pull out [48]. This causes significant toughness enhancement, and K_{IC} values even up to 30 MPa √m have been reported [48]. Xia et al., have explored this idea by reinforcing carbon nanotubes in Al_2O_3 coatings and reported an enhanced fracture resistance [49]. Similar effects might be possible for the TMN coatings which motivates further work in this direction.

2.3 Wear resistance

A high hardness and high fracture resistance are necessary conditions, but not sufficient conditions to achieve a high wear resistance. Several empirical parameters such as H/E, known as elastic strain to failure [50], H^3/E^2 known as resistance to plastic deformation [51] were proposed to be more valid criterion to predict the wear resistance of the coating. However, when two surfaces slide against each other several phenomena occurs simultaneously as shown in Fig. 2.9, which can be broadly classified into two categories (a) contact stress induced deformation and fracture related events, and (b) tribo-induced chemical reactions.

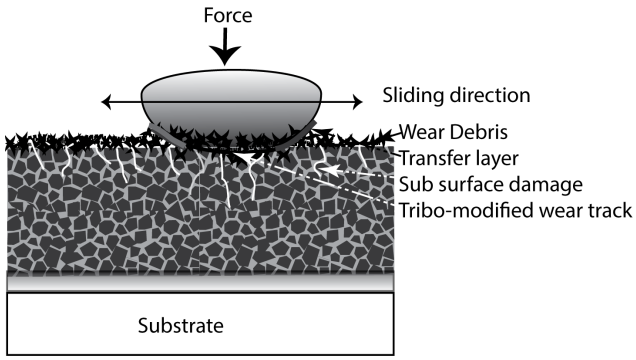

Figure 2.9. Schematic representation of several macro and micro damage mechanisms of coating under a sliding contact

The combination of thermal and mechanical energy in a tribosystem has been shown to significantly reduce the activation energy for a tribochemical reaction [52]. For example, the tribooxidation of ZrN, and TiN was observed at room temperature [53, 54], even though the thermally induced oxidation temperature has been observed only at a temperature above 500 °C. When the tribochemical reaction is initiated, the structure and the chemistry of the sliding surface undergo considerable

modification very locally. Subsequently, these structural and chemical changes influence the friction and wear properties. As a result of such a complex interplay of several factors, the tribological response of a coating is unique to every specific contact situation and the dependence of structural and chemical modifications of the coating on the wear properties may not be generalized. These aspects are investigated in paper II for Zr-Si-N coating as a function of microstructure and mechanical property variation under varied contact sliding conditions.

References:

[1] M. Odén, H. Ljungcrantz, L. Hultman, Characterization of the Induced Plastic Zone in a Single Crystal TiN(001) Film by Nanoindentation and Transmission Electron Microscopy, J. Mater. Res. 12 (2011) 2134–2142.

[2] R.W. Hertzberg, R.P. Vinci, J.L. Hertzberg, Deformation and Fracture Mechanics of Engineering Materials, 5th Edition, J. Wiley & Sons (2014).

[3] S. Ortmann, A. Savan, Y. Gerbig, H. Haefke, In-process structuring of CrN coatings, and its influenceon friction in dry and lubricated sliding, Wear. 254 (2003) 1099–1105.

[4] E.O. Hall, The Deformation and Ageing of Mild Steel: III, Proc. Phys. Soc. Sect. B. 64 (2002) 747–753.

[5] N.J. Petch, The cleavage strength of polycrystals, J. Iron Steel Inst. 174 (1953) 25 – 28.

[6] C.E. Carlton, P.J. Ferreira, What is behind the inverse Hall–Petch effect in nanocrystalline materials?, Acta Mater. 55 (2007) 3749–3756.

[7] H. Conrad, J. Narayan, K. Jung, Grain size softening in nanocrystalline TiN, Int. J. Refract. Met. Hard Mater. 23 (2005) 301–305.

[8] Z.B. Qi, P. Sun, F.P. Zhu, Z.C. Wang, D.L. Peng, C.H. Wu, The inverse Hall-Petch effect in nanocrystalline ZrN coatings, Surf. Coatings Technol. 205 (2011) 3692–3697.

[9] S. Vepřek, S. Reiprich, L. Shizhi, Superhard nanocrystalline composite materials: The TiN/Si3N4 system, Appl. Phys. Lett. 66 (1995) 2640.

[10] M. Stueber, H. Holleck, H. Leiste, K. Seemann, S. Ulrich, C. Ziebert, Concepts for the design of advanced nanoscale PVD multilayer protective thin films, J. Alloys Compd. 483 (2009) 321–333.

[11] B.M. Clemens, H. Kung, S.A. Barnett, Structure and strength of multilayers, MRS Bull. (1999) 20–26.

[12] Y. Long, F. Giuliani, S.J. Lloyd, J. Molina-Aldareguia, Z.H. Barber, W.J. Clegg, Deformation processes and the effects of microstructure in multilayered ceramics, Compos. Part B Eng. 37 (2006) 542–549.

[13] J.S. Koehler, Attempt to design a strong solid, Phy. Rev. B 2 (1970) 547.

[14] U. Helmersson, S. Todorova, S.A. Barnett, J.E. Sundgren, L.C. Markert, J.E. Greene, Growth of single-crystal TiN/VN strained-layer superlattices with extremely high

mechanical hardness, J. Appl. Phys. 62 (1987) 481–484.

[15] M. Shinn, L. Hultman, S.A. Barnett, Growth , structure , and microhardness of epitaxial TiN / NbN superlattices, J. Mater. Res. 7 (1992) 901-911.

[16] M. Setoyama, A. Nakayama, M. Tanaka, N. Kitagawa, T. Nomura, Formation of cubic-AIN in TiN/AIN superlattice, Surf. Coatings Technol.87 (1996) 225–230.

[17] X. Chu, M.S. Wong, W.D. Sproul, S.A. Barnett, Deposition, structure, and hardness of polycrystalline transition-metal nitride superlattice films, J. Materials research, (1999) 2500-2507.

[18] A. Misra, J.P. Hirth, R.G. Hoagland, Length-scale-dependent deformation mechanisms in incoherent metallic multilayered composites, Acta Mater. 53 (2005) 4817–4824.

[19] P.F. McMillan, New materials from high-pressure experiments, Nat. Mater. 1 (2002) 19-25.

[20] H. Holleck, Metastable coatings - Prediction of composition and structure, Surf. Coatings Technol. 36 (1988) 151–159.

[21] J. An, Q.Y. Zhang, Structure, morphology and nanoindentation behavior of multilayered TiN/TaN coatings, Surf. Coatings Technol. 200 (2005) 2451–2458.

[22] D.G. Kim, T.Y. Seong, Y.J. Baik, Effects of annealing on the microstructures and mechanical properties of TiN/AlN nano-multilayer films prepared by ion-beam assisted deposition, Surf. Coatings Technol. 153 (2002) 79–83.

[23] R.F. Zhang, S.H. Sheng, S. Veprek, First principles studies of ideal strength and bonding nature of AlN polymorphs in comparison to TiN, Appl. Phys. Lett. 91 (2007).

[24] M.A. Meyers, A. Mishra, D.J. Benson, Mechanical properties of nanocrystalline materials, Prog. Mater. Sci. 51 (2006) 427–556.

[25] K. Lu, L. Lu, S. Suresh, Strengthening materials by engineering coherent internal boundaries at the nanoscale., Science. 324 (2009) 349–352.

[26] J.W. Cahn, Hardening by spinodal decomposition, Acta Metall. 11 (1963) 1275–1282.

[27] S.-H. Jhi, J. Ihm, S.G. Louie, M.L. Cohen, Electronic mechanism of hardness enhancement in transition-metal carbonitrides, Nature. 399 (1999) 132–134.

[28] Thomas H. Courtney, Mechanical Behavior of Materials, Waveland Press Inc, Long Grove. Second edition (2005).

[29] Z.J. Liu, P.W. Shum, Y.G. Shen, Hardening mechanisms of nanocrystalline Ti-Al-N solid solution films, Thin Solid Films. 468 (2004) 161–166.

[30] M. Nose, W.A. Chiou, M. Zhou, T. Mae, M. Meshii, Microstructure and mechanical properties of Zr–Si–N films prepared by rf-reactive sputtering, J. Vac. Sci. Technol. A Vacuum, Surfaces, Film. 20 (2002) 823.

[31] B.J. Yeh, S. Chen, S. Lin, J. Gan, T. Chin, T. Shun, C.H. Tsau, S.Y. Change, Nanostructured High-Entropy Alloys with Multiple Principal Elements : Novel Alloy Design Concepts and Outcomes, (2004) 299–303.

[32] A. Wang, G. Yu, J. Huang, Surface & Coatings Technology Fracture toughness measurement on TiN hard coatings using internal energy induced cracking, 239 (2014) 20–27.

[33] S. Liu, J.M. Wheeler, P.R. Howie, X.T. Zeng, J. Michler, W.J. Clegg, Measuring the fracture resistance of hard coatings, Appl. Phys. Lett. 102 (2013) 1–5.

[34] S. Zhang, D. Sun, Y. Fu, H. Du, Toughness measurement of thin films: A critical review, Surf. Coatings Technol. 198 (2005) 74–84.

[35] M. Sebastiani, K.E. Johanns, E.G. Herbert, F. Carassiti, G.M. Pharr, A novel pillar indentation splitting test for measuring fracture toughness of thin ceramic coatings, Philos. Mag. 0 (2014) 1–17.

[36] B.N. Jaya, C. Kirchlechner, G. Dehm, Can microscale fracture tests provide reliable fracture toughness values? A case study in silicon, J. Mater. Res. 30 (2015) 686–698.

[37] K. Chen, L.R. Zhao, J. Rodgers, J.S. Tse, Alloying effects on elastic properties of TiN-based nitrides, J. Phys. D. Appl. Phys. 36 (2003) 2725–2729.

[38] D.G. Sangiovanni, L. Hultman, V. Chirita, Supertoughening in B1 transition metal nitride alloys by increased valence electron concentration, Acta Mater. 59 (2011) 2121–2134.

[39] H. Kindlund, D.G. Sangiovanni, L. Martínez-de-Olcoz, J. Lu, J. Jensen, J. Birch, I. Petrov, J. E. Greene, V. Chirita, L. Hultman, Toughness enhancement in hard ceramic thin films by alloy design, APL Mater. 1 (2013) 042104.

[40] L. Zhou, D. Holec, P.H. Mayrhofer, Ab initio study of the alloying effect of transition metals on structure, stability and ductility of CrN, J. Phys. D. Appl. Phys. 46 (2013) 365301.

[41] S. Zhang, D. Sun, Y. Fu, Y.T. Pei, J.T.M. De Hosson, Ni-toughened nc-TiN/a-SiNx nanocomposite thin films, Surf. Coatings Technol. 200 (2005) 1530–1534.

[42] K. Kendall, Transition between Cohesive and Interfacial Failure in a Laminate, Proc. R. Soc. A Math. Phys. Eng. Sci. 344 (1975) 287–302. doi:10.1098/rspa.1975.0102.

[43] A.F. Bower, The influence of grain size on the Toughness of monolithic ceramics.pdf, J. Eng. Mater. Technol. 115 (1993) 228–236.

[44] R.C. Garvie, R.H. Hannink, R.T. Pascoe, Ceramic steel?, Nature. 258 (1975) 703–704.

[45] R.H.J. Hannink, P.M. Kelly, B.C. Muddle, Transformation Toughening in Zirconia-Containing Ceramics, J Am Ceram Soc. 83 (2000) 461–87.

[46] D.L. Porter, A.G. Evans, A.H. Heuer, Transformation-toughening in partially-stabilized zirconia (PSZ), Acta Metall. 27 (1979) 1649–1654.

[47] Q. Xia, H. Xia, A.L. Ruoff, Pressure-induced rocksalt phase of aluminum nitride: A metastable structure at ambient condition, J. Appl. Phys. 73 (1993) 8198.

[48] A.G. Evans, Perspective on the Development of high-toughness ceramics, J. Am. Ceram. Soc. 73 (1990) 187–206.

[49] Z. Xia, L. Riester, W.A. Curtin, H. Li, B.W. Sheldon, J. Liang, et al., Direct observation of toughening mechanisms in carbon nanotube ceramic matrix composites, Acta Mater. 52

(2004) 931–944.

[50] A. Leyland, A. Matthews, On the significance of the H/E ratio in wear control: A nanocomposite coating approach to optimised tribological behaviour, Wear. 246 (2000) 1–11.

[51] J. Musil, Hard and superhard nanocomposite coatings, Surf. Coatings Technol. 125 (2000) 322–330.

[52] G. Kaupp, Mechanochemistry: the varied applications of mechanical bond-breaking, Cryst Eng Comm. 11 (2009) 388.

[53] E. Vancoille, B. Blanpain, Y. Xingpu, J.-P. Celis, J.R. Roos, Tribo-oxidation of a TiN coating sliding against corundum, J. Mater. Res. 9 (1994) 992–998.

[54] S. Wilson, A.T. Alpas, Tribo-layer formation during sliding wear of TiN coatings, Wear. 245 (2000) 223–229.

3. Physical vapor deposition and coating growth

Two different plasma based physical vapor deposition (PVD) techniques, known as reactive DC magnetron sputtering and reactive arc deposition are used in the current work. In both the techniques, coatings are grown by vaporizing a target material and subsequently condensing the vapor on the substrate with very high cooling rate of 10^{10} K/s [1]. The following chapter provides a brief description of both these processes.

3.1 Sputter deposition

Sputtering is an atomistic scale sandblasting process, where the target surface atom is ejected out by an energetic incident particle.

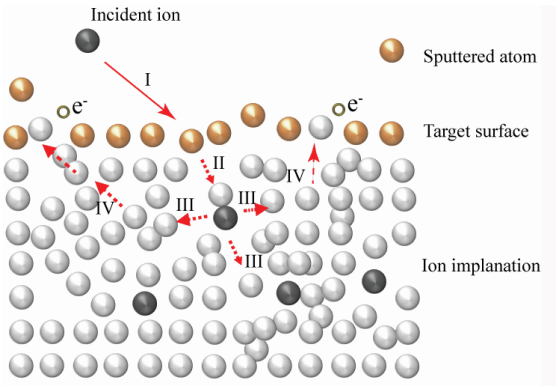

Figure 3.1. Schematic representation of sputtering mechanism. Roman numerals indicate series of collision events.

The process is schematically shown in Fig. 3.1, an incident particle initiates a collision cascade in the target, when the cascade recoil and reaches the target surface with an energy higher than the surface binding energy (SBE), the surface atom is ejected as a sputtered particle [2]. Most of the sputtered particles are neutrals, with a high probable ejected energy of 5 – 10 eV which is independent of the incident ion energy [3]. Besides sputtering, several other effects take place on the target surface, such as adsorption, reflection, chemical reaction, backscattering and implantation etc.

Sputter deposition is typically performed in a high voltage and low current glow discharge process, schematically shown in Fig. 3.2. When a high potential difference is applied between the electrodes in a low pressure inert gas atmosphere, the electric field accelerates the free electrons (generated by background radiation in the sputtering gas) towards the anode. The accelerated electrons will gain energy and collide with neutral gas atoms, causing ionization of the process gas. The ionized species are accelerated towards the negatively charged target and create a collision cascade which leads to ejection of the target surface atom.

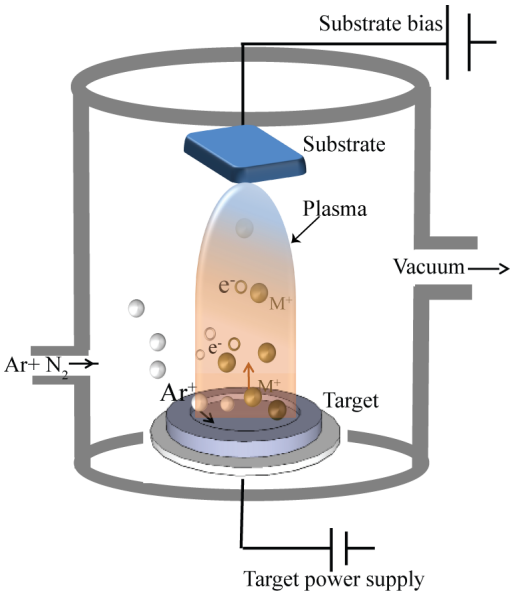

Figure 3.2. Schematic illustration of sputtering process.

Furthermore, the ion-surface interactions also causes ejection of secondary electrons from the target surface [4]. The secondary electrons further give rise to new ionization collisions in the processing gas, creating new ions and electrons, which eventually leads to self-sustaining plasma.

The efficiency of sputtering process is quantified as sputtering yield, defined as the number of target atoms ejected per incident particle which is typically between 0.5 to 5 for the regular DC sputtering conditions [5]. The sputter yield can be enhanced by (a) increasing the incident ion energy, (b) lowering the SBE of target material, (c) best mass match between the incident ions and the target atom, and (d) an optimal incidence angle of ~ 55 - 70° [6,7].

3.2 Magnetron sputtering

The sputtering process efficiency can be significantly enhanced by applying a magnetic field close to the target surface [8], known as magnetron sputtering.

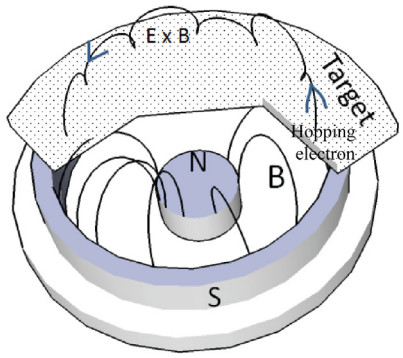

Figure 3.3. Cutaway view of magnetron

A magnetron consists of an external magnet that is located parallel to the target surface, and generates a static magnetic field. The crossed electric and magnetic field (E × B) confines the secondary electrons close to the target surface with long trajectories as shown in Fig. 3.3. Such electron confinement increases the electron-atom collision, yielding a high ionization probability of the processing gas. This causes increased ion bombardment of the target surface that leads to higher sputter rate. Magnetic field strength is the key operational parameter, higher the strength better the ionization efficiency. However, previous studies reveals that the efficiency saturate at higher field strength of 500 - 700 G (tangential component measured on the cathode surface) [9]. Higher magnetic field strength also causes deeper wear track, which leads to less utilization of the target.

Based on the magnetic field configuration, magnetrons are classified as balanced and unbalanced magnetrons (Type I and II) as shown in Fig. 3.4.

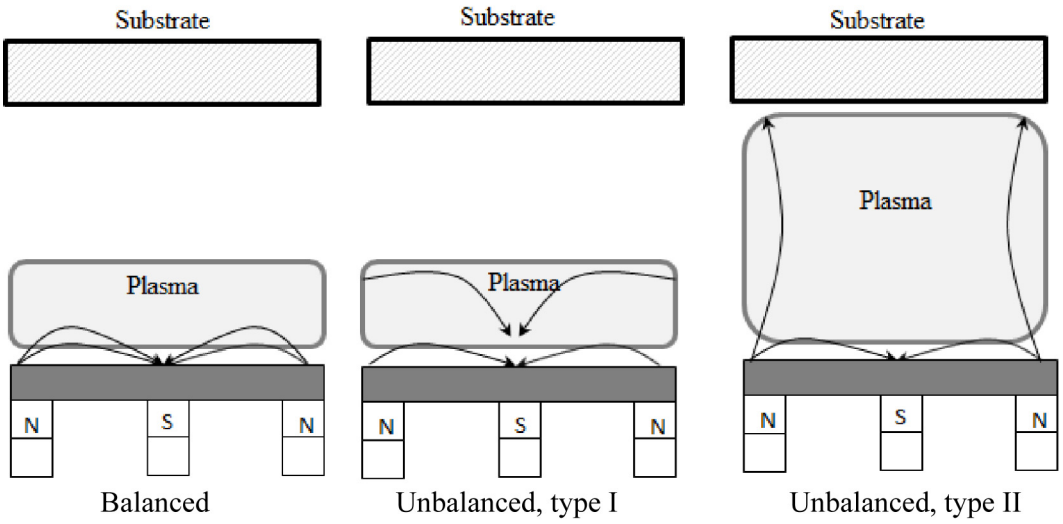

Figure 3.4. Plasma confinement of balanced and unbalanced magnetron sputtering after Kelly and Arnell (Kelly & Arnell, 2000)

In case of balanced magnetron, the strength of the inner and outer poles are balanced. Unbalanced type I configuration consists stronger inner pole relative to the outer pole causing a reduced ion fraction near the substrate, forming porous and chemically reactive coatings [10]. In type II unbalanced magnetron sputtering, the outer pole is relatively strengthened to the center pole. In this configuration, all the field lines are not closed at the center pole, some of the outer field lines are directed towards the substrate and secondary electrons are able to follow these lines. The secondary electrons near the substrate cause ionization of the processing gas and increase the ion to metal atom arrival ratio (J_{ion}/J_{met}) at the substrate.

In this work, the glow discharge is obtained at a voltage of 400 V, and current of 0.5 A in a N_2 and Ar partial pressures of 0.06 and 0.5 Pa in a chamber with 500 mm diameter and 350 mm height, and a target-to-substrate distance of 120 mm.

The deposition system is equipped with an additional tunable solenoid surrounding the substrate that is synchronized with the individual unbalanced type II magnetrons. This set up has a resulted a significant increase in the plasma density near the substrate as shown in Fig. 3.5.

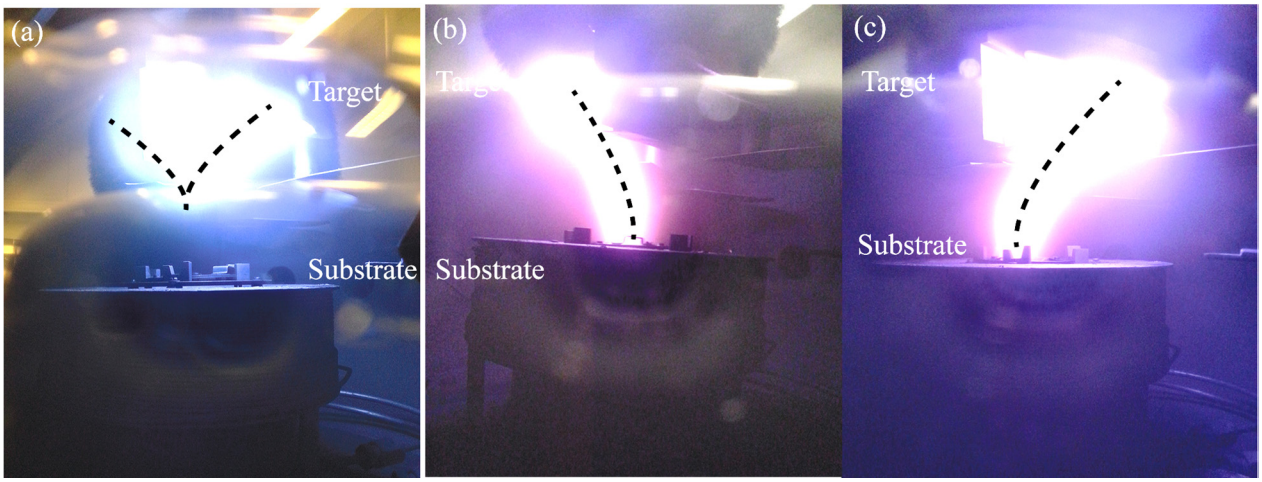

Figure 3.5. Plasma confinement under different configurations of solenoid coil. (a) without solenoid, (b) solenoid coupled with left magnetron, and (c) solenoid coupled with right magnetron.

When the solenoid is activated, the secondary electrons there by the plasma is guided to the substrate (Fig. 3.5 b and c), otherwise the plasma is essentially confined near the target region. This arrangement has been shown to boost the ion to metal ratio (J_{ion}/J_{met}) near the substrate by a factor of 100 (from 0.5 to more than 50) [11,12]. A high ionization fraction in the plasma with a moderate energy (20-30 eV) promote increased adatom mobility at the growth front which leads to a dense and uniform coating [1].

3.3 Cathodic arc deposition

The cathodic arc process is the current workhorse of the hard coating industry. The unique feature of this process is to vaporize the target material with a high degree of ionization (> 90%) [13] that facilitates greater surface mobility of adatoms. Higher adatom mobility leads to better adhesion, and uniform coating with higher density. In this work, an industrial scale Oerlikon/Metaplas MZR-323 arc evaporation chamber is used in a continuous (DC) arc mode (Fig. 3.6 a). An electric arc is a low-voltage, high-current discharge process, schematically illustrated in Fig. 3.6 b.

The process begins by striking an arc on the cathode surface that gives rise to a few micrometers (1-10 μm) energetic emitting area known as cathode spot (Fig. 3.6 c). The power density at the spot is extremely high and reaches up to 10^9 Wm^{-2} [14]. Such high power densities can transform the cathode materials from a solid phase to plasma phase in extremely short time period of 10-100 ns, known as explosive phase transformation [15]. The localized temperature of the cathode spot is extremely high (~ 5000-10000 °C) [16], which results in a high velocity jet of vaporized cathode material, leaving a crater on the cathode surface. The cathode spot emits electrons by

a combination of thermionic emission and field emission associated with the high temperature and high electric field at the cathode spot [13].

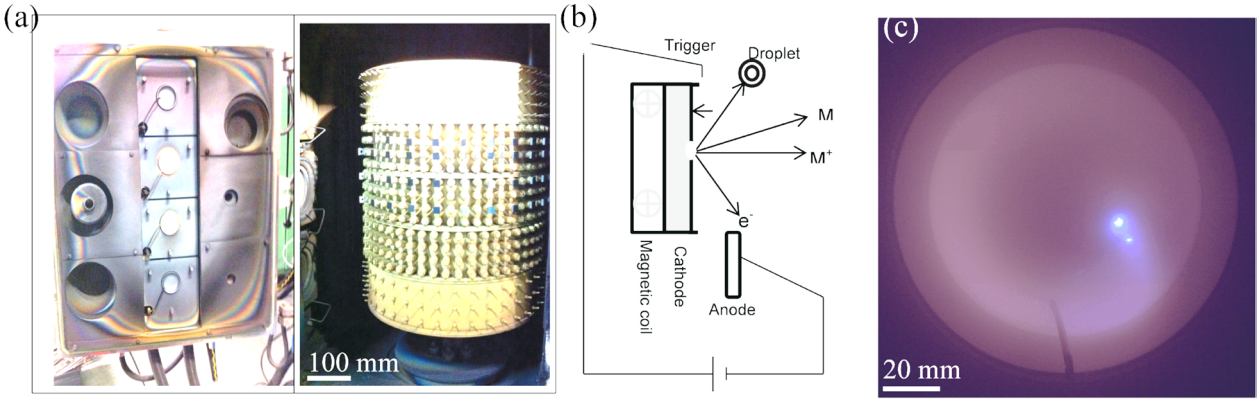

Figure 3.6. (a) Industrial scale arc deposition chamber used in this work, (b) arc evaporation process at the cathode, and (c) cathode spot on Ti target captured with a high speed camera. Figure c courtesy of B. Syed.

As the cathode spot expands, its power density, and consequently the peak temperature is reduced. This lowers the electron emission which results in a transition of the cathode spot from explosive phase to evaporative phase and finally the discharge ceases. The whole cycle takes place between 10 ns to 1 μs [13], then it self-extinguishes and reignites in a new area close to the previous crater and it moves either randomly or steered in the presence of external magnetic field [17]. This behavior is responsible for the apparent motion of the arc. The plasma pressure within a cathode spot is high, and the strong pressure gradient causes the plasma generated there to accelerate away from the surface. The plasma also supports the current flow between the electrodes and make the arc process self-sustaining. There is a lower limit to arc current, called the chopping current below which the cathode spot will not persist [18], an upper limit is determined by the source cooling requirements. Deposition parameters used in this work are, an arc current of 100 A and a burning voltage of 30 V, using a substrate temperature of 400 °C in the pure N_2 atmosphere at an operating pressure of 4 Pa.

3.3a Macroparticles:

The most important challenge of the cathodic arc deposition process is to control macroparticle incorporation in the coating. They are formed by the ejected molten droplets, surrounding the hot cathode spot, by a high local plasma pressure. These particles cause shadowing effect of the incident ion flux that results in undesirable voids surrounding them as shown in Fig. 3.7. The composition of these particles being completely different [19] from the rest of the coatings, they are a local source

of variation in physical and mechanical properties. Later, during the application, these voids will act as stress concentrators that facilitate crack initiation. Previous studies [20] have shown that both flank wear and rake wear of the cutting tool gets accelerated in the presence of macroparticles.

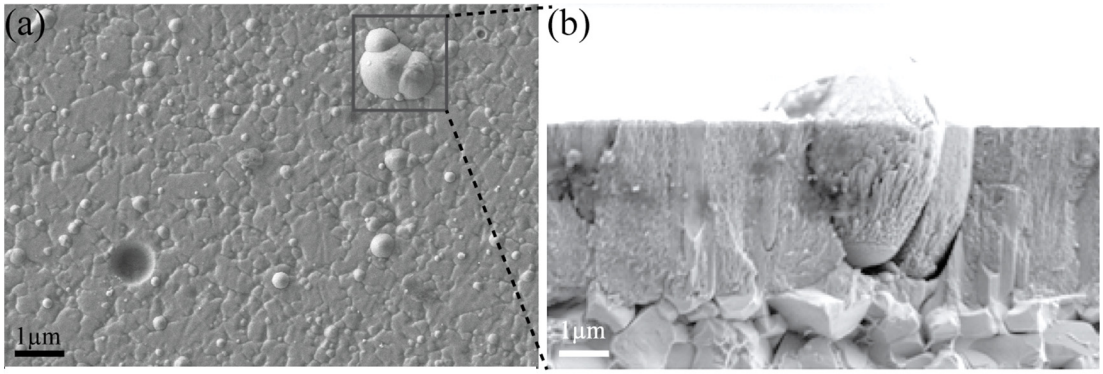

Figure 3.7. (a) SEM image of arc deposited ZrN film showing macro particle in plan view, and (b) cross-sectional view.

A technical solution to eliminate the macroparticles is to filter them using a curved magnetic filter [21]. However, the plasma filtering causes a significant drop in the deposition rate [13], and did not find great commercial success in the hard coating market. A routine practice in the industry is to steer the arc by an external magnetic field that reduces the mean lifetime of cathode spot. This in turn reduces the volume of the molten pool surrounding the cathode spot that may be ejected as droplets [17,22]. Other ideas to reduce macroparticle density includes higher partial pressure of reactive gas [23], pulsed-arc process [24], and refined grain size of a composite cathode [25].

3.4 Reactive vapor deposition

A direct way to grow a nitride coating is probably to use a compound target with the required stoichiometry. However, most of the compound material is electrically insulating which causes process instabilities. Even though some nitrides have satisfactory electrical conductivity to form a self-sustaining arc discharge, their high cohesive energy causes lower deposition rates [26]. Hence, a convenient way to grow the compound coating is by obtaining the metallic target discharge in a reactive gas atmosphere, known as reactive vapor deposition.

Nitride coatings in this thesis are grown by condensing the metallic vapor flux in a plasma activated nitrogen atmosphere. The molecular nitrogen (N_2) interacts with plasma and gets ionized either by electron impact ionization ($e + N_2 \rightarrow N^+ + 2e^-$)[27], or by charge exchange ionization ($Ar^+ + N \rightarrow N^+ + Ar$) [28], and accelerate towards

the negatively charged substrate. The chemical bonding between metallic and non-metallic species are established on the growth front of the coating, where the substrate offers the conservation of momentum and energy resulting from the compound formation. The stoichiometry of the compound coatings can be varied by changing the partial pressure of the reactive gas [29].

During the process, the reactive gas ions also form a compound layer on the target surface, which leads to so called poisoning effect. In case of sputtering, the target poisoning is generally not desirable as the formation of an electrically resistive compound layer interrupts the charge transport between the electrodes and results in arcing [5]. In contrast, the poisoning effect is less pronounced in the arc evaporation process as the arc spot depth is relatively higher than the thickness of compound layer. Furthermore, the compound layer formation on the cathode surface may reduce macro particle density, as observed for Ti in N_2 atmosphere [30].

3.5 Growth of PVD coatings

When the plasma species arrive at the substrate, the hyperthermal particles make a random walk, and join together to make a cluster. If the cluster acquire the critical radius they becomes stable nuclei [31], subsequently the incident atoms are drawn to these clusters, these clusters grow in size and gets coalesced to form a dense and continues coating.

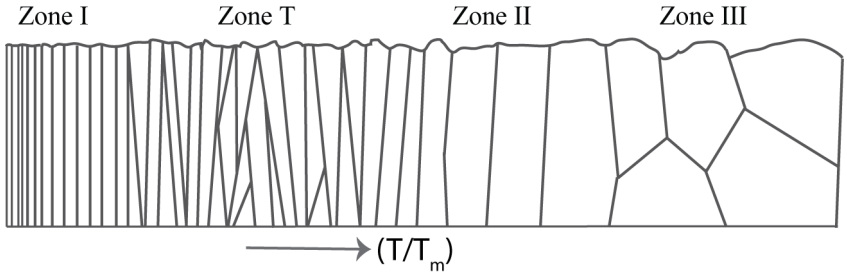

Figure 3.8. Microstructure evolution as a function of normalized temperature (T/T_m) after Barna et al. [32]

The microstructure evolution of a polycrystalline coating as a function of several growth parameters are typically represented by so called structure zone model (SZM) [33,34]. Two important parameters that influence the microstructure of the coatings are, kinetic energy of the incident species and growth temperature. The kinetic energy of the incident species can be tuned by varying the substrate bias voltage coupled with the charge state of the incident ions, and working pressure. Whereas the growth temperature can be tuned by varying the substrate temperature, and local atomic scale

heating caused by high potential energy of the incident ions, which is in the range of 5 to 15 eV per ion [35]. Figure 3.8 shows variation in the microstructure as a function of normalized growth temperature (T/T_M), where T and T_M are the growth and melting temperature of the coating material.

Zone 1 corresponds to lower temperature region that corresponds to limited adatom diffusivities resulting a fine porous columnar structure. Zone T represents the transition region, where surface diffusion is active but not grain boundary diffusion. As a result, the low surface diffusivity grains over grow the high surface diffusivity grains. This results in V- shaped grains with a microstructure variation across the coating thickness. Zone II represents coating growth, where both surface diffusion and grain boundary diffusion are active, resulting a homogenous columnar microstructure. Zone III corresponds to equiaxed structure that is formed under the combined effect of recrystallization and breakdown of the columnar structure by surface segregated residual elements out gassed from the chamber at high growth temperature [32].

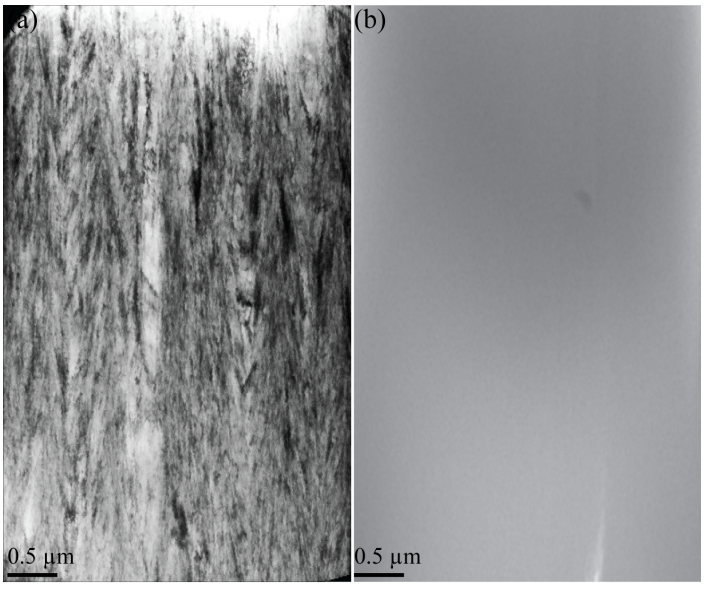

Figure 3.9. Cross-sectional BF- TEM micrograph, (a) ZrN, and (b) Zr-Si-N.

In addition to above mentioned growth factors, the coating microstructure can be tuned by varying the composition. Figure 3.9 shows BF-TEM micrograph revealing a fine columnar structure for the arc deposited ZrN coating (Fig. 3.9a). However, the Si addition, as low as 6.3 at. % causes breakdown of columnar structure and evolves a nanocomposite structure that gives a featureless contrast (Fig. 3.9 b). This effect is further extended in paper II and III to form a self-organized 2D and 3D nanocomposite structures with both chemical and structural modulations.

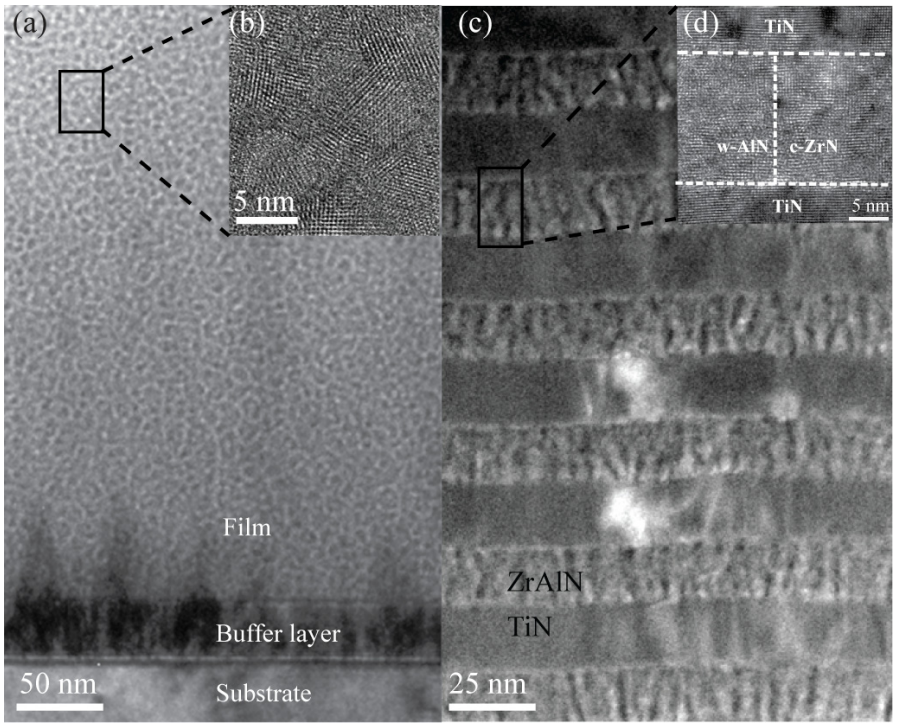

Figure 3.10. Overview BF-TEM and inset lattice resolved TEM image of (a) ZrAlN, and (b) TiN/ZrAlN multilayer.

Figure 3.10a shows BF-TEM and lattice resolved micrograph (inset image) of ZrAlN coating grown at a temperature of 700 °C. A high growth temperature causes the chemical segregation of the immiscible material during the growth that evolves a self-organized 3D nanocomposite consisting of nanoscale domains of c-ZrN and w-AlN. For such a nanocomposite material, the volume of the material located near the interfaces is significantly high. For a domain size of 6 nm and with an interface width of 1 nm, the estimated interface volume is up to 50 % (estimated as $3\Delta/d$, Δ is interface width, and d is the average grain diameter) [36]. A high interface volume naturally leads to a high interface energy. Subsequently, the interface energy minimization favors semi-coherent interfaces between cubic, and wurtzite domains provided the adatoms have high mobility, and cubic domains are grown in favorable crystallographic orientation (refer chapter 6). Figure 3.11 shows the BF-TEM and lattice resolved micrograph (inset image) of TiN/ZrAlN, where non-isostructural (semi-) coherent interfaces are formed between c-ZrN, c-TiN and w-AlN by tuning the growth conditions. The (semi-) coherency leads to self-aligned 2D chemical and structural modulation in the ZrAlN layer. Further details about the thermodynamic and kinetic conditions favoring this structure and the effect of the (semi-) coherency on the mechanical properties are discussed in paper IV.

3.6 References

[1] M. Ohring, Materials Science of Thin Films 2 nd edition, Academic Press (2001).

[2] S. Rossnagel, Sputtering and Sputter Deposition, in K. Sheshan (Eds.) Handbook of Thin film deposition process and techniques, Elsevier Science (2001) 319.

[3] R.V. Stuart, G.K. Wehner, G.S. Anderson, Energy distribution of atoms sputtered from polycrystalline metals, J. Appl. Phys. 40 (1969) 803–812.

[4] N. Bajales, S. Montoro, E.C. Goldberg, R.A. Baragiola, J. Ferrón, Identification of mechanisms of ion induced electron emission by factor analysis, Surf. Sci. 579 (2005) 97–102.

[5] D. Depla, S. Mahieu, J.E. Greene, Sputter Deposition Processes, in P.M. Martin (EDs.) Handbook of deposition technologies for films and coatings, Elsevier Science (2010) 253–296.

[6] P.Sigmund, Theory of sputtering, Part1: Sputtering yield of amorphous and polycrystalline targets, Phys. Rev. 184 (1969) 383-416.

[7] Q. Wei, K.-D. Li, J. Lian, L. Wang, Angular dependence of sputtering yield of amorphous and polycrystalline materials, J. Phys. D. Appl. Phys. 41 (2008) 172002.

[8] P. Kelly, R. Arnell, Magnetron sputtering: a review of recent developments and applications, Vacuum. 56 (2000) 159–172.

[9] J. Goree, T.E. Sheridan, Magnetic field dependence of sputtering magnetron efficiency, Appl. Phys. Lett. 59 (1991) 1052–1054.

[10] J.O Brien, R.D. Arnell, The production and characterisation of chemically reactive porous coatings of zirconium via unbalanced magnetron sputtering, Surf. Coatings Technol. 86-87 (1996) 200–206.

[11] I. Petrov, Use of an externally applied axial magnetic field to control ion/neutral flux ratios incident at the substrate during magnetron sputter deposition, J. Vac. Sci. Technol. A. 10 (1992) 3283.

[12] N. Ghafoor, Materials Science of Multilayer X-ray Mirrors, Dissertation No. 1169.

[13] A. Anders, Cathodic Arcs, Springer (2008).

[14] D.M. Sanders, A. Anders, Review of cathodic arc deposition technology at the start of the new millennium, Surf. Coatings Technol. 133-134 (2000) 78–90.

[15] B. Juttner, Cathode spots of electric arcs, J. Phys. D: Appl. Phys. 34 (2001) 103.

[16] T. Utsumi, Measurements of Cathode Spot Temperature in Vacuum Arcs, Appl. Phys. Lett. 18 (1971) 218.

[17] P. D. Swift, Macroparticles in films deposited by steered cathodic arc, J. Appl. Phys. 29 (2006) 2025–2031.

[18] R. Peter, P. Smeets, The Origin of Current Chopping in Vacuum Arcs, IEEE Trans. Plasma Sci. 17 (1989) 303–310.

[19] M.H. Shiao, Z.C. Chang, F.S. Shieu, Charecterization and formation mechanism of macroparticles in arc ion-plated CrN thin films, Journal of the Electro. Soc. 150 (2003) 320-324

[20] S. Boelens, H. Veltrop, Hard coatings of TIN, (TiHf)N and (TiNb)N eposited by random and steered arc evoperation, Surf. Coatings Technol. 33 (1987) 63–71.

[21] A. Anders, S. Anders, I.G. Brown, Transport of vacuum arc plasmas through magnetic macroparticle filters, Plasma Sources Sci. Technol. 4 (1995) 1-12.

[22] I.G. Brown, Cathodic arc deposition of films, Annu. Rev. Mater. Sci. 28 (1998) 243.

[23] S.G. Harris, E.D. Doyle, Y.C. Wong, P.R. Munroe, J.M. Cairney, J.M. Long, Reducing the macroparticle content of cathodic arc evaporated TiN coatings, Surf. Coatings Technol. 183 (2004) 283–294.

[24] M. Büschel, W. Grimm, Influence of the pulsing of the current of a vacuum arc on rate and droplets, Surf. Coatings Technol. 142-144 (2001) 665–668.

[25] J. Zhu, A. Eriksson, N. Ghafoor, M.P. Johansson, J. Sjolen, L. Hultman, J. Rosén, M.Odén, Characterization of worn Ti-Si cathodes used for reactive cathodic arc evaporation, J. Vac. Sci. Techno. A 28 (2010) 347–353

[26] P.H. Mayrhofer, D. Sonnleitner, M. Bartosik, D. Holec, Structural and mechanical evolution of reactively and non-reactively sputtered Zr-Al-N thin films during annealing, Surf. Coatings Technol. 244 (2014) 52–56.

[27] A.C.H. Smith, E. Caplinger, R.H. Neynaber, E.W. Rothe, S.M. Trujillo, Electron impact ionization of atomic nitrogen, Phy. Rev. 582 (1962) 1647-1649.

[28] Th. J. M. Sluyters, E. De Haas, J. Kistemaker, Charge exchange, Ionization and electron loss cross-sections in the energy range 5 to 24 keV, Physica 25 (1959) 1376-1388

[29] L. Li, G. Lv, S. Yang, Effects of nitrogen partial pressure in Ta–N films grown by the cathodic vacuum arc technique, J. Phys. D. Appl. Phys. 46 (2013) 285202.

[30] P. Hovsepian, D. Popov, Cathode poisoning during reactive arc evaporation of titanium in nitrogen atmosphere, Vacuum. 45 (1994) 603–607.

[31] I. Petrov, P.B. Barna, L. Hultman, J.E. Greene, Microstructural evolution during film growth, J. Vac. Sci. Technol. A. 21 (2003) S117-S128

[32] P. Barna, M. Adamik, Fundamental structure forming phenomena of polycrystalline films and the structure zone models, Thin Solid Films. 317 (1998) 27–33.

[33] B.A. Movchan, A.V Demchishin, Obtaining depositions during vacuum condensation of metals and alloys, Phys. of. metals and research. 28 (1969) 653.

[34] A. Anders, A structure zone diagram including plasma-based deposition and ion etching, Thin Solid Films. 518 (2010) 4087–4090.

[35] P.S. Matsumoto, Trends in Ionization Energy of Transition-Metal Elements, J. Chem. Educ. 82 (2005) 1660-1661.

[36] M.A. Meyers, A. Mishra, D.J. Benson, Mechanical properties of nanocrystalline materials, Prog. Mater. Sci. 51 (2006) 427–556.

4. Material systems

Today, TiN, and CrN based hard coatings are the backbone for several tooling applications[1]. Alloying these binary nitrides with AlN and SiN_x have resulted in several successful ternary and quaternary nitride alloys such as Ti-Al-N [2,3], Cr-Al-N, Ti-Cr-Al-N [4], Ti-Si-N, Ti-Al-Si-N, Ti-Zr-Al-N [5–7] with improved hardness, oxidation resistance and tribological properties.

Even though ZrN has the same crystal structure and comparable mechanical properties to TiN, and CrN, they are relatively less explored. Recent theoretical and experimental investigations have shown several interesting facts about ZrN based coatings. For example, Zr-Al-N has a larger miscibility gap compared to Ti-Al-N [8]. This means, a higher driving force for segregation of Zr-Al-N alloy which is an enabling criteria for the formation of self-organized nanostructure. Furthermore, recent studies report a comparable cutting performance between high Al containing Zr-Al-N coating and commercial grade Ti-Al-N coatings [9].

4.1 Zr-N

Cubic ZrN phase is stable for a wide range of nitrogen content, the lower limit is reported to be $ZrN_{0.56}$ [10] and the higher limit is not known precisely. ZrN has mixed metallic, ionic and covalent bonding characteristics [11]. Crystal structure of ZrN closely resembles TiN, but has a larger lattice parameter (ZrN, a = 4.58 Å [12] and TiN, a = 4.24 Å [13]). ZrN coatings have been reported with a hardness and elastic modulus in the range of 23-26 GPa and 400-450 GPa respectively [14–16]. ZrN has an aesthetic advantage over TiN with pleasing light gold color, which makes it as a strong candidate material for decorative coating applications. Figure 4.1 shows cubic B1 crystal structure[1] of ZrN, each Zr atom is coordinating six N atoms and vice versa.

At higher nitrogen content, orthorhombic Zr_3N_4 phase has been found [17]. Manish et al.,[18] have reported a structural transformation of Zr_3N_4 from orthorhombic to cubic structure by synthesizing the coatings in a high compressive stress state in the

[1] Schematic representation of crystal structures are courtesy of Hanna Fager

order of 9 GPa. The c-Zr_3N_4 coatings have displayed a high hardness of 36 GPa and a high wear resistance [18].

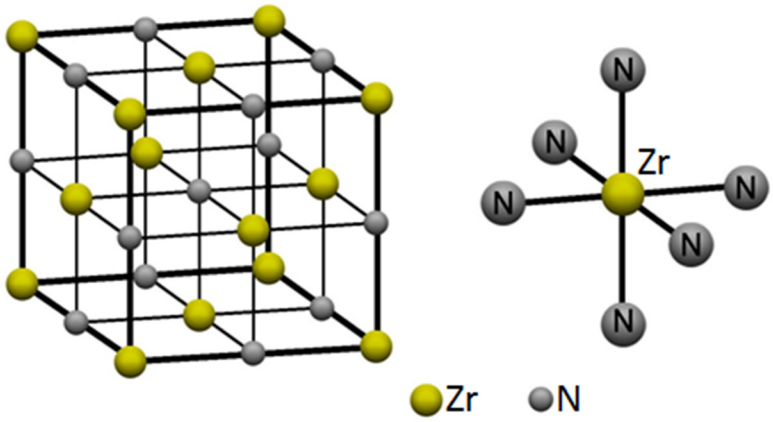

Figure 4.1. Cubic B1 crystal structure of ZrN.

4.2 Si-N

Silicon nitride (Si_3N_4) is the only line compound in the Si-N material system which has predominantly covalent bonding (70 %) [19]. Si_3N_4 has two polymorphic forms designated as α phase and β phase with trigonal and hexagonal symmetries respectively, and the transformation temperature from α to β phase has been reported to be around 1600 K [20]. A metastable γ phase with cubic structure can also be synthesized with a high hardness of 30 GPa [21] at high pressures and high temperatures (15 GPa and 2000 K). The bulk form Si_3N_4 display high strength and toughness over a wide range of temperatures, and is a candidate material for diverse applications such as metal cutting inserts, automotive, and gas turbine components [22].

Si_3N_4 coatings deposited by reactive sputter deposition have displayed an amorphous dominated structure, with a hardness of 23 GPa and elastic modulus of 220 GPa even at a growth temperature of 800 °C [23]. A crystalline Si_3N_4 coating could be grown only above 1300 °C [23] which indicates its sluggish diffusive nature. Figure 4.2 shows the trigonal structure of Si_3N_4, Si atoms are located at the center of SiN_4 tetrahedra, every Si atom coordinates four nitrogen atoms and every N atom coordinates three Si atoms.

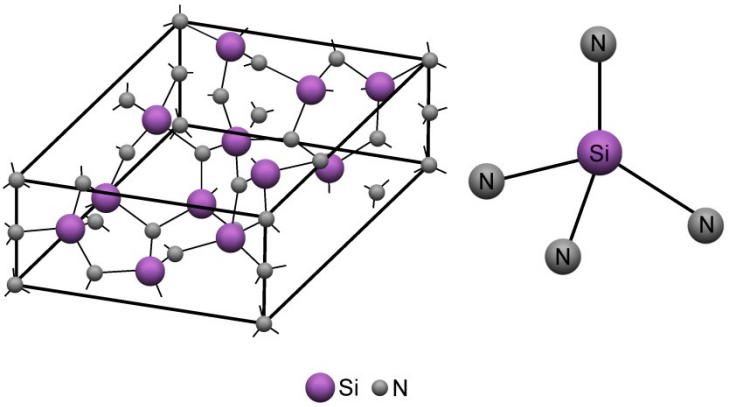

Figure 4.2 Crystal structure of α Si_3N_4.

4.3 Zr-Si-N

A high hardness (> 40 GPa) of the Ti-Si-N nanocomposite coating [24–26] has motivated Zr-Si-N material system [16,27,28]. At a Si content around 3-6 at. %, Zr-Si-N alloy forms a nanocomposite structure consisting ZrN nanocrystals and a monolayers of SiN_x presumably surrounding ZrN crystals [16,29–31]. However, the expected hardness enhancement is absent, i.e. the nanocomposite coating display a lower hardness compared to the columnar ZrN and this question is investigated in paper I.

When Si content is higher than 7 at. %, the Zr-Si-N alloy form x-ray amorphous structure with a high oxidation resistance [31]. For a high Si content of 25 at. %, the amorphous structure display a high thermal stability with a stable hardness of 30 GPa up to an annealing temperature of 1100 °C [32].

4.4 Al-N

In the binary system, Aluminum nitride (AlN) is the only stable compound, and it has a predominant covalent bonding character [33]. The most stable phase of AlN is wurtzite structure with lattice parameters a, b = 3.78 Å and c = 4.98 Å [34], schematically shown in Fig. 4.3. The structure consists of each aluminum atom being surrounded by four nitrogen atoms, and vice- versa.

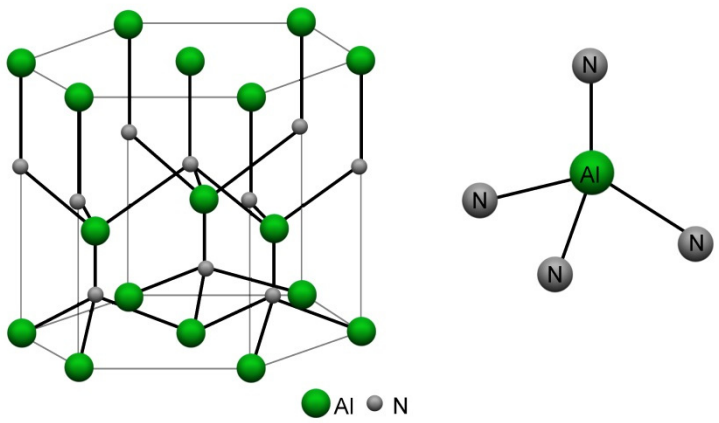

Figure 4.3 Wurtzite B4 crystal structure of AlN

The energy difference between wurtzite structure and the metastable cubic structure has been estimated to be only 0.18 eV/atom [35]. As a result, under favorable growth conditions, i.e. a domain size of less than 10 nm, and a right structural templating can cause AlN domains to form in a metastable cubic structure [36].

Mechanical properties of AlN coatings depend on its crystal structure. Coatings containing w-AlN display a lower hardness and lower elastic modulus of 17 GPa and 190 GPa respectively [37], and thus not preferred for wear resistant applications. In contrast, the coatings consisting of metastable c-AlN display high hardness [36] and high fracture toughness [38]. Furthermore, AlN offers a superior oxidation resistance by forming a protective α-Al_2O_3 layer [39] that acts as a diffusion barrier to oxidizing species. The combination of high oxidation resistance, and high hardness gives the pseudo-binary alloys of c- Al-TM-N such as c-Al-Ti-N, c-Al-Cr-N superior wear resistance [40].

4.5 Zr-Al-N

ZrAlN is an immiscible alloy with Gibbs free energy of mixing about 0.2 eV/atom with respect to c-ZrN and c-AlN [8]. However, the nonequilibrium growth conditions can form metastable cubic solid solution. Rogström et al., [41], have reported metastable c- ZrAlN up to 36 at. % Al, and a mixed cubic and wurtzite structure between 36 and 70 at. % Al, finally a solid solution of w-AlZrN above 70 at. % Al, in an arc evaporation process at a growth temperature around 400 °C.

When the metastable c-ZrAlN is subjected to elevated temperature annealing above 900 °C, the alloy decomposes to its equilibrium phases of c-ZrN and w-AlN [42].

Even though the theoretical calculations predict that the large miscibility gap of Zr-Al-N alloy should promote an intermediate isostructural decomposition pathway [43] similar to Ti-Al-N [44], there is no experimental proof. This discrepancy has been attributed to a large misfit strain of 12 % between c-ZrN and c-AlN hindering the coherent isostructural decomposition path way [43]. On the other hand the metastable w-AlZrN alloy has been reported to be thermally stable up to an annealing temperature of 1000 °C [45]. This causes a superior wear resistance during the metal cutting application [9].

The large immiscibility of the Zr-Al-N alloy is exploited here, to form chemically segregated c-ZrN and w-AlN domains during the growth. In addition, a process window is established to grow a self-organized inplane modulated structure. Based on this observation, a new generic material design approach is proposed and demonstrated to enhance the thermal stability of TM-Al-N alloy, a detailed discussion on this topic is presented in chapter 6 and paper IV.

In addition to the above mentioned binary and ternary material systems, a multi-component alloy of c-(TiAlCrNbV)N is synthesized to explore an entropy based alloy design, further details on this topic are presented separately in chapter 7.

References

[1] W. Kalss, A. Reiter, V. Derflinger, C. Gey, J.L. Endrino, Modern coatings in high performance cutting applications, Int. J. Refract. Met. Hard Mater. 24 (2006) 399–404.

[2] W.-D. Münz, Titanium aluminum nitride films: A new alternative to TiN coatings, J. Vac. Sci. Technol. A Vacuum, Surfaces, Film. 4 (1986) 2717.

[3] P.H. Mayrhofer, A. Hörling, L. Karlsson, J. Sjölén, T. Larsson, C. Mitterer, L. Hultman, Self-organized nanostructures in the Ti-Al-N system, Appl. Phys. Lett. 83 (2003) 2049–2051.

[4] R. Forsén, M.P. Johansson, M. Odén, N. Ghafoor, Effects of Ti alloying of AlCrN coatings on thermal stability and oxidation resistance, Thin Solid Films. 534 (2013) 394–402.

[5] S.K. Kim, P.V. Vinh, J.H. Kim, T. Ngoc, Deposition of superhard TiAlSiN thin films by cathodic arc plasma deposition, Surf. Coatings Technol. 200 (2005) 1391–1394.

[6] Y.-Y. Chang, H.-M. Lai, Wear behavior and cutting performance of CrAlSiN and TiAlSiN hard coatings on cemented carbide cutting tools for Ti alloys, Surf. Coatings Technol. 259 (2014) 152-158.

[7] L. Chen, D. Holec, Y. Du, P.H. Mayrhofer, Influence of Zr on structure, mechanical and thermal properties of Ti-Al-N., Thin Solid Films. 519 (2011) 5503–5510.

[8] D. Holec, R. Rachbauer, L. Chen, L. Wang, D. Luef, P.H. Mayrhofer, Surface & Coatings Technology Phase stability and alloy-related trends in Ti – Al – N , Zr – Al – N and Hf – Al – N systems from first principles, Surf. Coat. Technol. 206 (2011) 1698–1704.

[9] L. Rogström, M.P. Johansson-Jöesaar, L. Landälv, M. Ahlgren, M. Odén, Wear behavior of ZrAlN coated cutting tools during turning, Surf. Coatings Technol. 282 (2015) 180–187.

[10] E. Smagina, V.S. Kutsev, and B.F. Ormont, Equilibrium studies of Zr-N at high temperatures, J. Phys.Chem. 34 (1960) 1105-1114.

[11] P.L. Brown, E. Curti, B. Grambow. Chemical Thermodynamics of Zirconium, Elsevier (2005).

[12] PDF-card No. 00-035-0753. JCPDS-International Center for Diffraction data, 1998.

[13] PDF-card No. 00-038-0753. JCPDS-International Center for Diffraction data, 1998.

[14] L. Rogström, L.J.S. Johnson, M.P. Johansson, M. Ahlgren, L. Hultman, M. Odén, Thermal stability and mechanical properties of arc evaporated ZrN/ZrAlN multilayers, Thin Solid Films. 519 (2010) 694–699.

[15] Y. Dong, W. Zhao, Y. Li, G. Li, Influence of silicon on the microstructure and mechanical properties of Zr–Si–N composite films, Appl. Surf. Sci. 252 (2006) 5057–5062.

[16] M. Nose, W.A. Chiou, M. Zhou, T. Mae, M. Meshii, Microstructure and mechanical properties of Zr–Si–N films prepared by rf-reactive sputtering, J. Vac. Sci. Technol. A 20 (2002) 823.

[17] M. Lerch, E. Füglein, J. Wrba, Synthesis, crystal structure, and high temperature behavior of Zr3N4, Z. anorg. allg. Chem. 622 (1996) 367–372.

[18] M. Chhowalla, H.E. Unalan, Thin films of hard cubic Zr_3N_4 stabilized by stress, Nat. Mater. 4 (2005) 317–322.

[19] H. Okamoto, N-Si (Nitrogen-Silicon), J. Phase Equilibria Diffus. 26 (2005) 293–294.

[20] V. K. Sarin, On the α to β Phase Phase Transformation in Silicon Nitride, Matterials Sci. Eng. 106 (1988) 151–159.

[21] A. Zerr, G. Miehe, G. Serghiou, M. Schwarz, E. Kroke, R. Riedel, H. Fues, P. Kroll, R. Boehler, Synthesis of cubic silicon nitride, Lett. to Nat. 400 (1999) 340–342.

[22] B. Mikijelj, J. Mangels, E. Belfield, A. MacQueen, Silicon Nitride Applications in Modern Diesel Engines, SAE international article 01 (2004) 1448.

[23] M. Vila, D. Cáceres, C. Prieto, Mechanical properties of sputtered silicon nitride thin films, J. Appl. Phys. 94 (2003) 7868–7873.

[24] S. Veprek, M. Haussmann, S. Reiprich, L. Shizhi, J. Dian, Novel thermodynamically stable and oxidation resistant superhard coating materials, 87 (1996) 394–401.

[25] S. Vepřek, The search for novel, superhard materials, J. Vac. Sci. Technol. A 17 (1999) 2401.

[26] J. Patscheider, Nanocomposite Hard Coatings for Wear Protection, MRS bulletin march (2003) 180–183.

[27] T. Mae, M. Nose, M. Zhou, T. Nagae, K. Shimamura, The effects of Si addition on the structure and mechanical properties of ZrN thin films deposited by an r.f. reactive sputtering method, Surf. Coatings Technol. 142-144 (2001) 954–958.

[28] P.J. Martin, A. Bendavid, J.M. Cairney, M. Hoffman, Nanocomposite Ti–Si–N, Zr–Si–N, Ti–Al–Si–N, Ti–Al–V–Si–N thin film coatings deposited by vacuum arc deposition, Surf. Coatings Technol. 200 (2005) 2228–2235.

[29] G.P. Zhang, E.W. Niu, X.Q. Wang, G.H. Lv, L. Zhou, H. Pang, J. Huang, W. Chen, S.Z. Yang, Characterization of Zr–Si–N films deposited by cathodic vacuum arc with different N2/SiH4 flow rates, Appl. Surf. Sci. 258 (2012) 3674–3678.

[30] D. Pilloud, J.F. Pierson, A. P. Marques, A. Cavaleiro, Structural changes in Zr–Si–N films vs. their silicon content, Surf. Coatings Technol. 180-181 (2004) 352–356.

[31] M. Nose, M. Zhou, T. Nagae, T. Mae, M. Yokota, S. Saji, Properties of Zr . Si . N coatings prepared by RF reactive sputtering, Surf. Coatings Technol. (2000) 163–168.

[32] R. Daniel, J. Musil, P. Zeman, C. Mitterer, Thermal stability of magnetron sputtered Zr–Si–N films, Surf. Coatings Technol. 201 (2006) 3368–3376.

[33] H.A. Wriedt, The Al-N system, Bull. Alloy Phase Diag. 7(1986) 329-333.

[34] PDF-card No. 073-7288. JCPDS-International Center for Diffraction data, 1998.

[35] V. Chawla, D. Holec, P.H. Mayrhofer, The effect of interlayer composition and thickness on the stabilization of cubic AlN in AlN / Ti – Al – N superlattices, 565 (2014) 94–100.

[36] A. Madan, I.W. Kim, S.C. Cheng, P. Yashar, V.P. Dravid, S.A. Barnett, Stabilization of Cubic AlN in Epitaxial AlN - TiN Superlattices, (1997) 1743–1746.

[37] F. Jose, R. Ramaseshan, S. Tripura Sundari, S. Dash, A.K. Tyagi, M.S.R.N. Kiran, U. Ramamurthy, Nanomechanical and optical properties of highly a-axis oriented AlN films, Appl. Phys. Lett. 101 (2012) 254102.

[38] M. Schlo, C. Kirchlechner, J. Paulitsch, J. Keckes, P.H. Mayrhofer, Effects of structure and interfaces on fracture toughness of CrN / AlN multilayer coatings, Scr. Mat. 68 (2013) 917–920.

[39] V.A. Lavrenko, A.F. Alexeev, Oxidation of Sintered Aluminium Nitride, Cer. Int. 9 (1800) 80–82.

[40] A. Inspektor, P.A. Salvador, Architecture of PVD coatings for metalcutting applications: A review, Surf. Coatings Technol. 257 (2014) 138–153.

[41] L. Rogström, M.P. Johansson, N. Ghafoor, L. Hultman, M. Odén, Influence of chemical composition and deposition conditions on microstructure evolution during annealing of arc evaporated ZrAlN thin films, J. Vac. Sci. Technol. A. 30 (2012) 031504.

[42] L. Rogström, M. Ahlgren, J. Almer, L. Hultman, M. Odén, Phase transformations in

nanocomposite ZrAlN thin films during annealing, J. Mater. Res. 27 (2012) 1716–1724.

[43] S.H. Sheng, R.F. Zhang, S. Veprek, Phase stabilities and thermal decomposition in the Zr1-xAlxN system studied by ab initio calculation and thermodynamic modeling, Acta Mater. 56 (2008) 968–976.

[44] P.H. Mayrhofer, A. Hörling, L. Karlsson, J. Sjölén, T. Larsson, C. Mitterer, L. Hultman, Self-organized nanostructures in the Ti-Al-N system, Appl. Phys. Lett. 83 (2003) 2049–2051.

[45] L. Rogström, N. Ghafoor, J. Schroeder, N. Schell, J. Birch, M. Ahlgren, et al., Thermal stability of wurtzite Zr1–xAlxN coatings studied by in situ high-energy x-ray diffraction during annealing, J. Appl. Phys. 118 (2015) 035309.

5. Characterization

A wide range of structural characterization techniques such as x-ray diffraction, scanning electron microscope, transmission electron microscope, atom probe tomography, focused ion beam work station, have been used in the current work. These techniques are quite mature, well presented in the literature and briefly introduced in the experimental section of the corresponding papers.

In contrast, mechanical property evaluation of few micron thin coating is a challenging task, and almost none of the bulk form testing methods could be directly applied due to size limitations. A standard test method of hardness measurement using nanoindentation technique has been established only a few years ago [1], and till date, there is no standardized method available to quantify the fracture resistance. To address this challenge, a wide range of techniques, such as straining the free standing coating [2], scratch [3], and *in situ* micro pillar compression [4,5] methods are being explored.

In this work, a simple indentation based methodologies have been developed to probe the deformation behavior and fracture resistance of thin coatings which is presented in the following section. The indentation is performed with both Berkovich and Cube Corner indenter geometries that corresponds to equivalent cone angles of 70.3° and 42.3° with an axisymmetric indentation strain of 8 and 22 %, respectively [6].

5.1 Deformation behavior

The following protocol is used to investigate the indentation-induced deformation behavior of few micron thin coatings.

Polished coating surface → Indentation → Surface topography imaging of the imprint using AFM → Thin lamella extraction beneath the indent → TEM examination of the markers displacement.

This method is implemented in paper I to visualize transition in the deformation mechanism between columnar ZrN and nanocomposite Zr-Si-N coating.

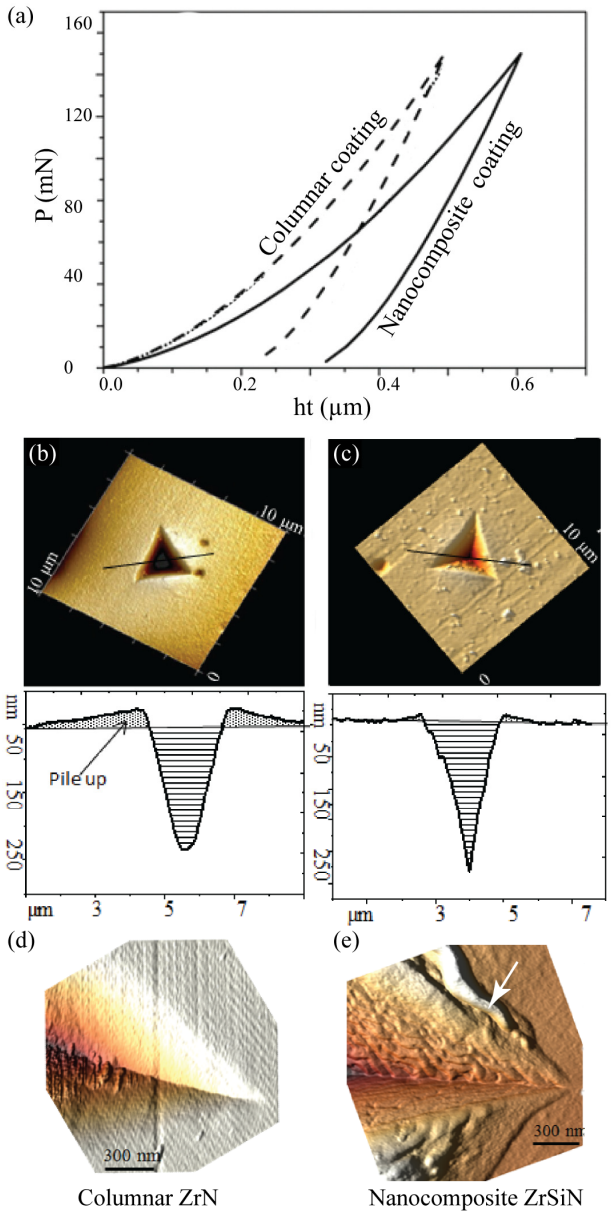

Figure 5.1. (a) P-h curves of columnar ZrN, and nanocomposite Zr-Si-N coating. Overview AFM image of the indent along with cross-sectional line profile and magnified AFM image at the edge of the indent for (b, d) columnar ZrN, and (c, e) Zr-Si-N nanocomposite coating. White arrow indicate bands long the edge of the imprint.

Both the coatings are subjected to an indentation force of 150 mN to form an imprint that is large enough for postmortem investigations but without causing fracture.

Load (P) - depth (h) curves of columnar and nanocomposite coatings are shown in Fig. 5.1a. Columnar structured coatings show lower contact depth indicating its higher hardness compared to the nanocomposite coating, but the P-h curves do not reveal any additional feature.

AFM image and the cross-sectional line profile of the indents for both the coatings show a large material pile up for the columnar structure (Fig.5.1b), but not for the nanocomposite coating (Fig. 5.1c). To understand this, the topography of the indented surface is imaged at higher magnification which shows some bands aligned parallel to the edge of the indent cavity for the nanocomposite coating (Fig. 5.1 e), while the columnar structured coating does not display any features. To investigate these bands further, thin lamellae have been extracted below the indent and visualized in TEM as shown in Fig. 5.2. BF-TEM image does not provide any deformation related contrast (Fig. 5.2a). This issue has been solved by switching to HAADF contrast, where the lamellae display rotation induced artificial layering contrast [7]. These layers are used as markers to follow the displacement events under the indent as shown in Fig. 5.2b and Fig. 5.2e. Note that the markers display localized sliding events in the nanocomposite coating (Fig. 5.2c), whereas the layers in the columnar structured coating shows a uniform compression

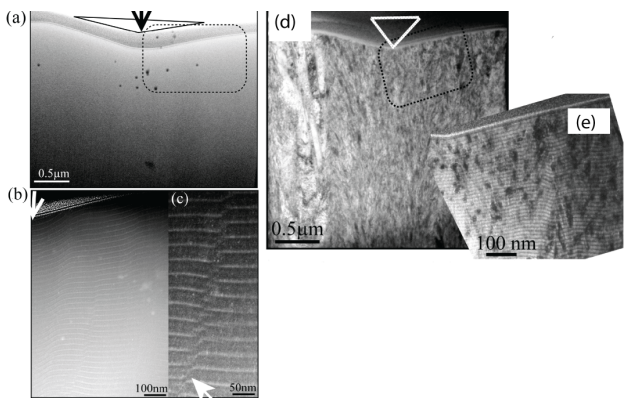

Figure 5.2. (a, d) BF-TEM, and (b, c, and e) HAADF STEM analysis of the lamellae extracted below the indent. (a, b and c) Zr-Si-N nanocomposite, (d and e) columnar ZrN. White arrow in Fig. c indicates localized layer sliding.

(Fig. 5.2e, for details refer paper I). These observations at different length scale points to the difference in deformation mechanism between columnar and nanostructured coatings. The strain localization of the nanocomposite structure is attributed to grain boundary mediated deformation mechanism which has resulted in shear bands on the edges of the indent surface (Fig. 5.1 e). In contrast, the uniform marker compression for the columnar structure has been attributed to dislocation dominant deformation mechanism, where out of plane dislocation glide causes higher material pile up. Further details are discussed in paper I.

5.2 Fracture resistance:

Fracture resistance of the coatings is evaluated by subjecting them to high contact force with a sharp indenter to develop well defined cracks. Two different methods, namely a displacement controlled qualitative method, and load controlled semi-quantitative methods have been developed in this work. In the qualitative method, coatings are subjected to controlled indentation using cube corner indenter to cause fracture followed by SEM imaging of FIB cut cross-sections to compare cracking morphology and crack density.

This method is applied to arc evaporated Zr-Si-N coatings with a thickness about 4 μm, shown in Fig 5.3. The fracture resistance is compared between columnar ZrN and nanocomposite Zr-Si-N coatings by subjecting them to the same indentation strain. The plan view micrograph of the indent surface shows well developed radial cracks for the nanocomposite coating (Fig. 5.3 b), indicating its lower fracture resistance compared to the columnar structured coating (Fig. 5.3 a). The lower fracture resistance of nanocomposite coating appears to be counterintuitive because of its lower hardness compared to the columnar structured coating (Fig. 5.1). However, the cross-sectional SEM micrograph after the FIB cut solve this puzzle by

revealing crack deflection and branching for the columnar structured coating (Fig. 5.3 c) but not for the nanocomposite coatings (Fig. 5.3 d).

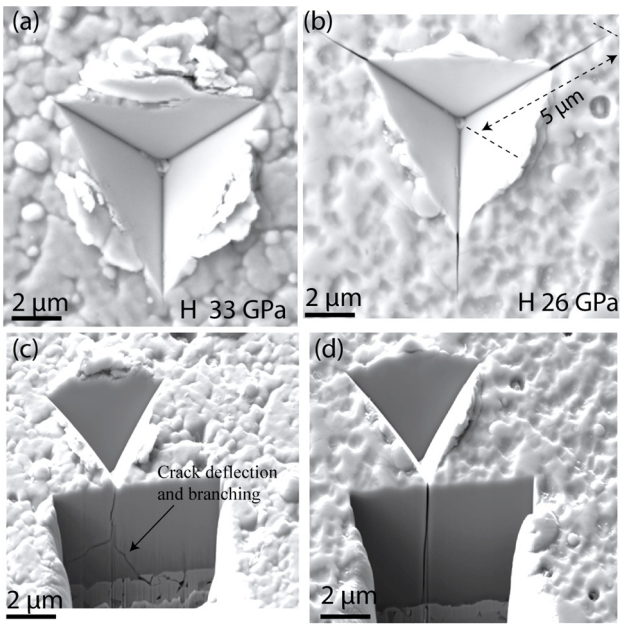

Figure 5.3. SEM micrographs of plan-view and FIB cut cross-sections: (a, c) columnar ZrN, and (b, d) nanocomposite Zr-Si-N coating

The crack deflection and branching offers additional energy dissipation which results in higher fracture resistance of the columnar ZrN coatings in spite of its higher hardness.

A well-developed radial crack emanating from the edge of the imprint in the nanocomposite coating allows estimation of fracture toughness K_c, by measuring the length of radial cracks using the equation formulated by Lawns, Evans and Marshall [8] for the bulk form ceramic materials as,

$$K_C = \alpha \left(\frac{E}{H}\right)^{1/2} \left(\frac{P}{c^{3/2}}\right) \quad (1)$$

α is an empirical constant based on indenter geometry, P is the maximum applied load, E is the elastic modulus of the coating and H is the hardness of the coatings and c is the length of the radial crack. A well-developed radial crack for the nanocomposite coating with a length of 5 µm (Fig. 5.3b) is estimated to K_c value of 8 MPa √m. This value has been found to be overestimated compared to K_{IC} value of 2.5 MPa √m measured by a validated pillar compression technique for similar materials [5]. This indicates that the existing quantitative indentation methods may not be suitable to get a reliable K_{IC} estimation of thin coatings. Furthermore, the indentation strain does not necessarily develop radial cracks in all the hard coating materials.

To overcome this challenge, an indentation based semi-quantitative method has been developed with the following protocol to provide a reliable comparison of fracture resistance between different coatings.

Polished coating surface → Indentation array with force ramp up → estimating the critical force following SEM examination

This technique is applied to evaluate the fracture resistance of ZrN/ZrAlN multilayer grown to a thickness of 1 μm on MgO substrate. An indentation array is made with a Berkovich indenter as shown in Fig. 5.4a.

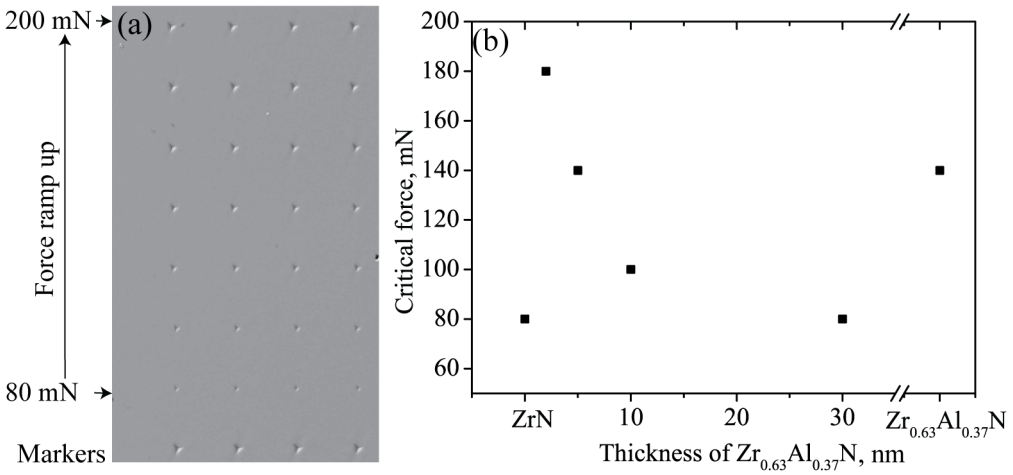

Figure 5.4. A semi-quantitative method of evaluating fracture resistance, (a) indentation array on coating with force ramp up between 80 mN and 200 mN, and (b) critical force needed to observe the first surface crack of ZrN/ZrAlN multilayer as a function of ZrAlN layer thickness.

The contact force has been varied between 80 mN and 200 mN at an increment of 20 mN. Four indents are made at each force at a distance of 30 μm between the indents. A critical force to cause the first observable surface crack around the indent is reported following the SEM imaging of the indentation array. Care has been taken to align one of the sides of the equilateral triangular imprint along MgO <110> while indenting, to avoid any substrate anisotropic effects on the measured fracture resistance. Figure 5.4b shows the measured critical force of ZrN/ZrAlN multilayer, as a function of ZrAlN layer thickness, where the multilayer with 2 nm ZrAlN layer shows the highest critical force.

To further validate this method, all the coatings are subjected to the same force of 200 mN and the crack density has been compared between different coatings as shown in Fig. 5.5. Interestingly, the observed crack density around the indent surface follows the same trend of measured critical force shown in Fig. 5.4b, where the multilayer of ZrN/ZrAlN with 2 nm (Fig. 5.5 c) shows negligible cracking and the

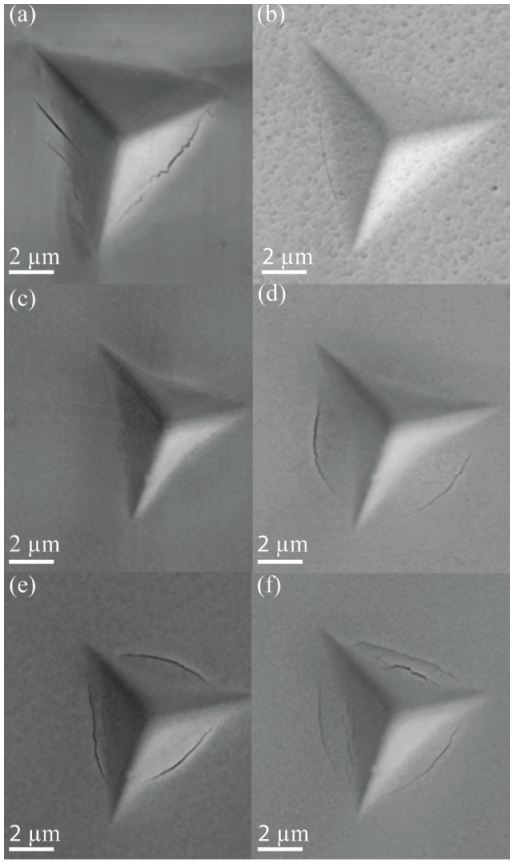

Figure 5.5. Indentation-induced surface cracks at a force of 200 mN, monolithic of (a) ZrN, (b) ZrAlN and multilayer of ZrN/ZrAlN with ZrAlN layer thickness of (c) 2 nm, (d) 5 nm, (e) 10 nm and (f) 30 nm.

multilayer with 30 nm ZrAlN layer (Fig. 5.5 f) thickness shows significantly higher cracking. A detailed discussion of toughening mechanisms responsible for the higher fracture resistance of the multilayer with 2 nm ZrAlN is presented in paper II.

5.3 Wear resistance:

Even though the coatings have high hardness, high fracture resistance, and excellent oxidation resistance, ultimately they must display a superior wear resistance for a given contact sliding condition. To probe the contact sliding response of the Zr-Si-N coatings (paper II), reciprocating contact sliding wear tests were performed in a SRV Optimal wear test machine using a ball-on-disc configuration equipped with sample heating stage. The test set up is shown in Fig. 5.6, where the electro-mechanical drive oscillates the upper specimen against the lower disc by using a spring deflection loading arrangement. For all the tests in this study, coatings were deposited only on the lower disc and the upper uncoated ball acts as a counter surface. The computerized control and data acquisition system enables control over stroke length, frequency, load, temperature and duration. It also records the frictional force by a pair of piezoelectric force transducers. The contact pressure between the spherical ball and the flat coated sample was estimated using the Hertz equation.

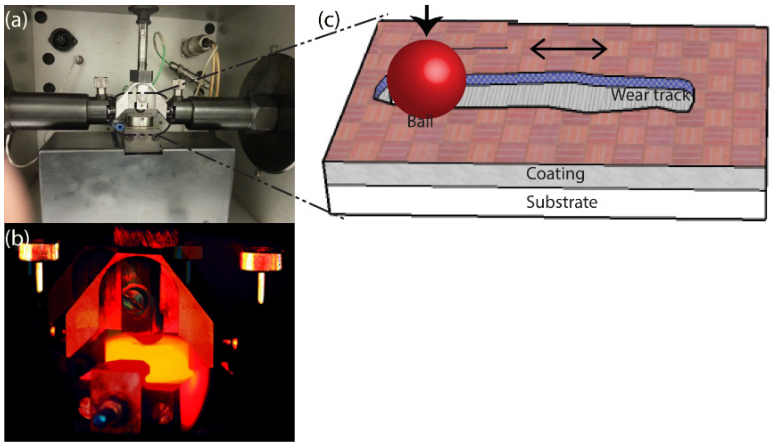

Figure 5.6. SRV Optimal wear testing set up with ball on disc configuration at (a) room temperature, (b) elevated temperature, and (c) schematic representation of wear track formation.

By varying the test conditions, the tribological response of Zr-Si-N coatings were scanned under macro and microscale wear tests. Microwear tests were performed on a polished coating surface using a diamond conical indenter with a nominal tip radius of 5 µm in a Triboindenter® TI-950 from Hysitron in a multipass nanoscratch test configuration, equipped with *in situ* scanning probe imaging. The results are summarized in Fig. 5.7 and further details are presented in paper II. The results reveal that for the same contact pair of Zr-Si-N coating and WC-Co, the dominant wear mechanism switch between tribo-oxidation and plastic deformation depending on the contact temperature and contact stress (Ref. paper II). As a consequence, the favorable microstructure and mechanical property combination of a coating that display a superior wear resistance is unique for every contact condition, and must be investigated individually.

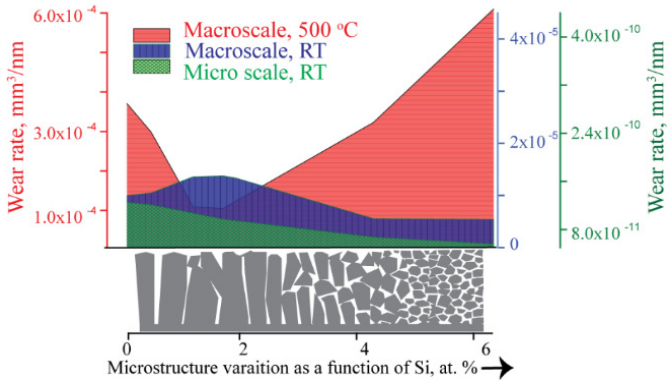

Figure 5.7. Wear resistance of Zr-Si-N coatings as a function of microstructure variation under varied contact sliding conditions.

References:

[1] ISO 14577-4:2007(en), Instrumented indentation test for ahrdness and materials parameters- Part 4. Test method for metallic and non-metallic coatings.

[2] R. Keller, J. Phelps, D. Read, Tensile and fracture behavior of free-standing copper films,

Mater. Sci. Eng. A. 214 (1996) 42–52.

[3] S. Zhang, D. Sun, Y. Fu, H. Du, Toughness measurement of thin films: A critical review, Surf. Coatings Technol. 198 (2005) 74–84.

[4] S. Liu, J.M. Wheeler, P.R. Howie, X.T. Zeng, J. Michler, W.J. Clegg, Measuring the fracture resistance of hard coatings, Appl. Phys. Lett. 102 (2013) 1–5.

[5] M. Sebastiani, K.E. Johanns, E.G. Herbert, F. Carassiti, G.M. Pharr, A novel pillar indentation splitting test for measuring fracture toughness of thin ceramic coatings, Philos. Mag. 0 (2014) 1–17.

[6] A.C Fischer-Cripps, Nanoindentation, third edition, Springer (2011).

[7] A.O. Eriksson, J.Q. Zhu, N. Ghafoor, M.P. Johansson, J. Sjölen, J. Jensen, M.Odén, L. Hultman, J. Rosén, Layer formation by resputtering in Ti-Si-C hard coatings during large scale cathodic arc deposition, Surf. Coatings Technol. 205 (2011) 3923–3930.

[8] B.R. Lawn, A.G. Evans, Elastic /Plastic indentation damage in ceramics: The median / radial crack system, Journal of Amer. Cer. Soc. 63. (1980) 574.

6. Thermal stability of TM-Al-N coatings, and the issue of w-AlN

6.1 TM-Al-N coatings

TM-Al-N coatings such as Ti-Al-N, and Cr-Al-N are the current workhorse materials for a large number of metal cutting and wear resistant applications [1,2]. This is a direct consequence of their high oxidation resistance combined with a high hardness, and fracture resistance associated with formation of the metastable phases [3].

6.2 Metastable c-TM-Al-N coating and their limited thermal stability

TMN and AlN are immiscible materials with a maximum Gibbs free energy of mixing between 0.06 eV/atom and 0.18 eV/atom, depending on the material system [4,5]. Nevertheless, the non-equilibrium growth conditions of plasma-assisted PVD process forms a metastable solid solution of c-TM-Al-N alloy up to 70 at. % Al [3,6,7].

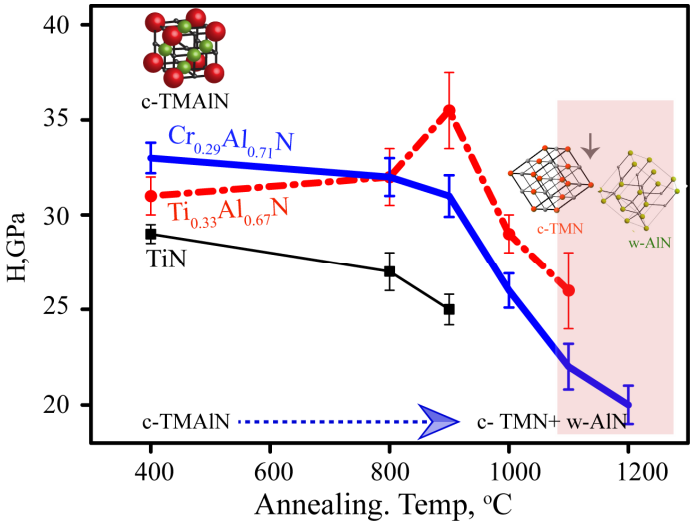

Figure 6.1. Hardness variation of TM-Al-N coatings as a function of annealing temperature, data is taken from [6,12].

However, when these coatings are subjected to elevated temperature, the metastable cubic solid solution decomposes to their equilibrium phase mixture of c-TMN and w-AlN[2]. This transformation is associated with a molar volume expansion about 20 % [8] causing an undesirable structural instability.

[2] Metastable solid solution of c- TiAlN with Al content > 40 at. %, undergo an intermediate isostructural decomposition to c-TiN and metastable c-AlN before the formation of equilibrium phase mixture [5].

Furthermore, the phase transformation also affects the coating hardness. Figure 6.1 shows hardness variation as a function of annealing temperature for several TM-Al-N coatings, where $Cr_{0.29}Al_{0.71}N$ display relatively stable hardness up to a temperature of 900 °C, while $Ti_{0.33}Al_{0.67}N$ shows self-hardening[3] between 800 °C and 900 °C. Most importantly, both coatings display a steep hardness drop at a temperature above 900 °C. This hardness drop has been attributed to formation of w-AlN [6,9].

To overcome this challenge, the current research strategy is to postpone the onset temperature of w-AlN formation by several sophisticated approaches such as multicomponent alloying [10,11], multilayering [12], and interface coherency strain tuning [13]. Nevertheless, there is a temperature limit around 1000 °C, above which the thermodynamically stable wurtzite phase forms and correspondingly a lower hardness of the coating. This remains as a long-standing challenge in the field.

6.3 A new material design to enhance the thermal stability of TM-Al-N

Even though it is well acknowledged that the w-AlN phase formation is detrimental to hardness in the TM-Al-N coatings [7,14,15], the mechanism by which this happens is not known precisely which will be examined here. A stress-strain relationship using first principle calculation has revealed a similar ideal shear strength between c-AlN and w-AlN [16]. This indicates that the lower hardness associated with w-AlN phase formation is not an intrinsic effect.

On the other hand, previous studies of elevated temperature annealed TiAlN [17] and CrAlN coatings [18] reveal that the precipitation of w-AlN phase evolves a nanocomposite structure with a domain size of about 15nm having incoherent interfaces, in place of continues coherent lattice. When such a nanocomposite structure is subjected to external mechanical force, such as indentation, the dislocation-induced plasticity is constrained by incoherent interfaces, as they are opaque to the gliding dislocations [19]. As a result, the material looks for an alternative deformation mechanism to relieve the strain energy induced by external forces.

The incoherent interfaces between c-TiN, and w-AlN being weak in shear [20], may likely favor an interface mediated deformation mechanism when the interface volume

[3] Self-hardening of c-TiAlN is a result of formation of nanoscale isostructural domains of c-TiN, and metastable c-AlN with coherent lattice [14].

is sufficiently high in the nanocomposite. This has been schematically presented in chapter 2 (Fig. 2.3a), and causes strain localization that leads to a lower hardness similar to the grain size softening effect in a nanocrystalline TiN [21]. The above discussion suggests that the reduced hardness of TM-Al-N coating consisting of w-AlN phase with incoherent interfaces, is an extrinsic effect that is related to the interface structure.

In this work it is shown that the w-AlN phase is not detrimental to hardness, instead the coating comprising of w-AlN display a high shear resistance and consequently a higher hardness, provided if it is grown coherently to c-TMN. This is experimentally shown for the multilayer of TiN/ZrAlN (paper IV), where the ZrAlN form nanoscale segregated domains of c-ZrN and w-AlN with coherent interfaces.

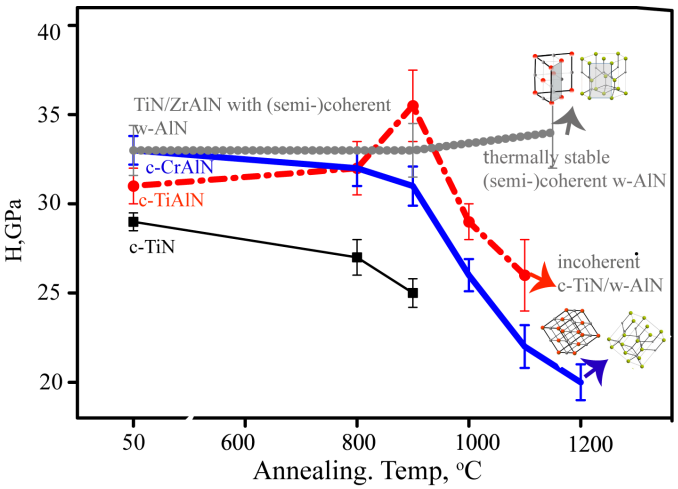

Figure 6.2. Hardness of TM-Al-N coatings as a function of annealing temperature, data is taken from [6] *and paper IV.*

Figure. 6.2 shows hardness variation as a function of annealing temperature for different TM-Al-N coatings. The important observation is that the multilayer of TiN/ZrAlN with coherent interfaces display a high and stable hardness of ~ 34 ± 1.5 GPa even after elevated temperature annealing of 1150 °C, and this is 50 % higher compared to the state of the art metastable c- Ti-Al-N, and c- Cr-Al-N alloys that forms w-AlN with incoherent interfaces (Fig. 6.2). A high hardness of the coating consisting w-AlN phase with coherent interfaces is attributed to (a) suppression of the coordinated shear displacement in the nanocomposite structure, and b) spatial fluctuations in shear modulus between the coherent domains of c-TiN and w-AlN offer Koehler strengthening [22], and the misfit strain across the coherent interfaces offer coherency strengthening [23] similar to the iso-structurally decomposed c-TiAlN alloy. Furthermore, it has been found that the non-isostructural coherent interfaces between w-AlN, and c-TiN, c-ZrN are thermally stable even up to an experimentally limited annealing temperature of 1150 °C.

To understand the high thermal stability of the interfaces, the relative thermodynamic stability is compared between isostructural and non-isostructural coherent interfaces for TiN/AlN, and ZrN/AlN multilayer using first principle calculations as shown in Fig. 6.3. The calculation details are presented in paper IV.

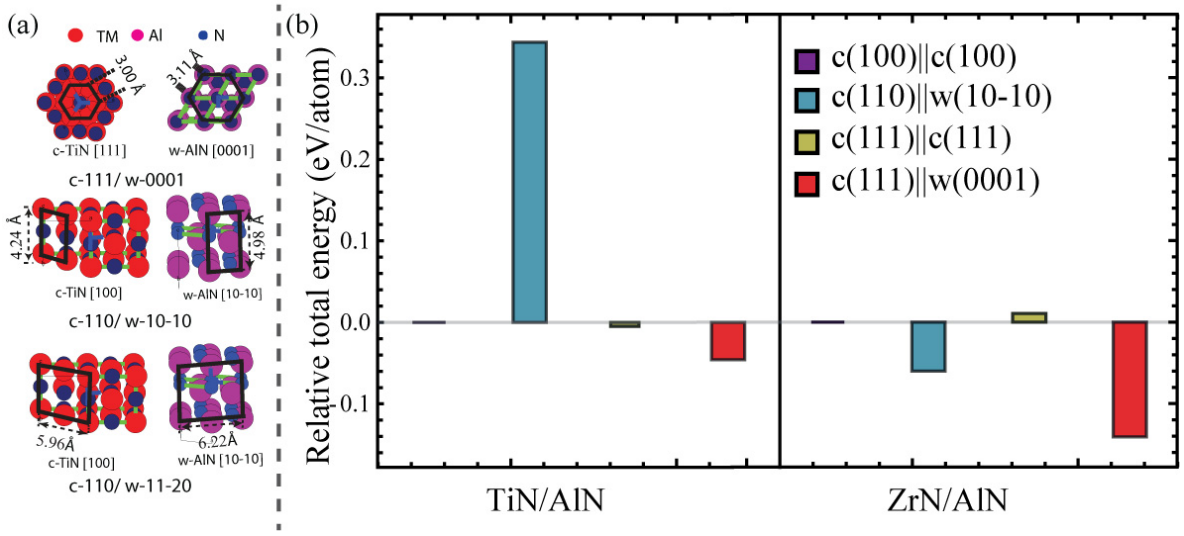

Figure 6.3. (a) Three possible coherent orientation relationships between c-TMN and w-AlN, (b) Ab-initio calculated energy (eV/atom) comparison between isostructural and non-isostructural interfaces for the multilayers of TiN/AlN and ZrN/AlN relative to c-TMN(100) || c-AlN(100). Calculation results are in collaboration with Fei. Wang.

There are three possible coherent orientation relationships between non-isostructural domains of c-TMN and w-AlN as shown in Fig. 6.3a. The calculated results reveal that the coherent orientation of c- (110) || w- (10-10) is only favorable for the ZrN/AlN, whereas the orientation of c- (111) || w- (0001) is energetically favorable for both the material systems. These results clearly indicate that the non-isostructural interfaces between c-TMN and w-AlN display high thermodynamic stability when the interface structure is appropriately tuned.

The above results lead me to propose a generic material design concept to achieve a high thermal stability in the TM-Al-N coating by forming a structural archetype of c-TMN/w-AlN with coherent interfaces. The next obvious question is how to grow these structures.

6.4 How to grow coherent interfaces between c-TMN and w-AlN.

The interface structure between two different phases in a material can be switched between coherent and incoherent type, by tuning the domain size via altering the interface and elastic strain energies [24]. When the domains are smaller, the interface volume, and correspondingly the interface energy is high. As a result, the interface

energy minimization favors coherent interfaces for smaller domain size [25]. However, the coherent interfaces generate an energy penalty in the form of elastic strain energy associated with the structural misfit between the two different domains across the coherent interface. The competition between interface energy and elastic strain energy sets a critical domain size below which only the coherent interfaces become thermodynamically favorable [25].

Even though the critical size is not known precisely, the non-isostructural coherent interfaces between w-AlN and c-TiN, c-ZrN, are formed at a domain size[4] about 15 nm in the multilayer of TiN/ZrAlN. Nevertheless, the coherent interface formation between non-isostructural domains is only possible for specific crystallographic orientations as shown in Fig. 6.3 a. This is a direct consequence of difference in the crystallographic symmetries between cubic B1 structure and wurtzite B4 structure. In summary, thermodynamic conditions for the coherent interface formation between w-AlN and c-TMN are fulfilled by growing them at an optimal domain size, with a favorable crystallographic orientation.

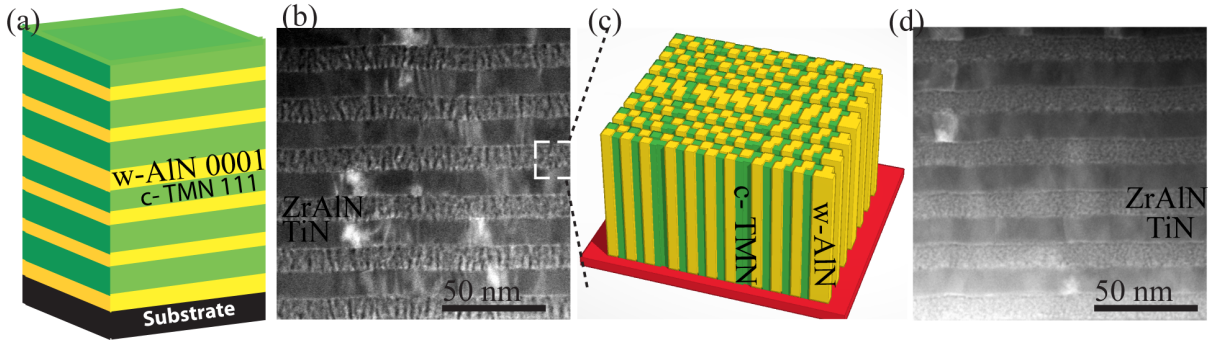

Figure 6.4. (a) Schematic representation of the multilayer to form non- isostructural coherent interfaces, (b) cross-sectional view (s)TEM image of TiN/ZrAlN multilayer grown at 900 °C, (c) schematic representation of inplane modulated structure, and (d) cross-sectional view (s)TEM image of TiN/ZrAlN multilayer grown at 700 °C with a random segregation.

Figure. 6.4 shows two different ways of growing the non-isostructural coherent interfaces. In a multilayer (Fig. 6.4 a), consisting of alternative layers of c-TMN and w-AlN, when the c-TMN layer is formed with a favorable crystallographic orientation, for example, with (111) orientation in the growth direction, the interface energy minimization causes adatoms in the next AlN layer to adapt (0001) orientation with coherent interfaces up to a critical layer thickness due to their close crystallographic symmetry.

[4] When AlN domains are too small (< 10 nm), they are formed in metastable cubic phase [17].

The same thermodynamic driving force of interface energy minimization, causes a structural and chemical inplane modulation with coherent interfaces in the multilayer of TiN/ZrAlN on MgO (001) surface. At a growth temperature of 900 °C, the large immiscibility combined with a high adatom mobility causes ZrAlN to segregate in to c-ZrN and w-AlN domains during the growth. The templating effect of MgO (001) surface causes c-ZrN to attain (002) orientation in the growth direction, causing coherent interfaces between c-ZrN (110) and w-AlN (10-10) in the lateral direction. This creates a self-aligned and inplane modulated structure as shown in Fig. 6.4b and c. Growth temperature plays an extremely important role to achieve this structure. For example, at a growth temperature of 700 °C, the insufficient adatom mobility at the growth front leads to incoherent interfaces between ZrN and AlN domains that lead to a random chemical segregation as shown in Fig. 6.4 d. Recently, a similar self-organized non-isostructural coherent interfaced c-TiN/w-AlN has been reported even on a polycrystalline substrate in a CVD process at a growth temperature of 800 °C [26].

6.5 Material choice for the structural archetype c-TMN/w-AlN with coherent interface

Even though the proposed structural archetype of c-TMN/w-AlN with coherent interfaces is a generic material design concept, the thermal stability, and perhaps the hardness of the structure could be tuned by switching between different family members of c-TMN or even by alloying between them.

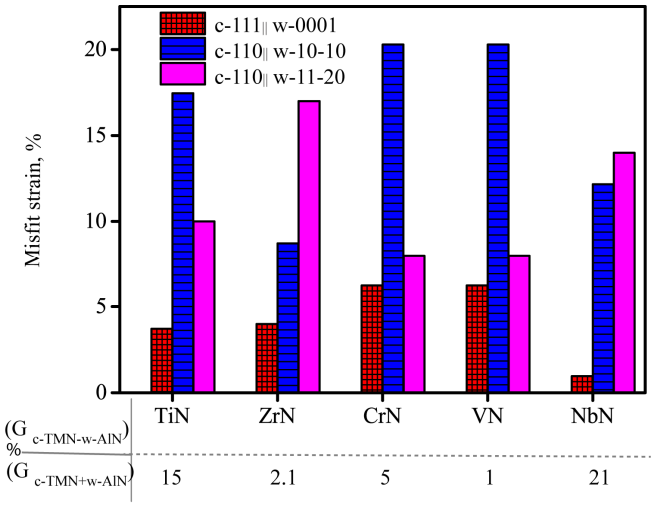

Figure 6.5. Calculated misfit strain between different coherent orientation of c-TMN/w-AlN, and the bottom table shows an estimated shear modulus difference for the coherent orientation of c-TMN(111) || w-AlN(0001) for different TMN materials.

The thermodynamic stability of the interface structure constitutes two components [27]: (a) interface chemistry, and (b) misfit strain. The evaluation of the first part is more complex and requires heavy computational support, while the latter part is relatively simple. Figure 6.5 compares the misfit strain for the three possible coherent

orientations between w-AlN and different family members of c-TMN.

The calculations show that the coherent orientation of c- 111 || w- 0001 display the lowest misfit strain, and for this orientation, NbN provides the lowest misfit strain compared to other c-TMN materials. However, a lower misfit strain may also likely to result a reduced coherency strengthening, but this is offset by a high shear modulus difference of 21 % (Fig. 6.5) offering the highest Koehler strengthening compared to any other TMN material. In summary, the coherent interface of c- NbN (111)||w-AlN (0001) is a favorite material system for the proposed new structural archetype. A lower misfit strain may result, a high thermodynamic stability, and a high shear modulus difference between c-NbN and w-AlN might lead to a high hardness.

References:

[1] S. Paldey, S.C. Dee, Single layer and multilayer wear resistant coatings of (Ti,Al)N: a re view, Materials Science and Engineering, 342 (2003) 58–79.

[2] W. Kalss, A. Reiter, V. Derflinger, C. Gey, J.L. Endrino, Modern coatings in high performance cutting applications, Int. J. Refract. Met. Hard Mater. 24 (2006) 399–404.

[3] A. Inspektor, P.A. Salvador, Architecture of PVD coatings for metalcutting applications: A review, Surf. Coatings Technol. 257 (2014) 138–153.

[4] D. Holec, R. Rachbauer, L. Chen, L. Wang, D. Luef, P.H. Mayrhofer, Surface & Coatings Technology Phase stability and alloy-related trends in Ti – Al – N , Zr – Al – N and Hf – Al – N systems from first principles, Surf. Coat. Technol. 206 (2011) 1698–1704.

[5] B. Alling, T. Marten, I.A. Abrikosov, A. Karimi, Comparison of thermodynamic properties of cubic Cr_{1-x} Al_x N and Ti1-x Alx N from first-principles calculations, J. Appl. Phys. 102 (2007).

[6] A.E. Reiter, V.H. Derflinger, B. Hanselmann, T. Bachmann, B. Sartory, Investigation of the properties of Al1-xCrxN coatings prepared by cathodic arc evaporation, Surf. Coatings Technol. 200 (2005) 2114–2122.

[7] R. Franz, M. Lechthaler, C. Polzer, C. Mitterer, Structure, mechanical properties and oxidation behaviour of arc-evaporated NbAlN hard coatings, Surf. Coatings Technol. 204 (2010) 2447–2453.

[8] Q. Xia, H. Xia, A.L. Ruoff, Pressure-induced rocksalt phase of aluminum nitride: A metastable structure at ambient condition, J. Appl. Phys. 73 (1993) 8198.

[9] A. Hörling, L. Hultman, M. Odén, J. Sjölén, L. Karlsson, Thermal stability of arc evaporated high aluminum-content $Ti_{[1-x]}Al_{[x]}N$ thin films, J. Vac. Sci. Technol. A. 20 (2002) 1815-1823.

[10] L. Chen, D. Holec, Y. Du, P.H. Mayrhofer, Influence of Zr on structure, mechanical and thermal properties of Ti-Al-N, Thin Solid Films. 519 (2011) 5503–5510.

[11] R. Rachbauer, A. Blutmager, D. Holec, P.H. Mayrhofer, Effect of Hf on structure and age hardening of Ti-Al-N thin films, Surf. Coatings Technol. 206 (2012) 2667–2672.

[12] A. Knutsson, M.P. Johansson, L. Karlsson, M. Odén, Thermally enhanced mechanical properties of arc evaporated $Ti_{[0.34]}Al_{[0.66]}N$/TiN multilayer coatings, J. Appl. Phys. 108 (2010) 044312.

[13] R. Forsén, N. Ghafoor, M. Odén, Coherency strain engineered decomposition of unstable multilayer alloys for improved thermal stability, J. Appl. Phys. 114 (2013) 244303.

[14] P.H. Mayrhofer, A. Hörling, L. Karlsson, J. Sjölén, T. Larsson, C. Mitterer, L. Hultman, Self-organized nanostructures in the Ti-Al-N system, Appl. Phys. Lett. 83 (2003) 2049–2051.

[15] H. Willmann, Thermal stability of Al – Cr – N hard coatings, Scr. Mater. 54 (2006) 1847–1851.

[16] R.F. Zhang, S.H. Sheng, S. Veprek, First principles studies of ideal strength and bonding nature of AlN polymorphs in comparison to TiN, Appl. Phys. Lett. 91 (2007)031906.

[17] N. Norrby, L. Rogström, M.P. Johansson-Jõesaar, N. Schell, M. Odén, In situ X-ray scattering study of the cubic to hexagonal transformation of AlN in $Ti_{1-x}Al_xN$, Acta Mater. 73 (2014) 205–214.

[18] R. Forsén, M.P. Johansson, M. Odén, N. Ghafoor, Effects of Ti alloying of AlCrN coatings on thermal stability and oxidation resistance, Thin Solid Films. 534 (2013) 394–402.

[19] K. Lu, L. Lu, S. Suresh, Strengthening materials by engineering coherent internal boundaries at the nanoscale, Science. 324 (2009) 349–352.

[20] H.M. Zbib, C.T. Overman, F. Akasheh, D. Bahr, Analysis of plastic deformation in nanoscale metallic multilayers with coherent and incoherent interfaces, Int. J. Plast. 27 (2011) 1618–1639.

[21] H. Conrad, J. Narayan, K. Jung, Grain size softening in nanocrystalline TiN, Int. J. Refract. Met. Hard Mater. 23 (2005) 301–305.

[22] J.S. Koehler, Attempt to design a strong solid, Phy. Rev. B 2 (1970) 547.

[23] J.W. Cahn, Hardening by spinodal decomposition, Acta Metall. 11 (1963) 1275–1282.

[24] S.J. Lloyd, J.M. Molina-Aldareguia, Multilayered materials: a palette for the materials artist, Philos. Trans. A. Math. Phys. Eng. Sci. 361 (2003) 2931–2949.

[25] B.M. Clemens, H. Kung, S.A. Barnett, Structure and strength of multilayers, MRS Bull. (1999) 20–26.

[26] J. Keckes, R. Daniel, C. Mitterer, I.Matko, B. Sartory, A. Koepf, R.Weißenbacher, R.Pitonak, Self-organized periodic soft-hard nanolamellae in polycrystalline TiAlN thin films, TSF 545 (2013) 29-32.

[27] S.K. Yadav, S. Shao, J. Wang, X.-Y. Liu, Structural modifications due to interface chemistry at metal-nitride interfaces., Sci. Rep. 5 (2015) 17380.

7. High entropy alloys

7.1. High entropy alloy (HEA) concept:

For several centuries, the alloy design has been primarily based on one or two principal elements with small addition of other alloying elements. According to Gibbs phase rule, the maximum number of phases in thermodynamic equilibrium increases with the total number of components in an alloy [1]. This means alloys with higher number of elements may generate more intermetallics and ordered phases. In contrast to this, multi-principal element alloys with more than 5 and up to 20 elements have surprisingly formed in simple solid solutions, reported by B. Cantor and J.W. Yeh et al. [2,3] independently. Yeh et al. [2] have attributed this phenomenon to the configurational entropy of mixing that is high in a multiprincipal element alloy relative to their enthalpy of mixing, there by solid solution formation is favored via a decrease in Gibbs free energy of mixing.

$$\Delta G_{mix} = \Delta H_{mix} - T\Delta S_{mix} \quad (1)$$

where, ΔH_{mix} is enthalpy of mixing, ΔS_{mix} is entropy of mixing, and T is temperature. This means in a high entropy alloy, a positive or negative ΔH_{mix} is overcome by $T\Delta S_{mix,}$ driven by a high configurational entropy of mixing, to favor solid solution over phase separation or intermetallic compound formation.

Even though the total mixing entropy has several components such as configurational, magnetic and vibrational; configurational entropy is dominant over other contributions for several material systems [4]. Furthermore, the configurational entropy ($S_{conf.}$) of any alloy can be scaled by increasing number of elements in the alloy which makes this concept appealing for a large number of material systems. Configurational entropy for an ideal solid solution is

$$S\ conf. = -R\sum_{i=1}^{n} xi\ lnxi \quad (2)$$

where R is the gas constant, *xi* is the molar fraction of i^{th} element, and *n* is the total number of constituent elements.

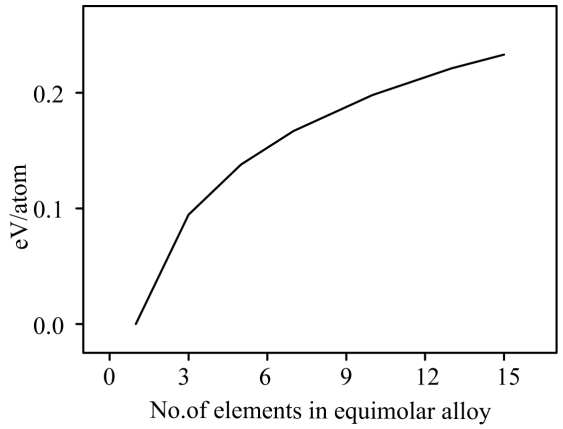

Figure 7.2. Calculated configurational entropy of mixing (at 1000 K), as a function of number of elements in an equimolar alloy.

Figure 7.1 shows estimated value of $S_{conf.}$ as a function of number of elements in an equiatomic alloy at a temperature of 1000 K. The estimation shows that the value of $T\Delta S_{conf.}$ for a quinary alloy is about 0.14 eV/atom which is higher than the enthalpy of mixing of even strong intermetallic compounds such as NiAl, and TiAl [2]. Based on this analysis, it is proposed that if an alloy consists more than five principal elements, an entropy stabilized solid solution might be achieved in spite of a positive enthalpy of mixing. This concept has received a wider acceptance, and resulted an upsurge in the synthesis of several metallic high entropy alloys with fascinating structural and functional properties [5–7].

Recent studies have reported an entropy stabilized solid solution even between non-isostructural oxides of MgO, CoO, NiO, CuO and ZnO, having enthalpy of mixing in the order of 0.1 eV/atom [8]. This indicates that the HEA design concept is also applicable to ceramic compounds such as carbides and nitrides which is explored here.

7.2 Motivation for the multi-principal alloy nitride coating and implementing HEA design:

Before discussing HEA design implementation in nitrides, the need for such a multicomponent nitride alloy must be explored. For a coating to display superior wear resistance in a wide range of applications, it must offer diverse properties simultaneously, i.e. high hot hardness, superior oxidation resistance, and high fracture resistance. The conventional material systems such as TM-Al-N, TM-Si-N achieve any one of these properties at the expense of others, for example high hardness leads to lower fracture resistance and vice versa [9].

To overcome this challenge, it is hypothesized that if a multi-principal element alloy solid solution is formed with a heavily distorted cubic unit cell as shown in Fig. 7.2, the alloy may display superior mechanical properties. For example, in a c-(AlTiZrCrVBSi)N alloy, a high solid solution strengthening can be achieved because of a significant size difference, combined with local fluctuations in shear modulus between different elements in the metallic sublattice [10]. By appropriately tuning the alloy composition, the strengthening mechanisms can be amplified and a high hardness may be achieved both at room temperature and elevated temperature. The alloy is expected to display a superior oxidation resistance by forming a passive oxide diffusion barrier layer consisting of Cr, Al and Si [11]. Simultaneously, the alloy might offer a high toughness to hardness ratio considering the large number of slip systems for the cubic phase. In summary, the cubic solid solution of multi-principal element alloy is likely to display a favorable combination of hot hardness, oxidation resistance and fracture resistance.

However, the proposed alloy has immiscible components. As a consequence, even though the alloy could be formed in a metastable cubic solid solution under non-equilibrium growth conditions, the solid solution may decompose in to non-isostructural equilibrium mixture at elevated temperature. This causes lower hardness and lower fracture resistance.

To overcome this challenge, the HEA design approach is explored in this work to see if the positive ΔH_{mix} can be overcome by high $T\Delta S_{mix\ conf.}$ in the multi-principal element solid solution. This situation leads to an entropy stabilized solid solution at elevated temperature via reduction in ΔG_{mix} as schematically represented in Fig. 7.2.

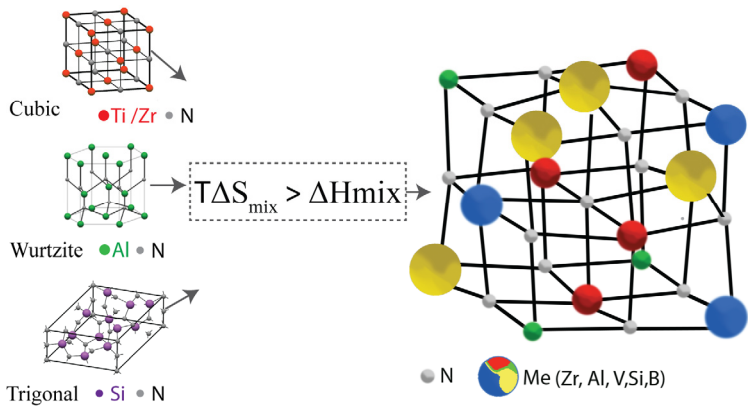

Figure 7.3. Schematic representation of entropy stabilized solid solution formation between hetrostructural metal nitrides.

To test this idea, several (quasi-) quinary TM-Al-N alloys are grown, the composition of these alloys on their metallic sublattice are shown in table 7.1, and nitrogen content is close to stoichiometry. AlN has wurtzite structure and characterized with high interaction energy to c-TMN that results a positive ΔH_{mix} [12].

Ab-initio calculated thermodynamic properties in table 7.1. reveal that the ΔH_{mix} is positive for all the alloys with a value between 0.01 to 0.10 eV/atom. These results also underline that the magnitude of ΔH_{mix} can be tuned as a function of Al concentration. The calculations also reveal that the value of $T\Delta S_{mix\ conf.}$ is higher than ΔH_{mix} at elevated temperature in the multi-principal element alloy. This indicates that the entropy stabilized solid solution may be achieved in spite of a positive ΔH_{mix} in the order of 0.1 eV/atom, at a temperature above 1000 K. This is experimentally investigated by synthesizing the alloys in a cubic solid solution in the coating form, followed by thermal stability investigations. These results are presented in paper V.

	Al, at. %	Ti, at. %	V, at. %	Cr, at. %	Nb, at. %	Zr, at. %	ΔH_{mix}, w.r.t to binaries, eV/atom	Temperature in K, $T\Delta S_{mix\ config.} > \Delta H_{mix,}$
Alloy 1	0.0	25.6	21.4	15.8	21.8	15.5	0.01	< 300
Alloy 2	14.6	16.0	15.9	30.6	0.0	23.0	0.05	400
Alloy 3	17.1	40.2	14.7	3.8	24.2	0.0	0.06	700
Alloy 4	31.1	33.5	12.5	5.5	17.4	0.0	0.10	1000

Table 7. 1 Composition (in metallic sublattice) and thermodynamic properties of multi-principal element nitride alloys

7.3 Synthesis of coatings:

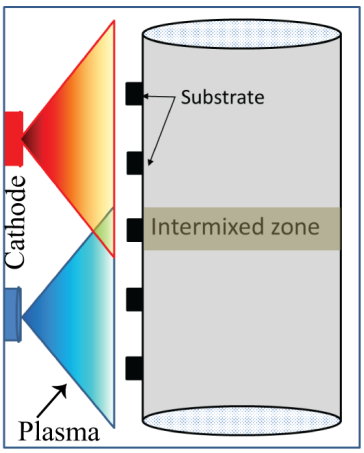

Figure 7.3. Schematic illustration of deposition system.

The multi-principal element alloy coatings are grown in an industrial scale Oerlikon Balzers Metaplas MZR-323 cathodic arc deposition system configured with vertically stacked multiple arc sources, schematically shown in Fig. 7.3.

Several (quasi-) quinary alloy coatings with compositions shown in table 1 are grown by placing the substrates in the plasma intermixed zone (Fig. 7.3) between the composite cathodes of $Ti_{0.3}Al_{0.6}Cr_{0.1}$, $Ti_{0.4}Nb_{0.4}V_{0.2}$ and

$Zr_{0.4}Cr_{0.4}V_{0.2}$. The coating composition is varied by displacing the substrate position away from the intermixed zone on the substrate holder.

Figure 7.4 shows XRD scans and TEM micrograph of the multi-principal element alloys revealing a single cubic crystalline phase, indicating solid solution formation in spite of having 5 different elements on their metallic sublattice.

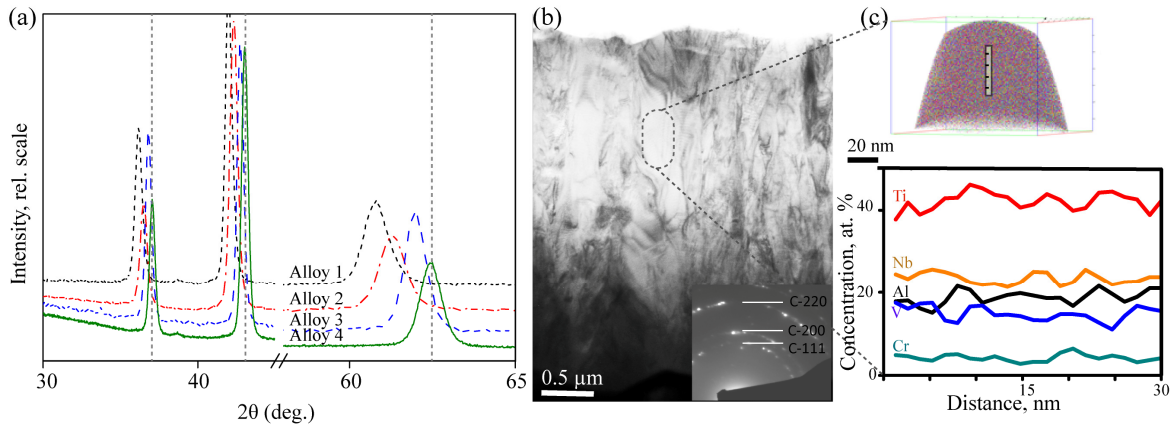

Figure 7.4. (a) θ- 2θ XRD scans of multi-principal alloy coatings, (b) BF-TEM with in set SAED pattern of alloy 3 coating, (c) APT reconstruction, and 1D concentration profile analysis of alloy 3 coating. The dotted line in Fig. a is for visual reference to indicate the diffraction peak positions of multicomponent cubic phase.

In addition, atomic scale investigations are performed in the alloy using atom probe tomography (APT). Figure 7.4 c shows APT reconstruction for alloy 3 revealing a randomly mixed solid solution and no cluster formation within the measured volume of 80 x 60 x 60 nm^3. This is achieved by fine tuning growth conditions such that the compositional fluctuations at the growth front are suppressed. The growth parameters used here are: an arc current of 150 A, and a burning voltage of 30 V, in a pure N_2 atmosphere, at an operating pressure of 6 Pa, a pulsed substrate bias of -50 V, 50 kHz, and a substrate temperature about 350 °C (heaters switched off). Furthermore, during the coating growth, the substrate holder is kept in a static condition to prevent the rotation- induced artificial layering that causes compositional inhomogeneity [13].

References

[1] J.W. Gibbs, The scientific papers of J. Willard Gibbs. Vol. 1, Dover, New York, 1961.

[2] B.J. Yeh, S. Chen, S. Lin, J. Gan, T. Chin, T. Shun, C.H. Tsau, S.Y. Change, Nanostructured High-Entropy Alloys with Multiple Principal Elements : Novel Alloy Design Concepts and Outcomes, (2004) 299–303.

[3] B. Cantor, I.T.H. Chang, P. Knight, A.J.B. Vincent, Microstructural development in

equiatomic multicomponent alloys, Mater. Sci. Eng. A. 375-377 (2004) 213–218.

[4] B.S. Murty, Jien-Wei Yeh, S. Ranganathan, High-Entropy Alloys, 1 st edition, Butterworth-Heinemann (2014).

[5] Y. Zhang, T. Ting, Z. Tang, M.C. Gao, K.A. Dahmen, P.K. Liaw, Z.P. Lu, Microstructures and properties of high-entropy alloys, Progress in Materials Science 61 (2014) 1–93.

[6] Y. Zhang, T. Zuo, Y. Cheng, P.K. Liaw, High-entropy alloys with high saturation magnetization, electrical resistivity, and malleability, Sci. Rep. 3 (2013) 1455.

[7] X.W. Qiu, Y.P. Zhang, L. He, C.G. Liu, Microstructure and corrosion resistance of AlCrFeCuCo high entropy alloy, J. Alloys Compd. 549 (2013) 195–199.

[8] C.M. Rost, E. Sachet, T. Borman, A. Moballegh, E.C. Dickey, D. Hou, J.L. Jones, S. Curtarolo, J.P. Maria, Entropy-stabilized oxides, Nat. Commun. 6 (2015) 8485.

[9] S. Zhang, D. Sun, Y. Fu, Y.T. Pei, J.T.M. De Hosson, Ni-toughened nc-TiN/a-SiNx nanocomposite thin films, Surf. Coatings Technol. 200 (2005) 1530–1534.

[10] R.L. Boxman, V.N. Zhitomirsky, I. Grimberg, L. Rapoport, S. Goldsmith, B.Z. Weiss, Structure and hardness of vacuum arc deposited multi-component nitride coatings of Ti, Zr and Nb, Surf. Coatings Technol. 125 (2000) 257–262.

[11] P. V. Kiryukhantsev-Korneev, D. V. Shtansky, M.I. Petrzhik, E.A. Levashov, B.N. Mavrin, Thermal stability and oxidation resistance of Ti-B-N, Ti-Cr-B-N, Ti-Si-B-N and Ti-Al-Si-B-N films, Surf. Coatings Technol. 201 (2007) 6143–6147.

[12] B. Alling, T. Marten, I.A. Abrikosov, A. Karimi, Comparison of thermodynamic properties of cubic Cr1-x Alx N and Ti1-x Alx N from first-principles calculations, J. Appl. Phys. 102 (2007)044314.

[13] A.O. Eriksson, J.Q. Zhu, N. Ghafoor, M.P. Johansson, J. Sjölen, J. Jensen, M.Odén, L. Hultman, J. Rosén, Layer formation by resputtering in Ti-Si-C hard coatings during large scale cathodic arc deposition, Surf. Coatings Technol. 205 (2011) 3923–3930.

8. Summary and contribution to the field

A lower fracture resistance of hard coatings, and limited thermal stability of TM-Al-N coatings has been a long standing challenges in the field. To overcome these challenges, the coating material is manipulated over multiple length scales, i.e microstructure variation in paper 1, and 2, crystal and interface structure variation in paper III and IV, and finally the atomic scale effects are explored in paper V. This chapter summarizes my interpretation of the results from the papers and explains how these findings show technical solutions to the standing challenges.

8.1 Paper I

Structure, deformation and fracture of arc evaporated Zr–Si–N hard film

Me-Si-N material systems have gained significant attention ever since Vepreck et al., have reported hardness value of above 40 GPa for Ti-Si-N nanocomposite coatings. However, in spite of the similar crystal structure and comparable electronic structure between ZrN and TiN, the hardness enhancement is absent for the Zr-Si-N nanocomposite coatings, which is an open question. Furthermore, it is not known how the fracture resistance varies as a function of microstructural variation.

In this paper, Zr-Si-N coatings are grown over WC-Co substrate using an industrial scale reactive arc deposition technique. The Si content of the coatings varied between 0.2 and 6.3 at. %, Si forms a substitutional solid solution with ZrN up to 1.8 at. % in a columnar structure. Further Si addition causes precipitation of amorphous-SiN_X phase on the growth front followed by a breakdown of the columnar structure. This evolves a nanocomposite structure at 6.3 at. % Si. The resulting microstructure of the coatings lead to a systematic variation in hardness, where the columnar structured coating with 1.8 at. % Si display a hardness value of 37±2GPa, and the nanocomposite coating shows a lower hardness of 26±1GPa. To unveil the structure-hardness relationship, the deformation mechanism of the coating is visualized by topographical examination of the indent surface followed by TEM examination of a lamellae extracted beneath the indent where the artificial layers are used as markers to follow the indentation-induced displacement events. The investigation reveals a dislocation-based homogeneous plastic deformation for the columnar

microstructure, while grain boundary sliding is the active mechanism mediating heterogeneous plastic deformation in the nanocomposite microstructure. The observed grain boundary sliding mechanism explains why the Zr-Si-N coating with nanocomposite structure is softer than the columnar structured coating. However, the lower hardness did not translate as higher fracture resistance for the nanocomposite coatings.

Indentation-induced fracture studies reveal that the fine columnar structure display higher fracture resistance compared to the nanocomposite structure. The observed crack pattern suggests a crack deflection and branching to be the active toughening mechanism in the columnar structure. In contrast, a grain size of 5 nm in the nanocomposite structure is much lower than the size of fracture process zone (~30 nm), and hence could not offer any local hindrances for the crack growth.

In summary, the nanocomposite structure of Zr-Si-N offers lower hardness due to the grain boundary mediated heterogeneous deformation mechanisms, and the absence of crack deflection mechanism causes lower fracture resistance compared to the columnar ZrN coatings. The later observation suggests that the fracture resistance of the coating can be enhanced by optimizing the microstructure of the coating to maximize the crack deflection.

6.2 Paper II

Influence of microstructure and mechanical properties on the tribological behavior of reactive arc deposited Zr-Si-N coatings at room and high temperature

A deeper understanding of the structure-hardness-fracture correlation of Zr-Si-N coatings in paper I has motivated me to investigate the intricate influence of microstructure and mechanical property variation on the tribology behavior of the coatings under a sliding contact, both at room temperature and high temperature (500 °C). By performing electron microscopy investigations, on the wear track, and FIB-cut cross-sections, followed by a lamellae extraction under the wear track, the study provide deeper understanding about the mechanisms governing the tribological response and their relationship to the microstructure and mechanical properties of the coatings.

The results show that at room temperature, tribo-oxidation is the dominant wear mechanism, where the nanocomposite coatings display the lowest wear rate of 0.64 x 10^{-5} mm^3/Nm, by forming an oxide diffusion barrier layer consisting of Zr, W, and Si. A transition in the dominant wear mechanism from tribo-oxidation to micro-ploughing is observed upon increasing the test temperature and contact stress. Here, all coatings exhibit significantly higher coefficient of friction of 1.4 and the hardest coatings with columnar structure displays the lowest wear rate of 10.5 x 10^{-5} mm^3/Nm. In a microscopic wear test, under the influence of contact-induced dominant elastic stress field, the coatings display wedge formation and material pileup due to accumulative dislocation-induced plastic deformation similar to fatigue process. In these tests, the nanocomposite coatings display the lowest wear rate of 0.56 x 10^{-10} mm^3/Nm, by constraining the dislocation motion.

In summary, this study underlines that the microstructure - mechanical property influence of the tribological response of the coatings is highly dependent on the thermal and mechanical conditions prevailing in a contact. The soft and brittle nanocomposite coatings have displayed superior wear resistance when tribo-oxidation is dominant. In contrast, the hard and tough columnar coatings display superior performance when surface deformation is the dominant wear mechanism.

6.3 Paper III

Tuning hardness and fracture resistance of ZrN/$Zr_{0.63}Al_{0.37}N$ nanoscale multilayers by stress-induced transformation toughening

TMN hard coatings suffer with lower fracture resistance, and the typical K_{IC} value has been reported to be around 2- 4 MPa√m. For the bulk form ceramic materials it is known that the fracture resistance could be enhanced by extrinsic toughening mechanisms, such as stress induced transformation toughening. However, it is not known how to adapt these toughening mechanisms to nitrides in the coating form which is explored in this paper.

$Zr_{0.63}Al_{0.37}N$ coatings are grown at a higher temperature of 700 °C to cause *insitu* segregation in to ZrN and AlN rich domains. By adapting a multilayer structure, and varying the ZrAlN layer thickness between 2 nm and 30 nm, a layer thickness dependent structural transformation is achieved for AlN domains, i.e. epitaxially

stabilized metastable cubic structure at a layer thickness of 2 nm, and stable wurtzite structure at a layer thickness of 30 nm. The structural changes of AlN domains lead to a systematic variation in mechanical properties.

Indentation induced fracture studies show a significantly high fracture resistance for the multilayers of 2 nm $Zr_{0.63}Al_{0.37}N$ consisting metastable cubic AlN phase. The critical force to cause a first surface crack is two times higher for the multilayer consisting metastable c-AlN, compared to the multilayer consisting of stable w-AlN phase. By extracting a thin lamella under the indent followed by TEM examination, it is discovered that the high fracture resistance is a result of transformation of AlN from a metastable cubic phase to thermodynamically stable wurtzite phase under indentation-induced stress field. This phase transformation is associated with a molar volume expansion of about 20 %, forming local compressive stress zones that postpone nucleation and propagation of cracks, and results in high fracture resistance.

In summary, this work provides the first experimental data point for the stress-induced transformation toughening in the TM-Al-N hard coating. This finding opens new avenues to tailor the coating composition and structure to enhance the toughness without compromising the hardness of the coating.

Paper IV.

Growth and thermal stability of TiN/ZrAlN: Effect of internal interfaces

Metastable c-TM-Al-N hard coatings such as c-Ti-Al-N, and c-Cr-Al-N are the current workhorse materials for several cutting applications, thanks to their high oxidation resistance in combination with a favorable hardness. However, at a temperature above 900 °C, the coatings show a significant hardness drop when the alloy decomposes to it's equilibrium mixture of c-TMN and w-AlN. This confines the coating application temperature, and remains as a long standing challenge in the field.

In this paper, a technical solution to the above mentioned challenge has been explored by modifying the interface structure of the material. It is shown that the w-AlN is not detrimental to hardness, provided the interface structure is modified, from the incoherent to (semi-)coherent type. Furthermore, thermal stability of the

modified interface structure is investigated by combining experimental results and first principal calculations.

The multilayers of TiN/ $Zr_{0.43}Al_{0.57}N$, are grown using DC magnetron sputtering on MgO (001) surface. The ZrAlN layer thickness and growth temperature are varied to modify both the crystal structure and interface structure of segregated AlN domains. A metastable cubic phase is formed up to a layer thickness of 5 nm, and at the higher layer thickness, AlN assume its thermodynamically stable wurtzite phase but with incoherent interfaces. However, a higher growth temperature of 900 °C facilitates pronounced segregation of w-AlN and c-ZrN domains, and the interface energy minimization leads to evolution of a self-aligned inplane modulation in composition and structure with (semi-)coherent interfaces between *w*-AlN and cubic phases (TiN and ZrN). More interestingly, the modulated structure displays a high and stable hardness of 34 GPa even after an experimentally limited annealing temperatures of 1150 °C. The underpinning structural effects are investigated by lattice resolved transmission electron microscopy combined with atom probe tomography revealing that the high hardness after the elevated temperature is a consequence of thermally stable (semi-)coherent interfaces between w-AlN and c-TiN, c-ZrN. Two types of interface coherency relations have been found, where *c*-$ZrN_{(110)[001]} \parallel w\text{-}AlN_{(10\text{-}10)[001]}$ interfaces are promoted by a MgO (001) template effect and the *c*-$TiN_{(111)[10\text{-}1]} \parallel w\text{-}AlN_{(0001)[11\text{-}20]}$ interfaces are promoted by their higher thermodynamic stability. These experimental observations are further confirmed by first principle calculations indicating that the non-isostructural (semi-)coherent interfaces between c-TiN, ZrN and w-AlN has higher thermodynamic stability compared to isostructural coherent interfaces between c-AlN and c-TiN, c-ZrN.

These findings in this paper lead to propose a new structural archetype of c-TMN/w-AlN, with low energy semicoherent interface structure as an alternative material design route to the currently used metastable c-TM-Al-N alloy, to achieve a high thermal stability and high hardness at elevated temperature.

Paper V

Exploring high entropy alloy design in (AlTiVNbCr)N alloy

A cubic solid solution consisting of TMN, AlN, SiNx, and BN offer significantly higher hardness and oxidation resistance. However, a high interaction energy between these components causes very limited solubility between them under thermodynamically equilibrium conditions.

To overcome this inherent material limitation, in this paper, high entropy alloy (HEA) design principles are explored to alter the thermodynamics of the immiscible TM-Al-N material system. HEA design is based on the idea that a high configurational entropy in a multi-principal-element alloy might favor an entropy stabilized solid solution via a decrease in ΔG_{mix} at elevated temperature, by overcoming positive ΔH_{mix} by the other thermodynamic term $T\Delta S_{mix}$ in the alloy.

Multi-prinicipal-element alloy of (AlTiVNbCr)N is formed in cubic solid solutions by reactive arc evaporation process. The (pseudo-) quinary cubic solid solution is characterized with high configurational entropy and predicted to have higher thermodynamic stability relative to their binary nitrides at a temperature above 1000 K. However, elevated temperature annealing show that the quinary solid solution decomposes to w-AlN and c-(TiVNbCr)N, which is investigated by combining first principle calculations and atom probe tomography. The investigation reveals that the thermally stable solid solution is achieved only between the elements with low enthalpy of mixing in the order of 0.01 eV/atom. Whereas the alloys with high enthalpy of mixing in the order of 0.06 eV/atom, evolves decomposition pathway such that the enthalpy of mixing is reduced without causing a significant loss in configurational entropy of mixing, so that the free energy is minimized. This study underlines that the multi-principal-element alloy solid solution with positive enthalpy of mixing, based on HEA design principles, is only a metastable state in TM-Al-N material system.

In summary, the current work provides technological solutions to the two outstanding issues in the field. A significant enhancement in fracture resistance of the coating can be achieved with an appropriate material choice and microstructural

design by invoking crack deflection and stress induced transformation toughening mechanism. A remarkable thermal stability enhancement of the TM-Al-N coating is achieved by a new structural archetype consisting *c*-TMN and thermodynamically stable *w*-AlN with a low energy (semi-)coherent interface structure.

9. Future work

This chapter presents the potential future work based on the observations and conclusions of the current work.

9.1 Fracture resistance of hard coatings

In this work I show that the fracture resistance of thin coatings could be enhanced by extrinsic toughening mechanisms such as crack deflection and stress induced transformation toughening using a semi-quantitative method. Someone must quantify the fracture resistance enhancement in terms of K_{IC} values using the pillar compression technique, and further open questions for the individual toughening mechanisms are presented here.

9.1a Stress induced transformation toughening (SITT):

The current work provides the first experimental data point for the SITT in nitride coatings, by transforming the AlN domains from a metastable cubic phase to thermodynamically stable wurtzite phase in a chemically segregated ZrAlN alloy under an indentation-induced stress field. However, the details about the transformation pathway, and the stress state activating this transformation is not known completely. Future studies are also required to examine if similar stress-induced transformation of AlN can be achieved in other TM-Al-N alloys such as, Ti-Al-N, Cr-Al-N, and Nb-Al-N alloy. By tuning the alloy composition, it might be possible to reduce the energy barrier for the transformation, thereby the magnitude of the stress required for the transformation might also be reduced.

Finally, someone needs to explore if SITT can be invoked in a real time application under the complex stress field, thereby the coatings can be engineered to offer superior toughness without a compromise in hardness. Nevertheless, it must be noted that the SITT can only be activated for medium and low temperature applications where AlN could be retained in a metastable cubic phase.

9.1b Crack deflection toughening mechanism

For the Zr-Si-N coating it has been shown that a high fracture resistance can be achieved in spite of its higher hardness by invoking crack deflection in the columnar structure, but not in the nanocomposite structure. Further systematic studies are required to find the optimal morphology and grain size that amplify the crack deflection mechanism and enhances the fracture toughness. This is also perhaps a material dependent issue, as the crack deflection tendency at the interface is influenced by the elastic and plastic properties of the material.

9.2 Thermal stability of TM-Al-N coatings

The state of the art metastable c-TM-Al-N alloys, such as c-Ti-Al-N, c-Cr-Al-N display poor thermal stability above 900 °C. This has been attributed to the precipitation of w-AlN that leads to a lower hardness, and structural instability. To solve this issue two different material design routes are explored in this work.

9.2a Interface structure modification

Based on the experimental and calculation results in the TiN/ZrAlN multilayer (paper IV), it has been shown that a high thermal stability (>1150 °C), and a high hardness at elevated temperature can be achieved in the TM-Al-N alloys with a new structural archetype of c-TMN/w-AlN, and having a low energy coherent interfaces between them. Based on these results, and the analysis in chapter VI it is hypothesized that the NbN(111)/AlN(0001) may offer the highest thermal stability with a stable and high hardness during the elevated temperature annealing. This must be verified experimentally.

Finally, the grand challenge is to grow such interface engineered structures on a polycrystalline surface, in a reliable and reproducible way to upscale the proposed structural archetype. Recently, similar structure has been reported in a CVD process as mentioned in chapter VI.

9.2b High entropy alloy design

It is presumed that the high configurational entropy in a multi-principal-element alloy of c- (TiNbVCrAl)N can overcome the positive ΔH_{mix}, there by an entropy stabilized solid solution may be achieved via lowing ΔG_{mix}. This means, the alloy

decomposition is suppressed forever in spite of positive ΔH_{mix}. However, the experimental results show that the (pseudo-) quinary cubic solid solution is only metastable state for the TM-Al-N material system.

However, this observation should not be generalized to other immiscible materials. At least theoretical calculations must be considered, if an entropy stabilized solid solutions can be achieved in other immiscible material systems such as TM-Si-N, TM-B-N etc.,

Paper I

Structure, deformation and fracture of arc evaporated Zr–Si–N hard film

K. Yalamanchili, R. Forsén, E. Jiménez-Piqué, M.P. Johansson Jöesaar, J.J. Roa, N. Ghafoor, M. Odén

Surface & Coatings Technology 258 (2014) 1100–1107

ATTENTION ¡
Pages 78 to 84 of the thesis, containing the text mentioned above, should be consulted on the web pages of the editor's web
http://www.sciencedirect.com/science/article/pii/S0257897214005969

Paper II

Influence of microstructure and mechanical properties on the tribological behavior of reactive arc deposited Zr-Si-N coatings at room and high temperature

K. Yalamanchili, E. Jiménez-Piqué, L. Pelcastre, KD Bakoglidis, J.J. Roa, M.P. Johansson Jöesaar, B. Prakash, N. Ghafoor, M. Odén

Surface & Coatings Technology 304 (2016) 393–400

Influence of microstructure and mechanical properties on the tribological behavior of reactive arc deposited Zr-Si-N coatings at room and high temperature

K. Yalamanchili[1,2], E. Jiménez-Piqué[2], L. Pelcastre[3], KD Bakoglidis[1], J.J. Roa[2], M. P. Johansson Jöesaar[1,4], B. Prakash[3], N. Ghafoor[1] and M. Odén[1]

1. Department of Physics, Chemistry and Biology (IFM), Linköping University, SE 58183, Linköping, Sweden

2. Departamento de Ciencia de los Materiales e Ingeniería Metalúrgica, Center for Research in Nanoengineering, CRnE-UPC Avda. Diagonal 647, 08028 Barcelona, Spain

3. Division of machine elements, Luleå University of Technology, Luleå SE-97187, Sweden

4. Seco Tools AB, SE 737 82 Fagersta, Sweden

Abstract

Varying the Si-content in Zr-Si-N coatings from 0.2 to 6.3 at% causes microstructural changes from columnar to nanocomposite structure and a hardness drop from 37 to 26 GPa. The softer nanocomposite also displays lower fracture resistance. The tribological response of these coatings is investigated under different contact conditions, both at room and elevated temperatures. At room temperature tribooxidation is found to be the dominant wear mechanism, where the nanocomposite coatings display the lowest wear rate of 0.64 x 10^{-5} mm^3/Nm, by forming an oxide diffusion barrier layer consisting of Zr, W, and Si. A transition in the dominant wear mechanism from tribooxidation to microploughing is observed upon increasing the test temperature and contact stress. Here, all coatings exhibit significantly higher coefficient of friction of 1.4 and the hardest coatings with columnar structure displays the lowest wear rate of 10.5 x 10^{-5} mm^3/Nm. In a microscopic wear test under the influence of contact-induced dominant elastic stress field, the coatings display wedge formation and pileup due to accumulation of the dislocation-induced plastic deformation. In these tests, the nanocomposite coatings display the lowest wear rate of 0.56 x 10^{-10} mm^3/Nm, by constraining the dislocation motion.

1. Introduction

ZrN based coatings are interesting candidate materials for the wear resistant applications with several unique features, such as excellent wear protection of metal cutting tool inserts [1], high thermal stability [2], and fracture resistance enhancement by stress induced-transformation toughening [3]. However, the primary limitation to ZrN based coatings is poor oxidation resistance. This behavior shows similarities with the TiN system. In this case it has been shown that alloying with Si effectively improve the oxidation resistance and mechanical properties of Ti-

Si-N coatings [4–7]. Motivated by these results, Zr-Si-N materials have been explored in several studies showing that coatings with a Si-content of 6 - 7 at% display an improved oxidation resistance and a transition in microstructure from a columnar to a nanocomposite structure correlated to a variation in coating hardness [8–11]. Previous studies of Zr-Si-N, however, have mainly focused on investigating the microstructure and mechanical property variation [9,12]. Its tribological response is less studied which motivates further studies in this area. In addition, there is a growing interest in nitride coatings for MEMS applications [13], where the microscale tribological response of the coatings is important, which is relatively unexplored.

Although wear properties of coating commonly are dependent on their mechanical properties [14,15], its specific wear mechanisms are material dependent. Previous tribological study of Zr-Si-N coating has related the wear rate to the Si-content [16]. In fact, nanocomposite Zr-Si-N coating with 7.6 at.% Si revealed a higher wear resistance in spite of its lower hardness [16]. However, no details of the corresponding wear mechanisms were reported.

In this work, the tribological response of Zr-Si-N coatings were investigated as a function of microstructure and mechanical property variation under different contact conditions, such as the contact force, temperature and test configuration, both at room and elevated temperature for macro- and microscale sliding contacts. Furthermore, we establish how the structure-property variation influences the tribological response by TEM examination of samples extracted beneath the wear tracks. This fundamental knowledge is essential for the development of future wear resistant coatings.

2. Experimental procedure

2.1 Deposition of coatings

A series of seven different Zr-Si-N coatings with Si-content varying between 0.2 and 6.3 at% were grown on mirror finished WC-10 wt. % Co (ISO geometry SNUN 120408) 12 × 12 mm^2 substrates in a Sulzer/Metaplas MZR-323 cathodic arc deposition system. The substrates were ground, mirror-shine polished, and pre-cleaned in an ultrasonic bath of an alcohol solution. Before growth, the deposition

system was evacuated to a pressure of less than 2.0×10^{-3} Pa, after which the substrates were plasma-etch cleaned with 500 eV Ar^+ ions for 15 min. Pre-alloyed cathodes with the compositions Zr, $Zr_{96}Si_4$, and $Zr_{86}Si_{14}$ were positioned at the top, center, and bottom arc sources of the chamber, respectively. The films were grown using an arc current of 100 A resulting in a burning voltage of 30 V in a pure N_2 atmosphere at an operating pressure of 4 Pa, a substrate bias of–30 V, and a substrate temperature of 400 °C. The coatings were grown up to a nominal thickness of 4 ± 0.5 μm, with a surface roughness (R_a) measured between 0.2 and 0.3 μm.

2.2 Wear tests

Room temperature (RT) reciprocating sliding wear tests were performed using a tribometer TRM 1000 from Wazau GmbH with ball-on-disc configuration, where the reciprocating ball slides against the lower stationary specimen. During a total sliding distance of 100 m a contact force of 5 N, stroke length of 4 mm and an average velocity of 0.06 m/s were maintained.

High temperature (HT) tribology tests were performed using a similar ball-on-disc configuration in a SRV Optimal wear test machine equipped with sample heating stage, which was maintained at 500 °C during the test. During the sliding distance of 3.6 m, a contact force of 10 N, stroke length of 1 mm and an average velocity of 0.02 m/s were used. Both these machines are equipped with computerized control and data acquisition system enabling control over stroke length, frequency, and contact force. For both RT and HT sliding wear tests, WC-8 wt. % Co balls of 10 mm diameter (Fritsch) with a hardness of 1600 HV_{10} were used as the counter material.

Before the tests, the ball and the coated specimens were ultrasonically cleaned with acetone, ethanol, and blow-dried with N_2. The wear tests were conducted under dry sliding conditions in air with relative humidity of 60%. After the test, the depth and the volume of the wear track was measured with a Veeco Dektak 150 profilometer and observed by scanning electron microscopy.

Microwear tests were performed at ambient temperature of 25 °C, on a polished coating surface using a diamond conical indenter with a nominal tip radius of 5 μm in a Triboindenter® TI-950 from Hysitron in a multipass nanoscratch test configuration, equipped with *in situ* scanning probe imaging. During the sliding distance of 10 mm, a normal force of 10 mN is applied with a stroke length of 10

μm at a sliding velocity of 0.002 μm/s. Wear volume is calculated from the 3D cross-sectional line profile of scanning probe image of the wear track.

2.3 Microstructural and mechanical property characterization

Scanning Electron Microscopy (SEM) images of the coating and wear tracks were recorded with a LEO 1550 FEG scanning electron microscope operated at 5 kV and a working distance of 10 mm. Cross-sectional transmission electron microscopy (TEM) foils were prepared under the wear track by the lift out technique using a focused ion beam (FIB) Zeiss Neon 40 dual-beam workstation [17]. TEM and scanning (S) TEM were performed using a FEI Tecnai G2 TF 20 UT FEG microscope operated at 200 kV, equipped with an energy- dispersive X-ray analysis spectrometer (EDX). For STEM analysis, a high-angle annular dark field (HAADF) detector and a camera length of 160 mm was used.

Hardness (*H*) and elastic modulus (*E*) of the tribolayer of the coatings were evaluated in a MTS nanoindenter XP equipped with a Berkovich diamond tip and using the Oliver and Pharr method [18]. The continuous stiffness measurement (*CSM*) module was activated to log the contact stiffness (S) during the entire loading portion of load (*P*) - depth (*h*) curve. The tip area function was calibrated using a fused silica reference, and the measurements were corrected for the load frame compliance and thermal drift.

2.4 Oxidation test

Oxidation tests were done on 0.2, 1.8 and 6.3 at% Si coating materials removed from the substrates. In this case, the coatings were grown on thin Fe foils using identical deposition conditions as for the WC-Co substrates. The Fe foil was removed through mechanical polishing and subsequent dissolution in a diluted H_2SO_4 acid at a temperature of 90 °C. The resulting powder of the coating material was then rinsed in deionized water and dried in a furnace at 150 °C overnight. Oxidation tests of the powder were conducted by heating at a rate of 5 °C/min up to 1000 °C in air at atmospheric pressure while measuring the sample mass in a Netzsch STA 410 instrument. In addition, coated WC-Co substrates were also heat treated at 800 °C in air for 1 hr.

3. Results

3.1 Microstructure and mechanical property variation as a function of Si

In addition to the wear behavior of Si-alloyed ZrN coatings reported here, a detailed study of the microstructure and mechanical properties of these coatings have been reported elsewhere [17]. As a background, we summarize the most relevant results. Si forms a substitutional solid solution, on the metallic sublattice of ZrN, in Zr-Si-N coatings up to 1.8 at.% of Si. Additional amount of Si causes precipitation of an amorphous-SiN_X phase on the growth front followed by a breakdown of the columnar structure. At ~ 6.3 at.% of Si the coatings have an equiaxed nanocomposite structure.

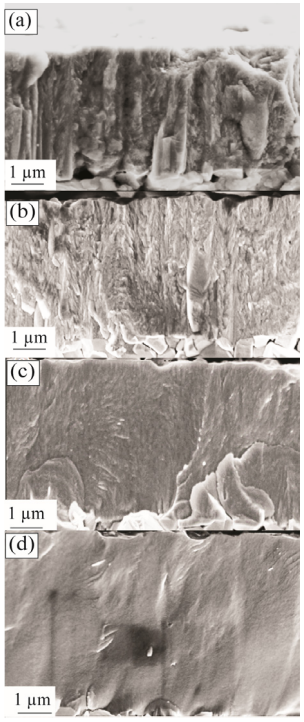

Figure 1. SEM micrographs of fractured cross-sections of Zr-Si-N coatings, (a) 0.2 at% Si, (b) 1.8 at% Si, (c) 4.3 at% Si, and (d) 6.3 at% Si.

Si [at%]	Structure	H (GPa)	E (GPa)	Fracture resistance,
0.2	columnar	33±2	425±17	high
0.6		35±2	450±28	
1.3		36±2	430±7	
1.8		37±2	425±17	medium
2	mixture	34±1	435±15	
4.3		30±1	395±11	
6.3	nanocomposite	26±1	350±7	low

Table 1. Hardness and elastic modulus of as-deposited Zr-Si-N coatings with varying Si content.

Figure 1 shows SEM micrographs of fractured cross-sections to visualize these microstructural changes. The hardness and elastic modulus are listed in Table 1 (from [17]). The hardness of the columnar structured coatings is found to increase with Si up to 1.8 at% (~ 37 GPa) attributed to solid solution hardening. Strain localization caused by the grain boundary mediated deformation causes a considerably lower hardness (~ 26 GPa) of the nanocomposite structure (6.3 at.% Si). The fracture

resistance of these coatings was found to be highest for the columnar structure with 0.2 at.% Si and lowest for the nanocomposite coating with 6.3 at.% Si.

3.2 Room temperature wear tests

The wear rates of the coatings, recorded at RT and a contact force of 5 N (Hertzian contact stress of 1200 MPa), are shown in Fig. 2.

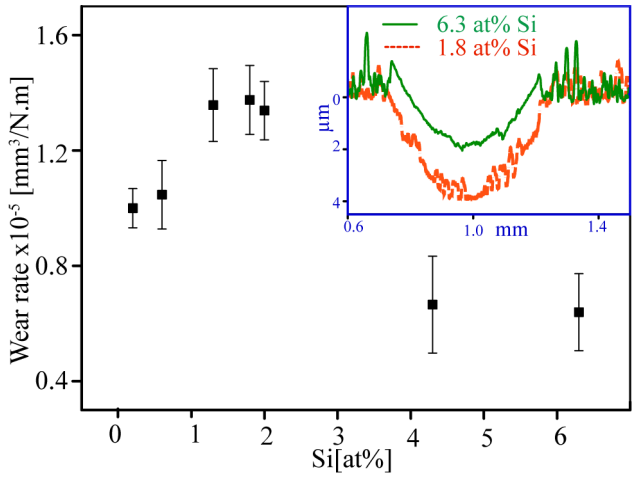

Figure 2. Wear rate of Zr-Si-N coatings as a function of Si content. Inset image show surface profile of the wear tracks.

The wear rate is calculated by dividing the wear volume [mm^3] by the normal force [N] and the sliding distance [m]. The wear rate increases up to a Si-content up to 1.8 at%, with a maximum value of 1.4x10^{-5} mm^3/Nm. Further Si additions reduces the wear rate to the lowest value of 0.64x10^{-5} mm^3/Nm for coatings with 6.3 at% Si, i.e. the soft and brittle nanocomposite coatings exhibit a wear resistance enhancement of 120 % compared to the hard columnar structured coating. The coefficient of friction (COF) is measured to be between 0.5 and 0.6 for all the coatings. The inset image in Fig. 2 shows the surface profiles of the wear track of 1.8 and 6.3 at% Si containing coatings. The 1.8 at% Si coating displays a deep and rough profile while the wear tracks of the 6.3 at% Si coating show shallow and smooth profiles.

Figure 3 shows SEM micrographs of plan-view and FIB prepared cross-sections of the wear tracks. They reveal a bilayer in the wear track with contrast variations for the columnar structured coatings containing 0.2 and 1.8 at% Si (Fig. 3 a, b and d, e). Cross-sectional micrographs reveal formation of a discontinuous thick tribolayer for the columnar structured coatings (Fig. 3c and f), which suggests delamination during the test. In contrast, the nanocomposite coating (6.3 at% Si) displays thin tribolayer with fine scoring marks (Fig. 3g and h). The thickness of the residual coatings is measured to be 2.0 and 0.6 µm, whereas the tribolayer are 0.9 and 0.7 µm for 0.2 at% Si and 1.8 at% Si coatings, respectively. The lower thickness values of both the coating and the tribolayer, indicate that the 1.8 at% Si coatings are more prone to delamination, compared to the 0.2 at% Si coating.

This observation can also explain the appearance of more discontinuous wear track of 1.8 at% Si more clearly observed in the overview micrograph. The coatings with 6.3 at% Si display thin tribolayers with fine scoring marks in the sliding direction. These were attributed to micro-abrading action of the wear debris.

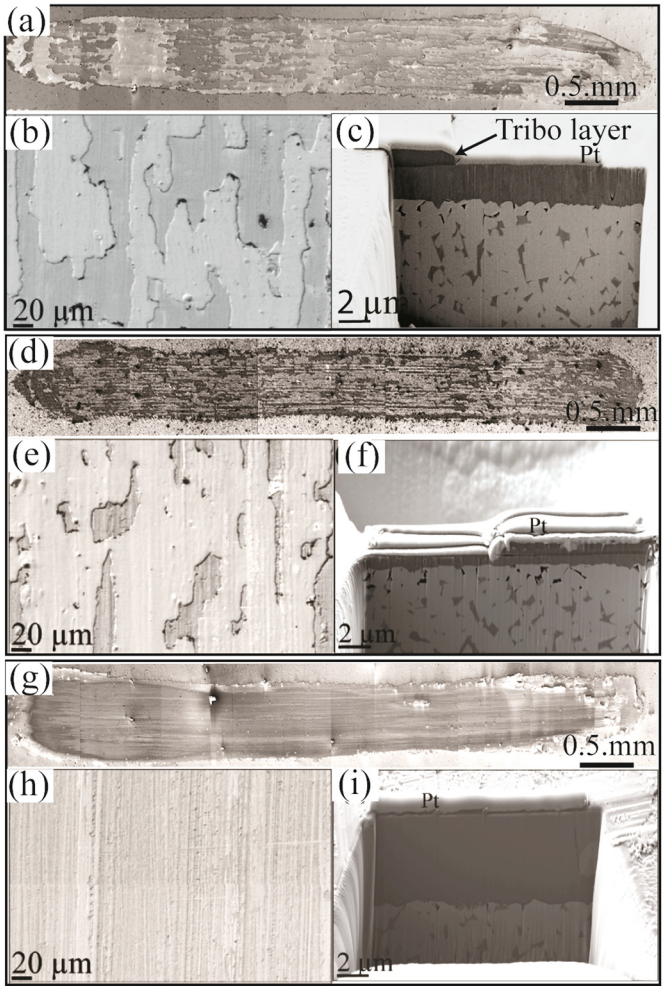

Figure 3. Overview and magnified SEM images of the wear tracks on the coatings in RT test, and corresponding FIB prepared cross-sections beneath the wear track, (a-c) 0.2 at% Si, (d-f) 1.8 at% Si, and (g-i) 6.3 at% Si.

Figs. 4a and d shows bright field BF-TEM micrographs of lamellas extracted under the wear track formed in the columnar coating containing 1.8 at.% Si and the nanocomposite coating containing 6.3 at.% Si, respectively.

No signs of sliding induced plastic deformation nor cracks are observed in the coatings and, the virgin microstructures are retained for both coating structures. The coating with 1.8 at% Si shows a partly delaminated thick tribolayer on top of the columnar structure with subsurface voids and cracks. The voids are likely generated by the accumulation of lattice defects induced during the sliding contact.

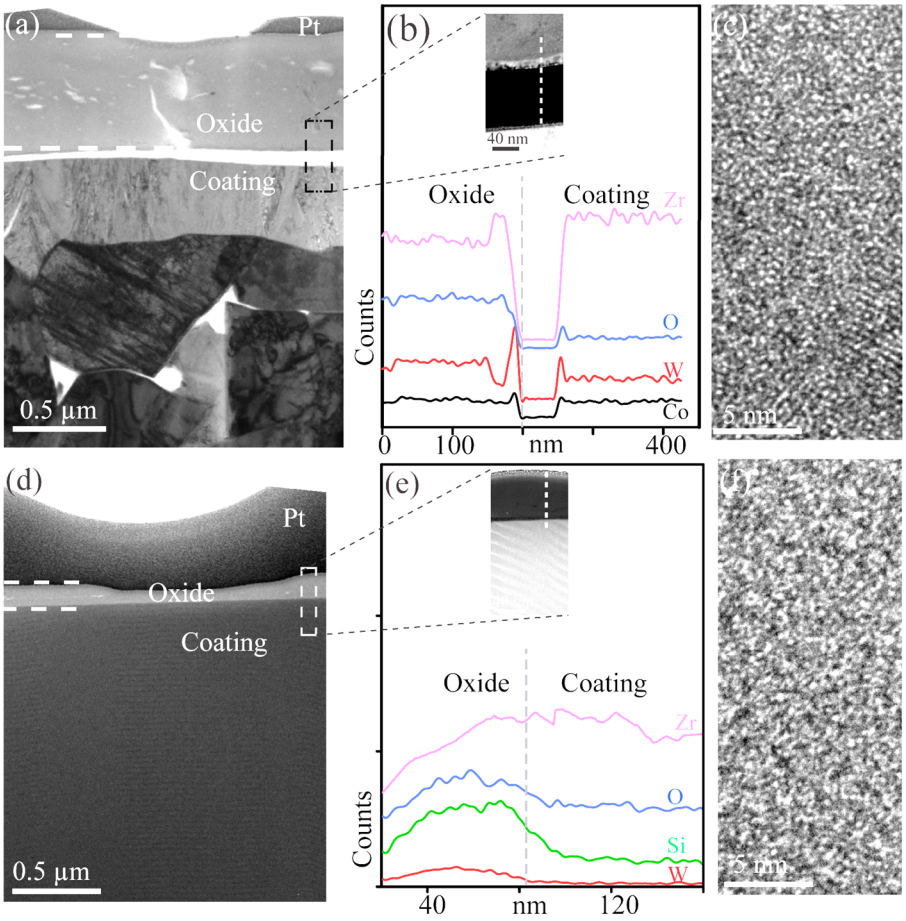

Figure 4. TEM analysis of lamellas beneath the wear tracks of the coatings after RT tests: (a-c) 1.8 at% Si, and (d-f) 6.3 at% Si. (a, d) are BF-TEM micrographs, (b, e) are EDX spectra with STEM micrographs insets having white vertical dotted lines that indicate the regions of the EDX scans, and (c, f) are HR- TEM micrographs of the oxides. Grey markers in EDX spectra (b, e) are for visual guidance to distinguish between oxide and coating.

The inserted STEM image in Fig. 4b shows a homogeneous tribolayer with a bright contrast region, approximately 10 nm thick, near the delaminated interface. Comparing EDX-spectra recorded from the tribolayer and the coatings indicates higher concentrations of O, Zr, and W in the tribolayer, which suggests it to be predominantly a tungsten containing zirconium oxide. The EDX spectra also reveal enrichment of W and Co at the delaminated interface between the tribolayer and the coating giving the bright contrast region in the STEM image.

For the nanocomposite 6.3 at% Si coating, the observed oxide layer is thin (~ 80 nm), continuous, and well adhered to the coating (Fig 4d and e). The tribolayer consists of silicon and zirconium oxides, with traces of W. The tribolayer is richer in Si than the coating. Lattice resolved TEM images (Fig. 4c and f) show that the tribolayers are dominated by an amorphous structure with isolated nano-crystalline regions for both the columnar and nanocomposite structure.

Hardness and elastic modulus of the tribooxide layer were found to be comparable for all the coatings with values of 4 ±1 GPa and 80 ±10 GPa, respectively. To further explore the mechanism of superior tribooxidation resistance of the nanocomposite coatings, static oxidation tests were performed.

3.3 Oxidation studies

Figure 5 shows SEM micrographs of Zr-Si-N coatings after being subjected to oxidation. The oxide layer thickness is about 3, 2, and 1 μm for the coating with 0.2, 1.8 and 6.3 at% Si, respectively, suggesting an increased oxidation resistance of ZrN coating with Si addition. We also note a change of the oxide layer's morphology as the Si-content is increased.

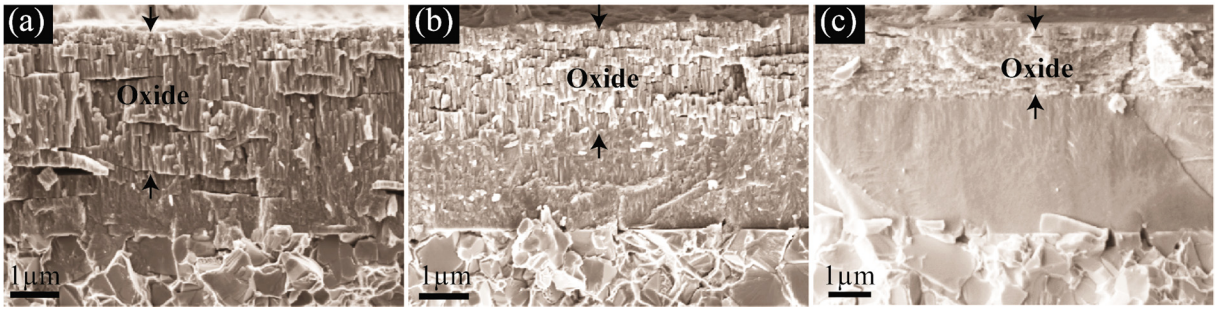

Figure 5. SEM micrographs of fractured cross-sections of oxidized Zr-Si-N coatings, (a) 0.2 at% Si, (b) 1.8 at% Si, and (c) 6.3 at % Si.

Figure 6a shows the relative mass change of the powder extracted from the coatings when oxidized in air. The onset temperature of oxidation was measured to be 590, 620, and 640 °C for 0.2, 1.8 and 6.3 at% Si respectively. Thereafter, the coatings display a constant mass gain rate as a function of temperature with a value of 0.12 %, 0.11 % and 0.06 % for 0.2, 1.8 and 6.3 at% Si respectively.

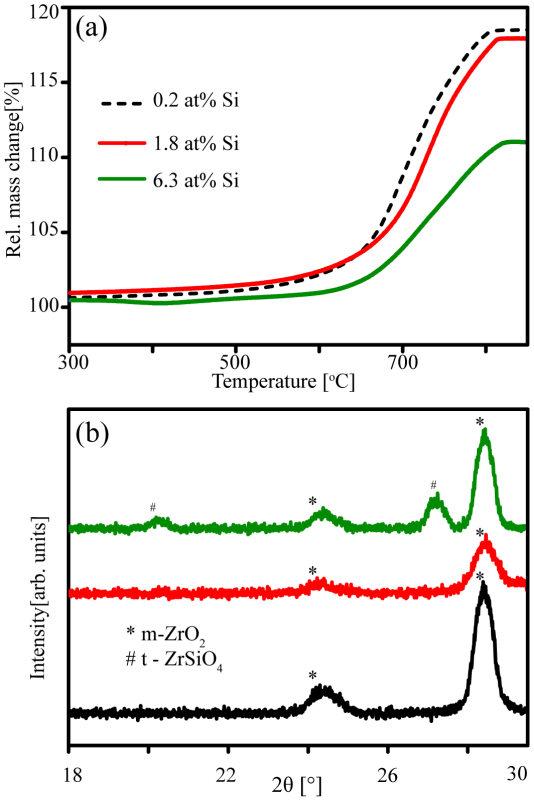

Figure 6. (a) Relative mass changes of coatings in air as a function of temperature, (b) Corresponding x- ray diffractograms of powder after subjecting to oxidation process.

The oxidation behavior is rather similar when comparing samples between 0.2 and 1.8 at% Si, while the data indicates a 40% reduction in the oxide growth rate of the 6.3 at% Si coating with a nanocomposite structure compared to the one with 0.2 at% Si with columnar structure. The x-ray diffractograms in Fig. 6 only display a monoclinic (m) ZrO_2 phase for 0.2 and 1.8 at% Si coatings, while coatings with 6.3 at% Si displays also a tetragonal (t) -$ZrSiO_4$ phase. This indicates that the higher oxidation resistance of the coatings with Si addition is related to the formation of t-$ZrSiO_4$ phase.

3.4 High temperature wear test

Figure 7 shows the wear rate of the coatings tested at 500 °C, and using a contact force of 10 N, which corresponds to a Hertzian contact pressure of 1600 MPa. The inset shows surface profiles of the wear track where the sample with 6.3 at% Si exhibits the deepest track, less for 0.2 at% Si, and the most shallow for 1.8 at% Si.

Wear rate of the coatings decreases with increasing Si content up to 1.8 at% with a minimum value of 10.5 x 10^{-5} mm^3/Nm. Further Si additions increase the wear rate and a value of 61 x 10^{-5} mm^3/Nm is recorded for the sample with 6.3 at% Si. That is, samples with a columnar microstructure have a lower wear rate than the ones with a nanocomposite microstructure.

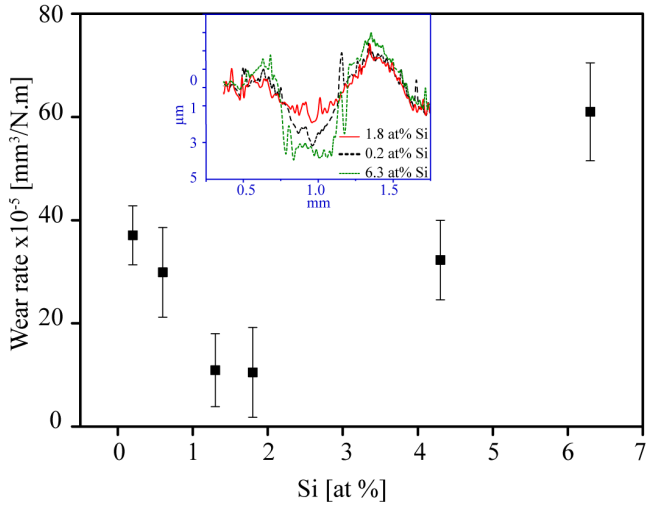

Figure 7. Wear rate of Zr-Si-N coatings as a function of Si content at 500 °C. Inset image shows surface profile of the wear track.

Furthermore the coatings with high hardness show high wear resistance, which is the opposite to the RT tribological response, see section 3.2. All the coatings display a steady state coefficient of friction between 1.4 and 1.5, which is significantly higher compared to the RT tests.

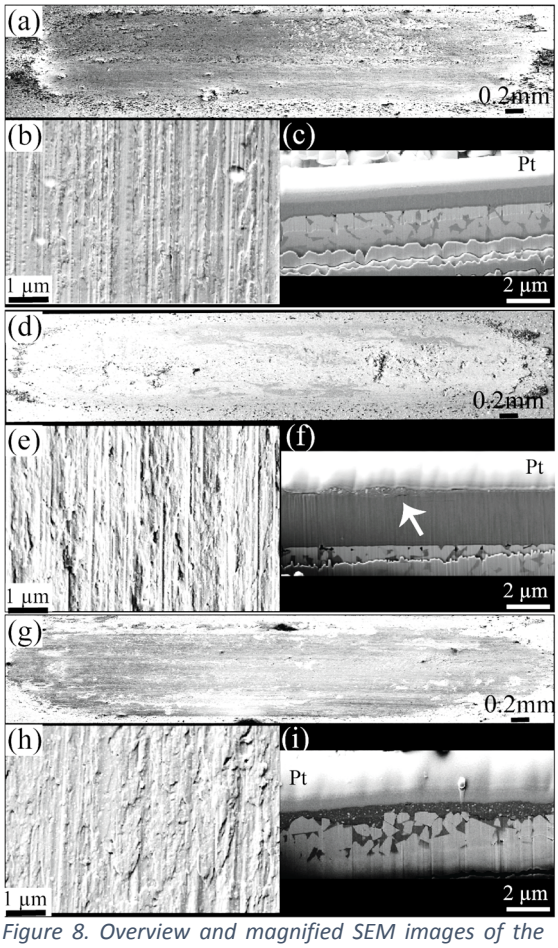

Figure 8. Overview and magnified SEM images of the wear tracks on coatings at a test temperature of 500 °C, and corresponding FIB prepared cross-sections beneath the wear track, (a-c) 0.2 at% Si, (d-f) 1.8 at% Si, and (g-i) 6.3 at. % Si. White arrow in (f) indicates crack formation beneath the wear track.

Figure 8 shows an overview and magnified plan view SEM micrograph of the wear tracks characterized by torn away material and deep grooves in the sliding direction, indicating the occurrence of adhesive and abrasive wear.

The wear track also shows discrete white particles, most clearly seen for 6.3 at% Si coating. FIB prepared cross-sectional views (Fig 8c, f and i) reveal a higher residual coating thickness for 1.8 at% Si, followed by 0.2 at% Si and 6.3 at% Si, which is in line with the measured wear rates. Also we note that nanocomposite coating shows uniformly embedded white particles under the wear track. The 1.8 at% Si coating also displays such embedded white particles along with lateral cracks at some locations.

Cross-sectional STEM micrograph of the lamellae extracted under the wear track of columnar (1.8 at% Si) and nanocomposite coating (6.3 at%) are shown in Fig. 9. The coating with 1.8 at% Si shows a thin tribolayer with a thickness of ~ 200 nm, consisting uniformly distributed white particles (Fig. 9a). The coating also displays subsurface lateral cracks which are connected with the vertical and inclined cracks where the tribolayer penetrate in to the virgin coating. EDX line scan (Fig. 9b) along with the point measurements (not shown here) indicate that the tribolayer is a zirconium tungsten oxide and the white particles are WC from the counter surface. These observations suggest that a tribolayer formed through compaction of the fine wear debris from both coating and the counter material under the contact stress.

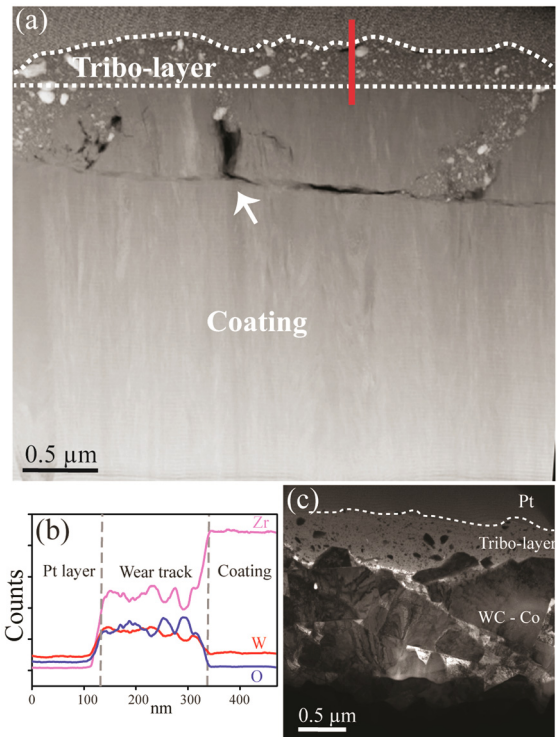

Figure 9. (a) STEM micrograph of a lamellae beneath the wear track of a Zr-Si-N coating with 1.8 at. % Si, after tested at 500 °C, (b) line scan EDX spectrum recorded along the red line in (a), and (c) BF-TEM micrograph of the lamellae under the wear track in 6.3 at% Si coating.

For the nanocomposite coating (Fig. 9c), the cross-sectional micrograph shows only the tribolayer attached to the substrate with a crack at the interface, indicating that the virgin coating is already consumed. These results suggest that the dominant wear mechanism at high temperature is the combination of deformation and fracture in place of the tribooxidation observed at room temperature.

3.5 Microwear tests

Figure 10 a shows the wear rate of the coatings in a microscale reciprocating sliding contact of a diamond tip at RT using a normal force of 10 mN, which generates a Hertzian contact pressure of 19 GPa.

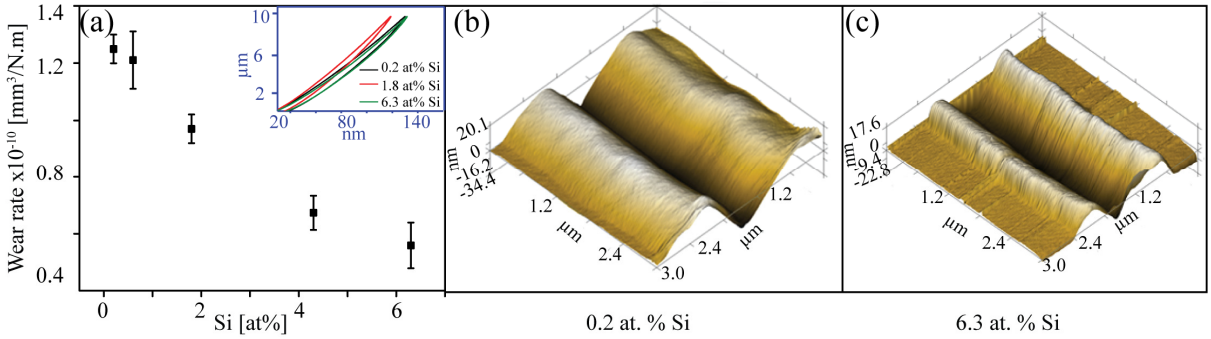

Figure 10. (a) Microscale wear rate of Zr-Si-N coatings as a function of Si-content (inset image shows P-h curves), (b and c) 3D profiles of the wear tracks.

The coatings display a monotonic decrease in the wear rate as a function of Si content up to 6.3 at% with a minimum value of 0.56 x 10^{-10} mm^3/Nm, i.e. nanocomposite coatings exhibit the highest wear resistance. The measured coefficients of friction in this test are significantly lower (0.15-0.17) for all of the coatings, which also explain their significantly lower wear rates. 3D profiles of the wear tracks (Fig. 10b and c) show groves accompanied with pileup on the sides of the wear track for both the columnar and nanocomposite coatings. The columnar 0.2 at% Si coating shows deeper groove and a larger material pile up compared to the nanocomposite structure with 6.3 at% Si coating. The ratio of groove volume to material pile up was measured close to 1 for both the columnar and nanostructured coatings. No loose debris either inside or adjacent to the wear track was detected. Instead the material pile up is caused by material flow due to the induced stress field under the sliding contact, similar to the situation during quasi-static indentation [17]. The inset *P- h* (load-displacement) curves of a quasi-static spherical indentation at a force of 10 mN (Fig. 10a) shows limited plasticity with an elastic recovery of ~90 %. Hence, the formed grove and pileup is the result of accumulated plastic deformation over several repeated cycles, similar to a fatigue process.

4. Discussion

Macro- and microscale sliding wear tests performed on Zr-Si-N coatings yield different tribological response given the different contact situations. For instance, the coating with highest wear resistance at RT actually displayed poor wear resistance at HT. The mechanisms governing the tribological response and their relationship to the microstructure and mechanical properties are discussed below.

The tribooxidation is observed for the all the coatings during the RT macroscale tests. A thicker tribooxide layer is formed in the columnar structured coatings, which

causes layer delamination and leads to a higher wear rate. In contrast, in the nanocomposite coating (6.3 at.% Si) a thin tribooxide layer offered higher resistance to delamination and thus elucidates the observed lower wear rates. The formation of a tribooxide layer is attributed to a contact induced oxidation process, where the oxide layer thickness increases as the sliding progresses. The wear tracks (Fig.4a and d) show a continuous tribolayer without any inter-particle boundaries. Thus the possibility of the tribooxide layer to be formed by accumulation of wear debris is ruled out.

The thermodynamic driving force for the oxidation process is associated with an energy release of 180 kcal.mol^{-1} [19] when transforming ZrN to ZrO_2. A high local flash temperature associated with friction induced heating provides the necessary energy for the transformation. The combination of thermal and mechanical energy in a tribosystem has been shown to reduce the activation energy for tribochemical reactions [20] and facilitates the tribooxidation of ZrN even at room temperature, similar to what has been observed for TiN [21,22]. For both the columnar and nanocomposite coatings, the tribooxide layers attained amorphous structure unlike crystalline oxide in the case of static oxidation. A lower diffusivity of the oxidizing species during RT tribooxidation favors amorphization also reported for TiN based coatings in a sliding contact at RT [24]. The amorphous tribooxide layer has voids and cracks, which results in low hardness (H ~ 4 ±1 GPa) and elastic modulus (E ~ 80 ±10 GPa). The softer tribolayer is subjected to a microcutting process by the wear debris, more clearly seen for the nanocomposite coatings, which explains the abrading action on the tribolayer (Fig. 3c).

The delamination of the thicker tribolayer for the columnar structured coating is attributed to a volumetric mismatch between the oxide and the coating generating shear stress at the oxide/coating interface. The magnitude of the shear stress increases with increasing oxide layer thickness and at a critical thickness the tribolayer delaminates. The interface between the tribolayer and the coating is the plane where cracks preferentially nucleate and propagate (Fig. 4a).

The columnar structured coatings display an increased wear rate between 0.2 and 1.8 at% Si (Fig. 2), despite of their increased static oxidation resistance (Fig. 5). This anomaly originates from the fact that the wear rate is not only determined by the

oxide growth rate but also by the resistance to the delamination process. The 1.8 at% Si coating shows lower resistance to delamination than 0.2 at% Si coating, observed from the lower critical thickness of the tribolayer in Fig 3c and f. A possible explanation for the lower critical thickness of the tribolayer is that the harder coating with 1.8 at% Si may accommodate relatively lower shear strain compared to the softer coating with 0.2 at% Si similar to what has been shown for the adhesive strength between the coating and substrate [23].

The nanocomposite structures with 6.3 at% Si shows high resistance to both static and tribooxidation, however, a comparative difference with low Si containing coatings was found remarkably higher for tribooxidation. The superior static oxidation resistance of nanostructured coating is associated to the formation of t-$ZrSiO_4$. It has been reported that substitution of ZrO_2 (the phase found in low Si containing columnar coatings) by $ZrSiO_4$ slows down the oxygen diffusion and thus increase the oxidation resistance [25]. From the TEM-EDX analysis we expect that the amorphous oxide layer in the case of tribo-oxidation is dominantly $ZrSiO_4$. Moreover, the amorphous oxide layer does not have grain boundaries. The combined effect is a lack of fast diffusion pathways for the oxidizing species and thus explains the superior resistance to tribooxidation of the nanocomposite coating.

In the elevated temperature wear test, the dominating wear mechanism is deformation and fracture of the coating causing a higher wear rate compared to room temperature test. Although it is expected that the high temperature test accelerates the tribooxidation, it is a diffusion driven process and time dependent phenomena. As a consequence, even before the onset of tribooxidation, the coatings are subjected to deformation dominant wear processes due to the combined action of higher contact stress and the thermal softening of the coating material. The two dominant wear mechanisms for the high temperature tests are, (a) microploughing of the coating surface, and (b) subsurface cracking observed for the columnar structured coating. Microploughing of the coatings is caused by the abrasive action of the WC particles likely generated by asperity breakage and transfer of the counter material. The high plastic strain in the coatings associated with microploughing lead to a high COF with a value between 1.4 and 1.5. The high COF causes higher tensile stresses at the trailing edge of the sliding contact [26], which is the most likely mechanism responsible for crack formation in the coating subsurface (Fig. 9a). Based on the

electron microscopy observation of the wear track after the test, it is difficult to ascertain the individual contribution of these mechanisms precisely. The measured wear resistance follows the hardness trend of the coatings (Fig. 7), which indicates that microploughing is the dominant wear mechanism. This is also supported by the observation that the crack formation is confined to relatively small areas in the coating (Fig 8f).

In the multipass microwear sliding tests, the diamond tip forms a wedge shaped wear track accompanied with material pile-up on each side (Fig. 10 b and c). Since the contact is primarily elastic with a minor plastic component (Fig. 10a), the observed deformation is attributed to the accumulation of plasticity over several repeated cycles. Higher hardness implies higher resistance to contact induced deformation and accordingly the wear rate reduces with increasing Si-content up to 1.8 at%. Further increase in Si results in hardness reduction (Table 1), as a consequence of strain localization caused by the grain boundary mediated deformation mechanism in the nanocomposite structure as shown previously [17]. It was shown that the dislocation mediated homogeneous deformation in the columnar structured coatings results in material pile up around an indentation cavity, whereas the grain boundary mediated deformation mechanism in the nanocomposite coating form shear bands on the edge of the indent cavity.

In the current study, the 3D surface profile of the microscale wear track did not display any shear bands besides the wear track of the nanocomposite coating. In addition, the comparable pile-up to wedge volume ratio between the columnar and nanocomposite coatings indicate that wedge formation is caused by dislocation-mediated deformation for both the coatings. The difference in the deformation mechanism of the nanocomposite coating between the sliding contact in the current study and the previous static indentation is likely explained by the difference in the contact stress field, i.e. a dominant elastic stress field in the former case (inset Fig. 10 a) and a fully developed plastic zone in the later. The limited plasticity in the sliding contact might not provide the necessary conditions to cause a collective atomic rearrangement that triggers grain boundary sliding. As a consequence, nanocomposite coating displays higher resistance to groove formation by constraining the dislocation motion, which leads to higher wear resistance. The limited plasticity in the sliding contact keeps the ploughing-induced friction

component low, and the counter surface of a diamond tip is significantly harder than the coating material, causing low contributions of adhesion. As a consequence, the microscale wear tests display significantly lower coefficient of friction of 0.15 to 0.17 and a reduction of the wear rate by four orders of magnitude compared to the macroscale tribological sliding tests.

5. Conclusions

Zr-Si-N coatings were grown on WC-Co substrates by reactive cathodic arc deposition. Si content of the coatings was varied between 0.2 and 6.3 at% Si to cause systematic changes in microstructure and mechanical properties. The tribological response of these coatings under macro-and microscale wear tests with a reciprocating dry sliding contact shows a transition in the dominant wear mechanism by varying the contact force and the test temperature.

In a macro scale wear test, when the sliding is performed at room temperature and lower contact stress, tribooxidation is the dominant wear mechanism. The columnar structured coatings form thick tribolayers, and their delamination leads to high wear rates. On the other hand, nanocomposite coatings form thin and strongly adhered oxide layers with lower wear rate. The superior tribooxidation resistance of the nanocomposite coating is attributed to the formation of an amorphous oxide diffusion barrier layer consisting of Zr, Si and W. At higher temperature, the softening of the coatings combined with the higher contact stress cause microploughing by the abrasive action of WC particles from the counter surface. It results in a high COF of 1.4 and high wear rate while the harder columnar coatings display higher resistance to surface deformation by microploughing.

Microscale wear test of the coatings shows wedge formation accompanied with material pile-up, which is ascribed to the accumulation of dislocation mediated plasticity under the sliding contact. The plasticity is induced over several repeated cycles from a dominantly elastic contact. Such sliding contact results in a low COF of 0.16 and the dislocation confinement in the nanocomposite coating leads to a low wear rate of 5.59×10^{-11} mm^3/Nm.

Finally, this study suggests that the Zr-Si-N coatings with a columnar structure and a high Si content must be aimed to combine high hardness, high fracture resistance

and high oxidation resistance that likely results high macroscale wear resistance both at room temperature and high temperature.

Acknowledgements

The Swedish research council (VR grant no 621- 2012-4401), the Swedish Foundation for Strategic Research (SSF) through the program MultiFilms (RMA08-0069), Swedish government strategic research area grant in material science AFM – SFO MatLiU (2009-00971), EU's Erasmus Mundus graduate school in Material Science and Engineering (DocMASE), and the Swedish Governmental Agency for Innovation Systems (Vinnova grants VINNMer 2011-03464 and M – Era.net 2013-02355), are gratefully acknowledged for their financial support.

6. References

[1] L. Rogström, M.P. Johansson-Jõesaar, L. Landälv, M. Ahlgren, M. Odén, Wear behavior of ZrAlN coated cutting tools during turning, Surf. Coatings Technol. 282 (2015) 180–187.

[2] L. Rogström, N. Ghafoor, J. Schroeder, N. Schell, J. Birch, M. Ahlgren, M. Odén, Thermal stability of wurtzite $Zr_{1-x}Al_xN$ coatings studied by in situ high-energy x-ray diffraction during annealing, J. Appl. Phys. 118 (2015) 035309.

[3] K. Yalamanchili, I.C. Schramm, E. Jiménez-Piqué, L. Rogström, F. Mücklich, M. Odén,N. Ghafoor, Tuning hardness and fracture resistance of ZrN/$Zr_{0.63}Al_{0.37}N$ nanoscale multilayers by stress-induced transformation toughening, Acta Mater. 89 (2015) 22–31.

[4] S. Vepřek, M. Haussmann, S. Reiprich, L. Shizhi, J. Dian, Novel thermodynamically stable and oxidation resistant superhard coating materials, Surf. Coatings Technol. 86-87 (1996) 394–401.

[5] A. Flink, T. Larsson, J. Sjölén, L. Karlsson, L. Hultman, Influence of Si on the microstructure of arc evaporated (Ti,Si)N thin films; evidence for cubic solid solutions and their thermal stability, Surf. Coatings Technol. 200 (2005) 1535–1542.

[6] J. Patscheider, T. Zehnder, M. Diserens, Structure-performance relations in nanocomposite coatings, Surf. Coat. Technol. 146 (2001) 201–208.

[7] H. Söderberg, M. Odén, T. Larsson, L. Hultman, J.M. Molina-Aldareguia, Epitaxial stabilization of cubic-$SiN_{[x]}$ in TiN/$SiN_{[x]}$ multilayers, Appl. Phys. Lett. 88 (2006) 191902.

[8] M. Nose, M. Zhou, T. Nagae, T. Mae, M. Yokota, S. Saji, Properties of Zr - Si - N coatings prepared by RF reactive sputtering, Surf. Coatings Technol. 132 (2000) 163–168.

[9] T. Mae, M. Nose, M. Zhou, T. Nagae, K. Shimamura, The effects of Si addition on the

structure and mechanical properties of ZrN thin films deposited by an r.f. reactive sputtering method, Surf. Coatings Technol. 142-144 (2001) 954–958.

[10] D. Pilloud, J.F. Pierson, A. P. Marques, A. Cavaleiro, Structural changes in Zr–Si–N films vs. their silicon content, Surf. Coatings Technol. 180-181 (2004) 352–356.

[11] M. Nose, W. A. Chiou, M. Zhou, T. Mae, M. Meshii, Microstructure and mechanical properties of Zr–Si–N films prepared by rf-reactive sputtering, J. Vac. Sci. Technol. A Vacuum, Surfaces, Film. 20 (2002) 823.

[12] Y. Dong, W. Zhao, Y. Li, G. Li, Influence of silicon on the microstructure and mechanical properties of Zr–Si–N composite films, Appl. Surf. Sci. 252 (2006) 5057–5062.

[13] X. Cao, T. Shao, S. Wen, Y. Yao, Micro/Nanotribological and Mechanical Studies of TiN Thin-Film for MEMS Applications, Tribol. Trans. 47 (2004) 227–232.

[14] A. Leyland, A. Matthews, On the significance of the H/E ratio in wear control: A nanocomposite coating approach to optimised tribological behaviour, Wear. 246 (2000) 1–11.

[15] J. Musil, Hard and superhard nanocomposite coatings, Surf. Coatings Technol. 125 (2000) 322–330.

[16] D. Pilloud, J.F. Pierson, J. Takadoum, Structure and tribological properties of reactively sputtered Zr–Si–N films, Thin Solid Films. 496 (2006) 445–449.

[17] K. Yalamanchili, R. Forsén, E. Jiménez-Piqué, M.P. Johansson Jöesaar, J.J. Roa, N. Ghafoor, M. Odén, Structure, deformation and fracture of arc evaporated Zr–Si–N hard films, Surf. Coatings Technol. 258 (2014) 1100–1107.

[18] W.C. Oliver, G.M. Pharr, Measurement of hardness and elastic modulus by instrumented indentation: Advances in understanding and refinements to methodology, J. Mater. Res. 19 (2011) 3–20.

[19] L. Krusin-Elbaum, M. Wittmer, Oxidation Kinetics of ZrN Thin films, Thin Solid Films, 107 (1983) 111–117.

[20] G. Kaupp, Mechanochemistry: the varied applications of mechanical bond-breaking, Cryst. Eng. Comm. 11 (2009) 388.

[21] E. Vancoille, B. Blanpain, Y. Xingpu, J.-P. Celis, J.R. Roos, Tribo-oxidation of a TiN coating sliding against corundum, J. Mater. Res. 9 (1994) 992–998.

[22] S. Wilson, A.T. Alpas, Tribo-layer formation during sliding wear of TiN coatings, Wear. 245 (2000) 223–229.

[23] C. Zhang, T. Hu, N. Zhang, Influence of substrate hardness on coating-substrate adhesion, Adv. Mater. Res. 177 (2010) 148-150.

[24] Q. Luo, P.E. Hovsepian, D.B. Lewis, W.D. Münz, Y.N. Kok, J. Cockrem, et al., Tribological properties of unbalanced magnetron sputtered nano-scale multilayer coatings TiAlN/VN and TiAlCrYN deposited on plasma nitrided steels, Surf. Coatings Technol. 193 (2005) 39–45.

[25] A.C.Y. Tsai, C.C. Lin, A. Zangvil, and A.K. Li, Effect of Zirconia Content on the Oxidation Behavior of Silicon Carbide/Zironia/Mullite Composites. J. Am. Ceram. Soc. 81(1998) 2413-2420.

[26] K. Kato, Wear in relation to friction - A review, Wear. 241 (2000) 151–157.

Paper III

Tuning hardness and fracture resistance of $ZrN/Zr_{0.63}Al_{0.37}N$ nanoscale multilayers by stress-induced transformation toughening

K. Yalamanchili, I.C. Schramm, E. Jiménez-Piqué, L. Rogström, F. Mucklich, M. Odén, N. Ghafoor

Acta Materialia 89 (2015) 22–31

Paper IV

Growth and thermal stability of TiN/ZrAlN: Effect of internal interfaces

K. Yalamanchili, F. Wang, H. Aboulfadl , J. Barrirero , L. Rogström , E. Jiménez-Pique , F. Mücklich , F. Tasnadi, M. Odén, N. Ghafoor

Accepted in Acta Materialia

Growth and thermal stability of TiN/ZrAlN: Effect of internal interfaces

K. Yalamanchili[a,c], F. Wang[a,b], H. Aboulfadl[b], J. Barrirero[b], L. Rogström[a], E. Jiménez-Pique[c, d], F. Mücklich[b], F. Tasnadi[a], M. Odén[a], N. Ghafoor[a]

[a] *Department of Physics, Chemistry, and Biology (IFM), Linköping University, SE 581 83 Linköping, Sweden*

[b] *Functional Materials, Department of Materials Science, Campus D3.3, Saarland University, D 66123 Saarbrücken, Germany*

[c] *Departamento de Ciencia de los Materiales e Ingenieri´a Metalurgica, Universitat Polite`cnica de Catalunya, Barcelona, Spain*

[d] *Center for Research in Nanoengineering, CRnE-UPC, Barcelona, Spain*

Abstract

Wear resistant hard films comprised of cubic (*c*) transition metal nitride (TMN) and metastable *c*-AlN with coherent interfaces have a confined operating envelope governed by the limited thermal stability of metastable phases. However, equilibrium phases (*c*-TMN and wurtzite (*w*) AlN) forming semicoherent interfaces during film growth offer higher thermal stability. We demonstrate this concept for a model multilayer system with TiN and ZrAlN layers where the latter is a nanocomposite of ZrN- and AlN- rich domains. The interface between the domains is tuned by changing the AlN crystal structure by varying the multilayer architecture and growth temperature. The interface energy minimization at higher growth temperature leads to formation of semicoherent interfaces between *w*-AlN and *c*-TMN during growth of 15 nm thin layers. *Ab initio* calculations predict higher thermodynamic stability of semicoherent interfaces between *c*-TMN and *w*-AlN than isostructural coherent interfaces between c-TMN and *c*-AlN. The combination of a stable interface structure and confinement of *w*-AlN to nm-sized domains by its low solubility in *c*-TMN in a multilayer, results in films with a stable hardness of 34 GPa even after annealing at 1150 °C.

Key words

Thermal stability, TM-Al-N multilayer films, Nanostructured materials, Interface energy, Three-dimensional atom probe (3DAP), Transmission electron microscopy,

1. Introduction

Development of new materials for wear resistant coatings with high hardness at elevated temperature is a long- standing technological challenge. The current workhorse material for the wear resistant coatings on metal cutting tool inserts is TiAlN with 50 - 67 at% of Al on the metallic sublattice [1–3]. TiAlN exhibits hardness enhancement at annealing temperatures between 700 and 900 °C due to

spinodal decomposition of the supersaturated cubic (*c*)-TiAlN solid solution into *c*-TiN and metastable *c*-AlN [4–9]. The isostructural domains form coherent interfaces contributing to the age hardening. However the lattice coherency breaks down above 900 °C when *c*-AlN transforms to the thermodynamically stable wurtzite (*w*) phase [6]. The resulting incoherent interfaces cause a hardness drop and thus limit the working envelope of the film [6]. Several approaches, such as multicomponent alloying [10–13], multilayering [14,15], and interface coherency strain tuning [16] have been developed to enhance the stability of the metastable *c*-AlN with respect to *w*-AlN. Nevertheless, there is a temperature limit around 1000 °C [15], above which the metastable *c*-AlN assumes its thermodynamically stable wurtzite structure. A volume expansion associated with the transformation leads to structural instability which further deteriorates the mechanical properties of the material [17].

Here, we investigate an alternative material design route to improve the thermal stability of TM-Al-N films, i.e, instead of forming AlN in the metastable cubic phase we propose to grow it in its stable wurtzite structure but with semicoherent interfaces to *c*-TMN. The concept originates from recent experimental studies by us and others showing films consisting *w*-AlN with semicoherent interfaces to display higher hardness similar to the films containing *c*-AlN [18–21]. It exposes the fact that even though *w*-AlN has a lower shear resistance [22], films containing *w*-AlN could be strengthened by growing them such that semicoherent interfaces are formed. The current knowledge of semicoherent growth of *w*-AlN is, however, limited [19,20,23], and their thermal stability is yet to be studied. These topics are addressed in this article using TiN/ZrAlN as a model system.

ZrAlN is an immiscible alloy with a maximum enthalpy of mixing around $Zr_{0.4}Al_{0.6}N$, the composition chosen in this study [24,25]. During high temperature growth the alloy segregates to its binaries ZrN and AlN [18]. By adapting a multilayer structure it is known that the crystal structure of AlN can be tuned between the cubic and wurtzite phases by varying the layer thickness [26–28]. Here we combine these phenomena and vary the growth temperature to switch between isostructural (*c*-TMN/*c*-AlN) and hetrostructural (*c*-TMN/*w*-AlN) with coherent or semicoherent interfaces in the magnetron sputtered TiN/ZrAlN multilayers. We probe the thermal stability of hetrostructural semicoherent interfaces by measuring the hardness before and after elevated temperature anneals. The relative thermodynamic stability of

isostructural and hetrostructural coherent interfaces are calculated by first principle calculations. The results provide insights in to the interface crystallographic and chemical requirements to enhance the thermal stability of TM-Al-N films to achieve an unaffected high hardness even after annealing to high operational temperatures.

Note the term "interface" is used in the text for both layer interfaces as well as boundaries between chemically segregated domains and collectively all interfaces are referred as "internal interfaces".

2. Experimental and calculation methods

TiN/$Zr_{0.43}Al_{0.57}N$ multilayer films were deposited on MgO (001) substrates in a high vacuum dual DC magnetron sputter deposition system with a background pressure of 2 x 10^{-5} Pa. Details of the deposition chamber can be found elsewhere [29]. A pure Ti and a pre-alloyed $Zr_{0.4}Al_{0.6}$ target with a size of 75 mm diameter were used. The discharge was obtained at N_2 and Ar partial pressures of 0.06 and 0.5 Pa, respectively. Applied powers of P_{Ti} = 200 W (power density ~ 4.5 w/cm^2) and $P_{Zr0.4Al0.6}$ = 150 W (power density ~ 3.4 w/cm^2) resulted in deposition rates of 0.15 (TiN) and 0.18 ($Zr_{0.43}Al_{0.57}N$) nm/s, respectively. The individual layers thicknesses (l) of TiN and $Zr_{0.43}Al_{0.57}N$ in the multilayer structure were controlled by shutters in front of each target. The nominal thickness l_{TiN} was kept constant at 15 nm, whereas l_{ZrAlN} was set to 2, 5, 10, 15, and 30 nm in a growth series of five films.

Monolithic films of TiN and $Zr_{0.43}Al_{0.57}N$ (with a 30 nm thick TiN buffer layer) were also deposited for reference. A total film thickness of about 1 μm was achieved for all samples to ensure reliable hardness measurements. All films were grown at a substrate temperature of T_s = 700 °C. However, an additional multilayer with l_{ZrAlN} = 15 nm was deposited at T_s = 900 °C to ensure growth of *w*-AlN with semicoherent interfaces. This film was further annealed at 1150 °C for 2 hours under controlled atmosphere of 95 % N_2 and 5% H_2 to probe thermal stability.

The composition of the monolithic films was determined by elastic recoil detection analysis (ERDA) using a 40 MeV I^+ beam, having an incident angle of 67.5° with respect to the surface normal, and the recoils were detected at an angle of 45°. The measured ERDA data was converted into relative atomic concentration profiles using the CONTES code [30]. Structural changes were characterized by X-ray diffraction (XRD) with a Panalytical Empyrian diffractometer operated in Bragg-Brentano geometry using Cu-K_α radiation at 40 kV and 40 mA. Transmission electron

microscopy (TEM) and scanning transmission electron microscopy (STEM) were performed using a FEI Tecnai G2 TF 20 UT FEG microscope operated at 200 kV, equipped with an energy- dispersive X-ray analysis spectrometer (EDX). For STEM analysis, a high angular annular dark field (HAADF) detector with a camera length of 160 mm was used. Cross section TEM (XTEM) samples were prepared by conventional mechanical polishing followed by ion milling [21].

Atom probe tomography (APT) was used to obtain quantitative information regarding the interface chemistry. APT was performed on four films; l_{ZrAlN} = 2 and 15 nm (T_s 700°C), l_{ZrAlN} =15 nm (T_s 900°C) in its as-deposited state and after isothermal annealing. Atom probe specimens were prepared in a dual-beam focused ion beam/scanning electron microscopy (SEM) workstation implementing the *in situ* lift out technique [31]. A 200 nm thick Pt layer was electron beam deposited on the film surface to reduce Ga implantation during specimen preparation. The measurements were carried out using a LEAP™ 3000X HR CAMECA™ system operated in laser pulsing mode (532 nm wavelength) with a repetition rate of 160 kHz, base temperatures of 40-50 K, and laser pulse energies of 0.4-0.5 nJ. The data were reconstructed using the standard algorithm developed by Bas et al. [32] and analyzed with the software CAMECA™ IVAS 3.6.8.

First principle calculations were performed to compare the relative thermodynamic stabilities between isostructural and hetrostructural interfaces. The total energy calculations were performed within the density functional theory (DFT) using the projector augmented wave (PAW) approach [33] implemented in the Vienna Ab initio Simulation Package (VASP) [34]. The Perdew-Burke-Ernzerhof generalized gradient functional (PBE-GGA) [35] was used to approximate the exchange and correlation functional. A plane-wave energy cutoff value of 450 eV was used. The reciprocal space integration was performed within the Monkhorst-Pack scheme [36] using a k-mesh of 5×5×1. To determine the thermodynamic equilibrium configuration of the multilayers, the in-plane lattice parameter, the c/a ratio, and all the atomic coordinates were relaxed.

Multilayers of TiN/AlN and ZrN/AlN were modeled with different interface structures. Fig. 1 shows the models together with the interfacial matching. The models were built with 1:1 metal-to-metal atomic ratio between the parental slabs (TiN, ZrN and AlN), a condition which results in different slab thicknesses for the

different multilayers. The in-plane size and the thicknesses were varied until the relative energy differences between the different multilayers (a-d) were converged. This was achieved for in-plane sizes made by the (2x2) repetition of the black skeletons shown in Fig. 1. Convergence was achieved using 192 atoms in the models. This means in total 96 metal atoms for the (a), (c) and (d) multilayers. The multilayer (b) does not commensurate with the other three models in terms of the number of metal atoms therefore its total energy was derived by a linear interpolation of the energies calculated with models built from 72 and 168 metal atoms.

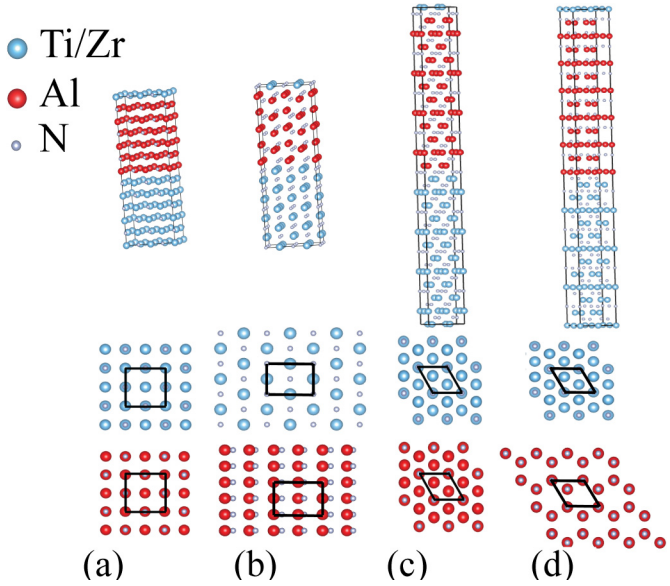

Figure1: Multilayer models and the corresponding interfacial matchings (black skeletons). (a) c-(100)[001]//c-(100)[001], (b) c-(110)[001]//w-(10-10)[001], (c) c-(111)[1-10]//c-(111)[1-10], (d) c-(111)[1-10]//w-(0001) [11-20].

Hardness and Young's modulus were obtained using a load-controlled UMIS nano indenter equipped with a Berkovich diamond indenter with a tip radius of approximately 150 nm. An optimum load of 12 mN was selected to avoid substrate effects and obtain load independent mechanical properties. A minimum of 30 indents for each film were used to evaluate the average and standard deviation of the hardness (H) and elastic modulus (E) using the Oliver and Pharr method [37].

3. Results

3.1. Composition

The as deposited monolithic film compositions were determined to $Zr_{0.43}Al_{0.57}N$ and TiN (± 1.5 at%) with a nitrogen to metal ratio close to 1 ± 0.05. Oxygen and carbon impurities account for less than 0.2 at% while the Ar content is 0.8 at% in the films,

and no preferential segregation of the impurities are observed with in the detection limits. The Al content in the Zr-Al-N film is lower than that of the target by about 3 at%, which stems from preferential re-sputtering of Al during deposition [21,38]. A Quantitative compositional analysis is compared (table. 1) between the multilayers (average of 5 layers) measured by APT analysis and their monolithic counterparts measured by ERDA. The peak overlap between Zr^{+3} and TiN^{+2} ions in the mass spectrum did not permitted for the precise measurement of Zr concentration in APT analysis, and for the rest of the elements results are comparable between two techniques. Measured error is less than 0.05 at. % for both the techniques.

Technique/ Film	location	Avg. Comp. at. %						
		Ti	Zr	Al	N	O	Ar	C
APT/ multilayer	TiN	49.8	--	0.3	49.5	0.1	0.1	0.01
	ZrAlN	0.2	--	28.2	51.3	0.3	0.25	0.01
ERDA/ Monolithic	TiN	49.3	0	0	48.9	0.1	0.5	0.01
	ZrAlN	0	21.6	28.5	48.4	0.1	1	0.01

Table 1. Composition of as deposited monolithic and multilayers measured by ERDA and APT analysis respectively.

3.2. XRD analysis

Fig. 2 shows X-ray diffractograms of the $Zr_{0.43}Al_{0.57}N$ film, multilayers with l_{ZrAlN} = 2, 10, 15 and 30 nm grown at T_s = 700 °C, and the multilayer l_{ZrAlN} = 15 nm grown at T_s = 900 °C in its as deposited and annealed states. The close lattice-match causes TiN 002 and MgO 002 diffraction peaks to overlap and they cannot be resolved in these diffractograms. The monolithic film shows only one weak and broad diffraction signal around 32.4°, interpreted as *w*-AlN 0002. The peak shift to a slightly lower diffraction angle than pure *w*- AlN is attributed to Zr incorporation in the *w*-AlN, whereas the peak broadening reflects the nanocrystalline nature of the film.

The short period multilayers l_{ZrAlN} = 2 and 5 nm exhibit finite thickness fringes around TiN (MgO) 002 diffraction peak indicative of a superlattice nature of these multilayers. The diffraction signal originates entirely from (002) cubic planes, which indicates epitaxial growth of these short period multilayers.

The appearance of a TiN 111 diffraction peak in l_{ZrAlN} = 10, 15, and 30 nm (hereafter, referred to as long period multilayer) suggests polycrystalline growth.

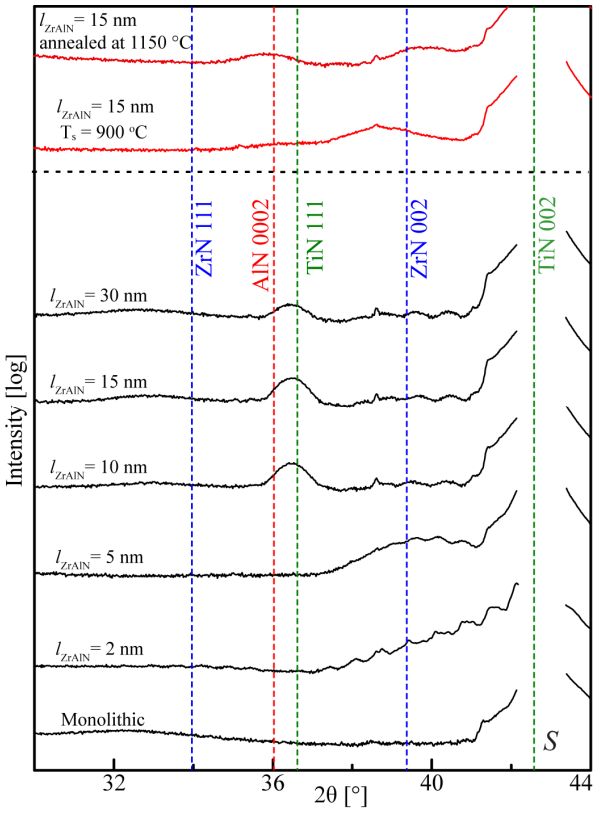

Figure 2: XRD of monolithic $Zr_{0.43}Al_{0.57}N$ film and TiN/$Zr_{0.43}Al_{0.57}N$ multilayers deposited at T_s =700 °C (profiles in black), l_{ZrAlN} =15 nm multilayer deposited at 900 °C and after annealing at 1150 °C (profiles in red).

The absence of *c*-ZrN peaks and the appearance of a broad diffraction peak around 32.4° suggest that the $Zr_{0.43}Al_{0.57}N$ layers in the long period multilayers are structurally similar to the monolithic film.

The multilayer, l_{ZrAlN} =15 nm deposited at T_s = 900 °C shows a distinct diffraction pattern with a single broad peak centered between *c*-ZrN 002 and *w*-AlN 0002 peak positions. Upon annealing at 1150 °C, two broad peaks at 2θ 35.77° and 39.65° appeared. The phase identification in these films is ambiguous and will be addressed later when combining XRD with TEM investigations.

3.3. Microstructure of as-deposited films

3.3.1. Monolithic $Zr_{0.43}Al_{0.57}N$ film

The cross sectional HAADF-STEM image of $Zr_{0.43}Al_{0.57}N$ monolithic film in Fig. 3a shows contrast variation with a wavelength of ~ 3 nm, attributed to the formation of ZrN- and AlN-rich domains during growth. The film displays weak columnar contrast in the bright field TEM image (Fig. 3b). The lattice resolved image reveals a preferentially oriented wurtzite crystal structure in the growth direction. A closer analysis of the image shows that the wurtzite lattice repeatedly interrupts about every 2-3 nm with regions that do not display fringes, hereafter referred to as a distorted structure. The wurtzite lattice corresponds to AlN- rich domains, and the distorted regions correspond to ZrN-rich domains.

The SAED pattern shows wurtzite reflections with 0002 preferentially orientated in the growth direction and, in agreement with the XRD results, no cubic diffraction peaks are observed. The lattice parameters, a ≈ 3.66 Å and c ≈ 5.41 Å determined

from the SAED are larger than the equilibrium lattice parameter of *w*-AlN [39]. Again, this is in agreement with the XRD 0002 peak being shifted with respect to pure *w*-AlN indicating that AlN-rich domains contain Zr.

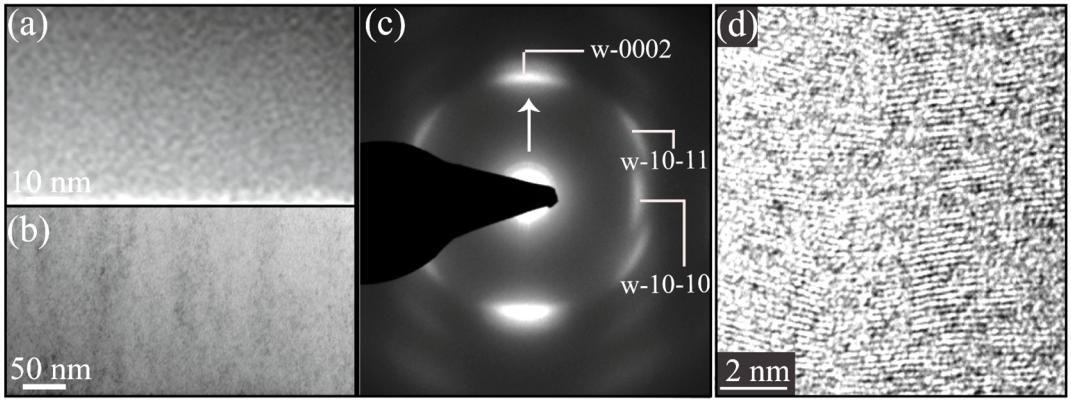

Figure 3: XTEM images of the monolithic $Zr_{0.43}Al_{0.57}N$ film: (a) STEM-HAADF, (b) BF-TEM, (c) SAED (arrow indicates the growth direction), and (d) HR-TEM.

These observations suggest that the segregated monolithic $Zr_{0.43}Al_{0.57}N$ film form a nanocomposite with incoherent interfaces where AlN-rich regions assume a preferentially oriented wurtzite structure and ZrN-rich domains assume a distorted structure. Despite the distorted ZrN-rich domains the nanocomposite film displays a crystallographic texture governed by minimization of the surface energy of *w*-AlN, i.e. <0002> orientation in the growth direction.

3.3.2. Short period multilayers and coherent interfaces

In the short period multilayers (l_{ZrAlN} = 2 and 5 nm) well defined interfaces between TiN and $Zr_{0.43}Al_{0.57}N$ layers are observed in TEM (Fig. 4). STEM images show bright and dark modulations within the $Zr_{0.43}Al_{0.57}N$ layer that correspond to vertical aligned ZrN- and AlN-rich domains with a wavelength of ~2 nm. The SAED patterns only contain cubic diffraction spots along two different zone axis and no wurtzite phase is observed. The lattice resolved images shows cube-on-cube epitaxy between TiN and $Zr_{0.43}Al_{0.57}N$ layers. It means that the AlN- rich domains assume a metastable cubic crystal structure, forming coherent interfaces with both TiN and ZrN, which leads to a self-aligned and compositionally modulated structure (Fig. 4d).

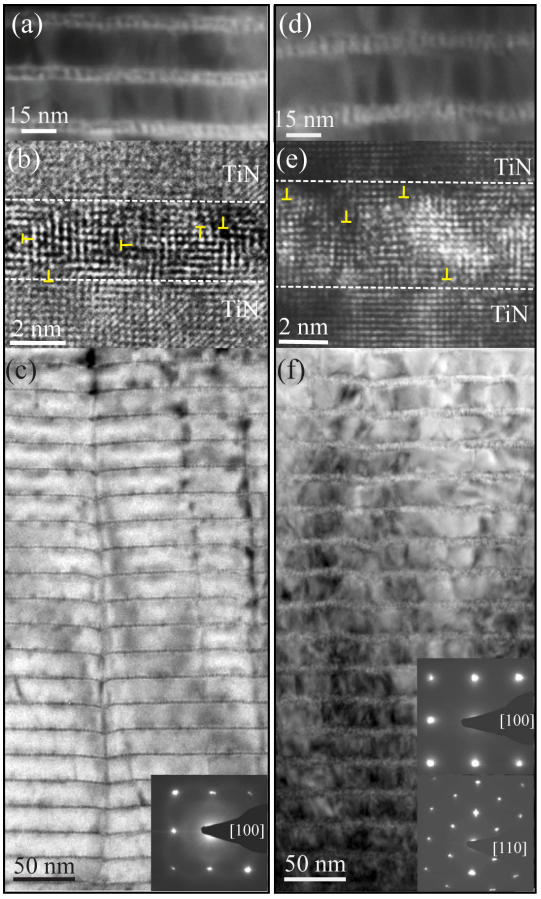

Figure 4: STEM, HR-TEM, and BF-TEM micrograph with SAED insets of short period multilayers grown at 700 °C: (a-c) l_{ZrAlN} = 2 nm, and (d-f) l_{ZrAlN} = 5 nm.

The lattice resolved images (Fig. 4b and e) also show misfit dislocations and the density is higher within the ZrAlN layer, i.e. between the segregated c-ZrN- and c-AlN- rich domains, compared to the interfaces between TiN and ZrAlN layer. This is a consequence of high misfit strain between c-ZrN and c-AlN (~ 10 %) compared to the misfit strain between c-TiN and c-ZrAlN layer (~ 1.5 %).

The bright field TEM image shows continues contrast of threading dislocations in the growth direction, more clearly seen for the multilayer of l_{ZrAlN} = 2nm in Fig 4c, which is typical for epitaxial growth. The epitaxial growth causes correlated layer roughness in the growth direction which was also observed in APT reconstruction of l_{ZrAlN} = 5 nm multilayers as shown in Fig. 5 inset image.

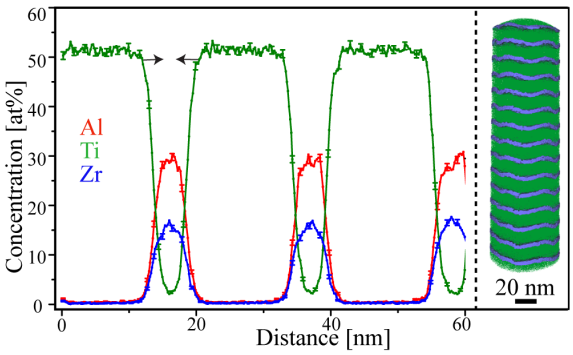

Figure 5: 1D concentration profile of l_{ZrAlN} = 5 nm (nitrogen not shown here) from a localized volume within the APT reconstruction shown in the inset. Black arrows indicate the region of chemical intermixing between the layers.

The 1D concentration profiles from the APT data of the multilayer with l_{ZrAlN} = 5nm (Fig. 5) show an average interface width of ~ 4 nm between the alternating TiN and $Zr_{0.43}Al_{0.57}N$ layers. This implies that the actual $Zr_{0.43}Al_{0.57}N$ layer thickness shrinks to ~ 1 nm, while the rest of the layer consists of ZrN and AlN- rich domains intermixed with Ti. Thus, in epitaxial l_{ZrAlN} = 2 nm multilayer the $Zr_{0.43}Al_{0.57}N$ layers are expected to be fully intermixed with TiN. These observations suggest that the layer composition in short period multilayers significantly deviate from the nominal values and need to be considered when describing metastable phase formation.

3.3.3. Long period multilayers: interface structure versus growth temperature

The multilayer with l_{ZrAlN} = 15 nm was chosen for detailed microstructural analysis since all of the long period multilayers show similar X-ray diffractograms. Fig. 6 shows XTEM images of this multilayer grown at 700 °C (a-c), and 900 °C (d-f), respectively. STEM images at low and high magnifications reveal randomly distributed ZrN- and AlN- rich domains in the ZrAlN layers when grown at T_s = 700 °C. The HRTEM micrograph (Fig. 6c) shows a nanocomposite structure of *w*-AlN-rich and distorted ZrN-rich domains similar to what has been observed in the monolithic film (see Fig. 3a). This suggests that the epitaxy associated with the templating effect of TiN is lost for the long period multilayers (l_{ZrAlN} > 10 nm). Similar to the monolithic film, the ZrAlN layers display a weak 0002 diffraction signal from the *w*-AlN-rich domains in Fig. 6a. The ZrN-rich domains are too small and distorted to result in an observable diffraction signal, whereas the *c*-TiN shows nearly continues diffraction ring. These observations suggest that the *w*-AlN forms incoherent interfaces with both ZrN and *c*-TiN.

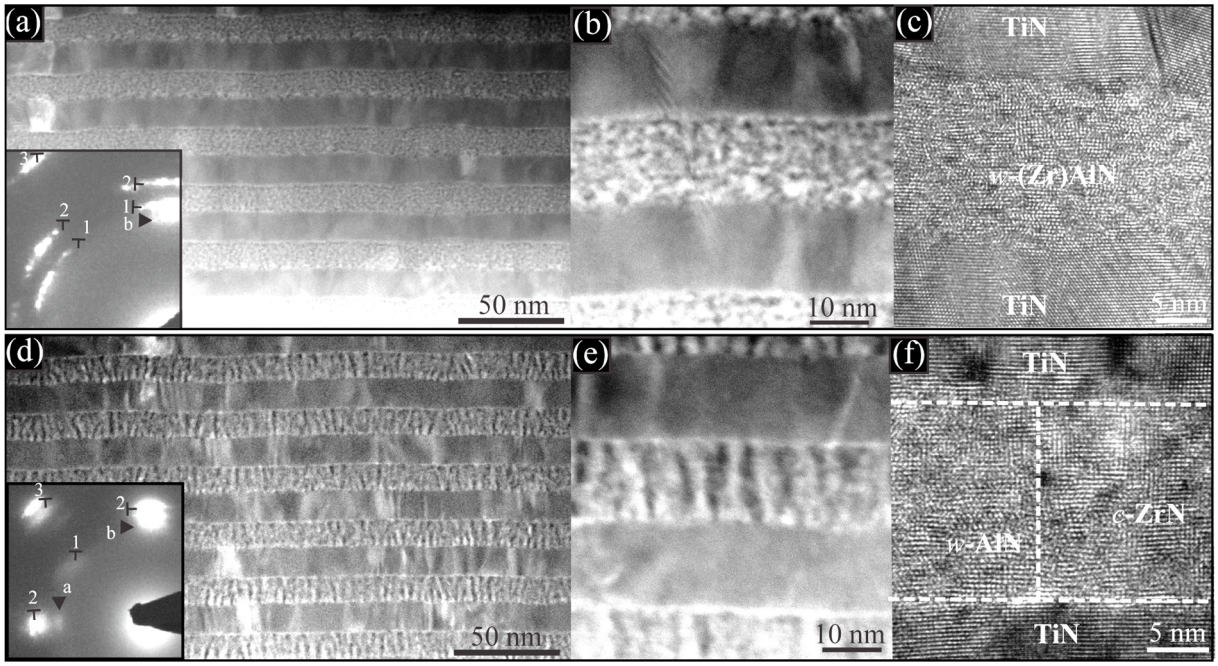

Figure 6: Cross sectional TEM analysis of l_{ZrAlN} = 15 nm multilayers. Overview STEM images with SAED inset, magnified STEM, and HR-TEM images from left to right for the multilayers grown at 700 °C (a-c) and 900 °C (d-f). SAED annotations, 1, 2 and 3 corresponds to cubic-111, 200, 220 reflections, a and b corresponds to wurtzite-10-10 and 0002. The twin diffraction pattern of cubic phase in (d) corresponds to c-TiN and c-ZrN.

In contrast, the STEM micrograph of the multilayer grown at 900 °C reveals a compositionally modulated microstructure with vertically aligned domains within the $Zr_{0.43}Al_{0.57}N$ layer (Fig. 6d and e), similar to what is observed for the short period multilayers. The crystallographically aligned wurtzite and cubic reflections in SAED pattern implies that the *w*-AlN-rich domains form semicoherent interfaces to *c*-ZrN and *c*-TiN. Fast Fourier transform (FFT) of the lattice resolved image in combination with SAED yield a coherency relation of $(110)_{c\text{-}TiN} \parallel (110)_{c\text{-}ZrN} \parallel (10\text{-}10)_{w\text{-}AlN}$ and $[001]_{c\text{-}TiN} \parallel [001]_{c\text{-}ZrN} \parallel [0001]_{w\text{-}AlN}$, here after termed *type I* interfaces. A substrate-film SAED pattern (not shown here) revealed $(100)_{MgO} \parallel (100)_{c\text{-}TiN}$ and $[001]_{MgO} \parallel [001]_{c\text{-}TiN}$.

The lattice resolved image (Fig. 6f) confirms the coherency between *c*-ZrN and *w*-AlN domains, and *c*-ZrN domains and TiN layers. The *type I* interface formation causes an expansion of the *c*-ZrN lattice and a shrinkage of the c-axis of *w*-AlN along the growth direction. This explains the origin of a single broad XRD peak between the *c*-ZrN 002 and *w*-0002 in Fig.2. The weak cubic 111 reflections in the SAED pattern are signatures of an additional orientation which evolves further after annealing the multilayers and it will be addressed in section 3.4.

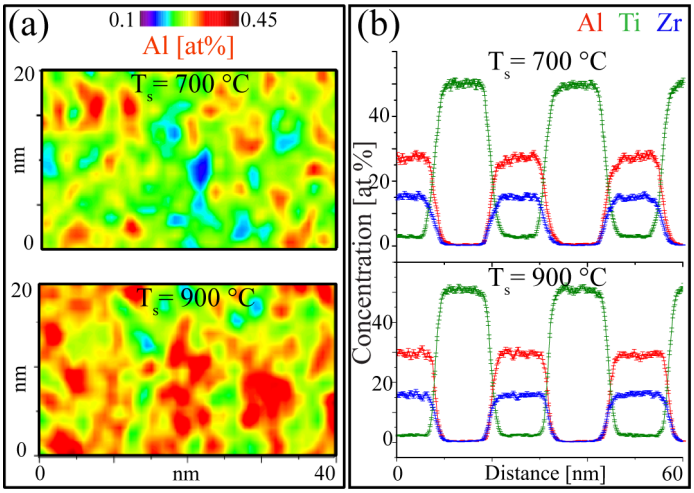

Figure 7: (a) Plan-view 2D concentration map of Al from the $Zr_{0.43}Al_{0.57}N$ layer in l_{ZrAlN} =15 nm multilayer from a localized volume within the APT reconstruction, and (b) 1D concentration profiles across the layer interfaces.

APT was performed to unveil compositional effects behind the structural variation of l_{ZrAlN} = 15 nm multilayers as a function of growth temperature. Fig. 7a shows 2D Al concentration maps from 1 nm thick virtual slices of $Zr_{0.43}Al_{0.57}N$ layers perpendicular to the growth direction from the multilayers grown at 700 and 900 °C. The more pronounced segregation for T_s = 900 °C is evident by a larger domain size and a higher frequency of AlN-rich domains. The average composition ratios (Al : Zr) evaluated by proximity histogram (not shown here) were 0.9 and 0.3 for the *w*-AlN- and *c*-ZrN- rich domains, respectively. The

values indicate that the AlN-rich domains are relatively pure compared to ZrN- rich domains. Previous studies on TiAlN reveal that the segregation in metallic sublattice has a significant influence on the stability of metastable cubic phase connected with differences in the electronic structure, bond energy and configurational contribution to the total energy, by reducing the number of transition metal -Al bonds [40].

The APT 1D profiles in Fig. 7b show interface widths of approximately 4 nm in the 700 and 900 °C multilayers. The intermixed layer is comparable to what was observed in short period multilayers and thus, indicates that the interface width is an atomic mixing caused by the ion-bombardment during growth and the difference in growth temperature is too small to affect the intermixing. The interface topography analysis of $Zr_{0.43}Al_{0.57}N$ layers shows that the bottom interface is rougher compared to the top interface in both multilayers, which is likely caused by a faceted columnar growth of TiN layers.

3.4 Interface chemistry and crystallography after annealing

The STEM analysis (Fig. 8a) of the multilayer l_{ZrAlN} =15 nm (T_s = 900 ° C) after isothermal annealing at 1150 °C for 2 hours shows a lateral coalescence of AlN domains (dark contrast) to approximately 20 nm in size surrounded by ZrN (bright contrast) in the lateral and TiN (grey contrast) in the growth direction. The $Zr_{0.43}Al_{0.57}N$ displays a decrease in the layer thickness from 15 nm in the as-deposited state to 5 nm after annealing. A comparison of EDX line spectra of the as-deposited and annealed film (Fig. 8b) shows that ZrN and TiN interdiffuse. However, due to higher volume fraction of the TiN layer, out diffusion of ZrN is dominant, leaving behind AlN as the main constituent in the original $Zr_{0.43}Al_{0.57}N$ layer, which explains the decrease in layer thickness.

An APT reconstruction in Fig. 8c shows the formation of pure AlN with intermittent ZrN domains and out diffusion of ZrN from the $Zr_{0.43}Al_{0.57}N$ layer. The AlN (red) domains distribution is presented in the reconstruction with Al ions and the ZrN (blue) domain distribution is presented with ZrN complex ions, respectively, to avoid showing spatial artifacts in the reconstruction originating from minor peak overlaps of Zr^{+3} and TiN^{+2} ions in the mass spectrum. A relatively higher volume fraction of

ZrN at the bottom interface is visualized in the reconstruction and also in the isoconcentration surfaces created for the top and bottom interfaces of the $Zr_{0.43}Al_{0.57}N$ layers shown in Fig. 8d.

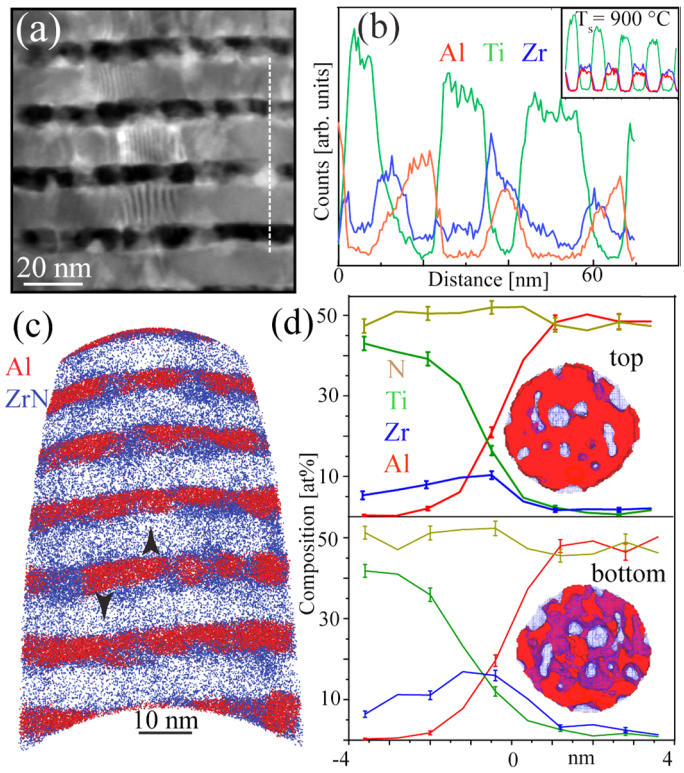

Figure 8: Analysis of l_{ZrAlN} =15 nm (900°C) multilayer after isothermal annealing. (a) STEM image,(b) EDX line profile, inset image shows profile of as-deposited multilayer, (c) reconstructed APT tip, (d), proxigrams of TiN/AlN top and bottom interface, inset images shows isoconcentration surface of Al 30 at% (red, solid) and ZrN 20 at% (blue, wireframe). Black arrows in (c) indicate top and bottom interfaces for proximity histogram construction.

Proximity analysis across the AlN domian interfaces (Fig. 8d), shows concentration gradient of Zr with an average value of 10 ± 1 and 16 ± 1 at%, resulting in $Ti_{0.8}Zr_{0.2}N$ and $Ti_{0.68}Zr_{0.32}N$ compositions at the top and bottom interface respectively (interfaces are marked with arrows). We attribute this to the presence of columnar boundaries near the faceted TiN surface (i.e., bottom interfaces with relatively higher topographical roughness in the as deposited multilayers) providing shorter path for Zr diffusion.

SAED pattern of the annealed multilayer in Fig. 9 shows confined reflections of cubic and wurtzite phases identical to the as deposited multilayer (see Fig. 6d). This is an important result indicating that the semicoherent interfaces of *w*-AlN are stable even after isothermal annealing. The faint c-111 reflections seen in the as-deposited multilayer, however, become intense after annealing. The combination of HRTEM, FFT, SAED pattern, and our previous plan-view image analysis [18] reveal two different interface coherency relations(Fig. 9c-d):

Type I : *c*-ZrN $_{(110)[001]}$ ‖ *w*-AlN $_{(10\text{-}10)[001]}$, exist in both as deposited and annealed multilayers, and

Type II: *c*-TiN $_{(111)[1\text{-}10]}$ ‖ *w*-AlN $_{(0001)[11\text{-}20]}$, which forms only in small amounts (faint *c*-111 reflection) during deposition and grows in extent during annealing.

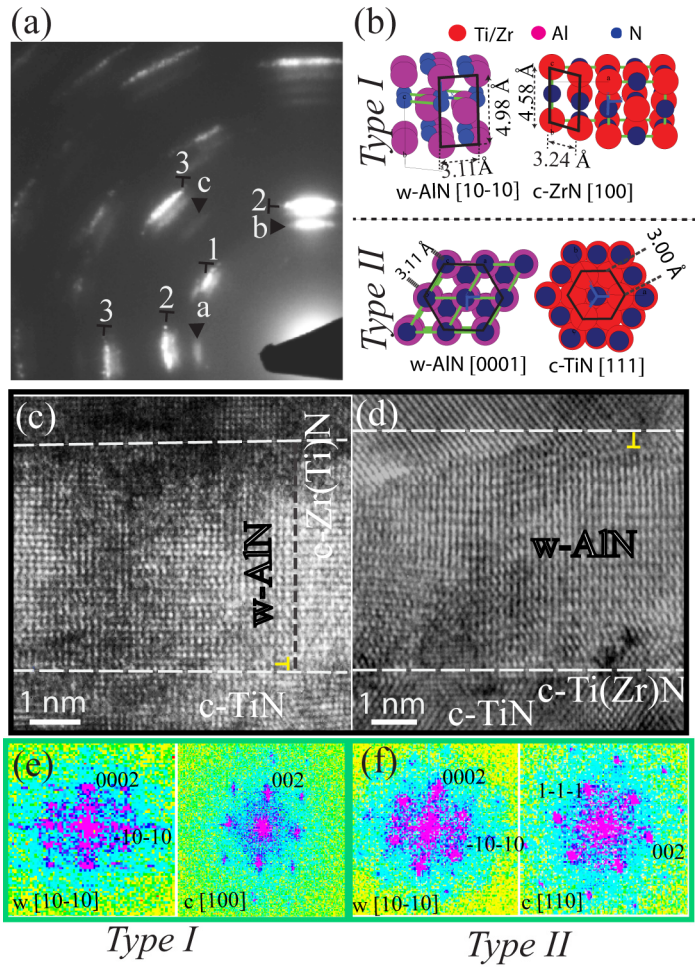

Figure 9: Type I and Type II Interface structure of multilayer shown in Fig. 8. (a) SAED pattern, where annotation 1, 2 and 3 mark c-111, 200, 220, and a, b and c mark w-10-10, 0002, 10-12 reflection. (b) visualization of the two interfaces, (c-d) HR-TEM images and (e-f) corresponding FFT of the two interface types.

The crystallographic details of the two semicoherent interfaces are visualized in Fig.9b with *c*-110 ‖ *w*-10-10 (*type I*) and *c*-111 ‖ *w*-0001 (*type II*) having the same crystallographic in plane symmetry. The analysis also explains the origins of the XRD-peaks at 35.77° and 39.65° of the annealed multilayer (see. Fig. 2) to be domains with *type II* and *type I* interfaces, respectively. The lattice resolved image display misfit dislocations between the hetrostructural domains (Fig. 9c and d). The dislocation density is comparable in spite of significant difference in the misfit strain between type I (~ 8%) and type II (~ 3.6 %) interfaces. This indicates that the hetrostructural domains with type I interfaces are kept in high stress state.

3.5 *Ab-initio* Thermodynamic stability of the interfaces

First-principles calculations were performed to evaluate the interfacial energies of TiN/AlN and ZrN/AlN bicrystals using the multilayer models shown in Fig. 1(a-d). The results in Fig.10 show that the relative energy difference is low between isostructural coherent interfaces with (100) and (111) orientations for both TiN/AlN and ZrN/AlN. For hetrostructural semicoherent interfaces we infer that the *Type I* is favorable for ZrN/AlN interfaces but not for TiN/AlN, whereas *type II* interfaces are energetically the most favorable ones for both material systems. The calculations also reveal that semicoherent *c*-TMN/*w*-AlN structural archetypes have higher

thermodynamic stability compared to isostructural coherent interfaces, i.e. *c*-TMN/*c*-AlN. This underlines the experimental observation of a high thermal stability of the film, l_{ZrAlN} = 15 nm, when it contains semicoherent interfaces.

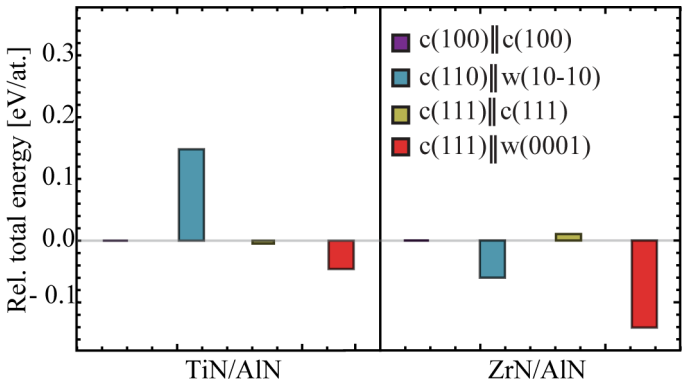

Figure 10: Ab-initio calculated total energy divided by 192 atoms (eV/atom) relative to c-(100)[001]//c-(100)[001] for TiN/AlN and ZrN/AlN multilayer.

The common in-plane lattice parameter of the multilayer and the strain values calculated in each layer are listed in table 2. In the case of TiN/AlN, the strain values are largest for *type I*, followed by isostructural interfaces and smallest for *type II* interfaces. For ZrN/AlN, the largest strain is found for isostructural interfaces, followed by *type I* and smallest for *type II* interfaces. It is to be noted that the higher thermodynamic stability of a *type II* interface is related to the lower misfit strain, combined with the fact that the AlN is in its stable wurtzite structure. Accordingly, the structural misfit and the bulk free energy can be suggested as a measure to predict the relative thermodynamic stabilities in chemically modulated structures containing different coherent interface structures.

Interface structure	Common in-plane lattice parameter, Å		% Strain TiN	% Strain AlN	% Strain ZrN	% Strain AlN
	TiN/AlN	ZrN/AlN	TiN/AlN		ZrN/AlN	
c-(100)//c-(100)	4.18	4.45	-1.42	1.46	-2.79	8.01
c-(110)//w-(10-10) Type 1	4.37	4.63	3.07	-12.25	1.14	-7.03
c-(111)//c-(111)	2.94	3.08	-2	0.89	-4.94	5.69
c-(111)//w-(0001) Type 2	3.06	3.2	2	-1.61	-1.23	2.89

Table 2: Ab-initio calculated in-plane common lattice parameter and the strain in different layers as a function of interface structure variation for TiN/AlN and ZrN/AlN multilayer.

3.6 Mechanical properties

Fig. 11a shows the variation in H and E of the monolithic and multilayered films as a function of $Zr_{0.43}Al_{0.57}N$ layer thicknesses for T_s = 700 °C. The trend for E follows closely the rule-of-mixture of monolithic TiN with a value of 458± 15 GPa and $Zr_{0.43}Al_{0.57}N$ with a value of 220±7 GPa. A high hardness is measured for the short period coherenet interface containing multilayers with a maximum value of 35±2

GPa for l_{ZrAlN} =5 nm. In contrast, the long period multilayers with incoherent interfaces display a monotonic hardness drop as a function of $Zr_{0.43}Al_{0.57}N$ layer thickness.

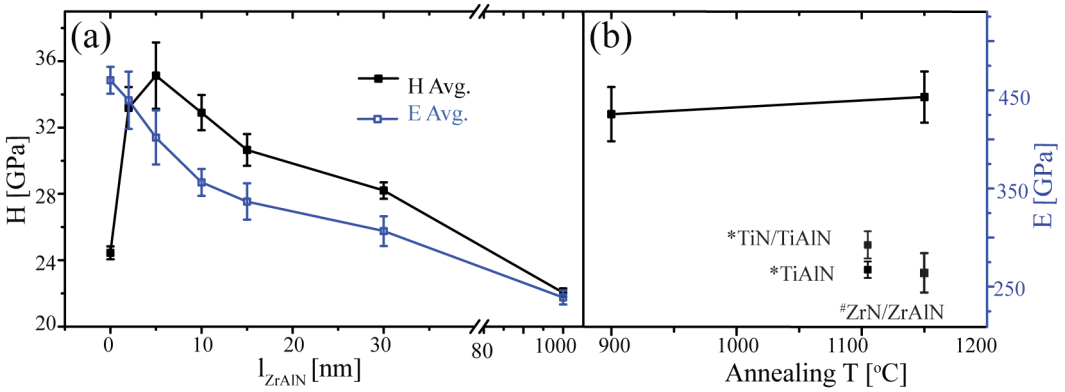

*Figure 11: H, E of monolithic and multilayers. (a) Films grown at 700 °C, (b) multilayers with d_{ZrAlN} 15 nm grown at 900 °C and isothermally annealed at 1150 °C. Ref. values: *TiN/TiAlN, TiAlN [6], #ZrN/ZrAlN [30].*

However, the multilayer l_{ZrAlN} =15 nm deposited at 900 °C, consisting semicoherent interfaces, shows a higher hardness (Fig. 11 b) in its as-deposited state. More importantly, this multilayer display a stable H value of 34 ± 1.5 GPa, after isothermal annealing at 1150 °C. We ascribe the stable hardness of the annealed films to the thermally stable semicoherent interfaces between *w*-AlN and *c*-TiN, *c*-ZrN.

4. Discussion:

The current study is an investigation of the crystal and interface structure of TiN/ZrAlN multilayers grown at temperatures between 700 and 900 °C. TiN attains a stable cubic (B1) structure and due to a close lattice match grows epitaxially on MgO [41]. Immiscible $Zr_{0.43}Al_{0.57}N$ on the other hand segregates into ZrN and AlN-rich domains during the growth. Here, the growth temperature corresponds to ~ 0.4 of the melting temperature, which sets the average adatom diffusion lengths to a few nm for the current deposition rates [42]. This results in a nanocomposite structure of ZrN and AlN.

In the TiN/$Zr_{0.43}Al_{0.57}N$ multilayers, the segregated AlN- rich domains form coherent, semicoherent, and incoherent interfaces with TiN and ZrN depending on the thickness of ZrAlN layer and the growth temperature. Interestingly, the semicoherent *w*-AlN/*c*-TMN interfaces display significantly high thermal stability with a stable hardness compared to the monolithic films and multilayers of TiAlN and ZrAlN forming incoherent interfaces [15,43]. The mechanisms governing the

different interface structure formation and their effects on thermal and mechanical stability are discussed here.

4.1 Influence of T_s and l_{ZrAlN} on crystal and interface structure

From the APT analysis of the long period multilayers, incorporation of approximately 10 at% Zr in AlN-rich domains and ~ 30 at% Al in ZrN-rich domains is determined. This suggests that the substrate temperature of 700 °C enables segregation within the $Zr_{0.43}Al_{0.57}N$ layers, however insufficient adatom mobility at the growth front limits the formation of pure binaries. The high solute amount in ZrN- rich domains leads to a distorted structure, whereas the lower solute concentration in the AlN- rich domains enable it to forms its stable wurtzite structure (Fig. 3d). The resulting nanocomposite of *w*-AlN and distorted ZrN forms incoherent interfaces both in monolithic film and in long period multilayers.

The short period multilayers ($l_{ZrAlN} \leq 5$ nm) on the other hand, consist of coherent interfaces. This is a direct consequence of metastable *c*-AlN domain formation. The stabilization of metastable *c*- AlN with a layer thickness between 2 and 5 nm in an epitaxial multilayer structure is attributed to the interface energy dominating the bulk free energy and strain energies [26,44]. The interface energy minimization is achieved by adapting the crystal structure of AlN layer to that of the underlying *c*-TiN layer and thus forming a low energy coherent interface. However, the chemical gradients constitute a significant portion of the multilayer, as observed in the case $l_{ZrAlN} \leq 5$ nm (Fig. 5). This has a favorable effect on the stabilization of metastable *c*-AlN rich domains by reducing the structural misfit with the templating TiN layer and ZrN-rich domains. Hence, we suggest that the metastable phase formation in the short period multilayers is a combined effect of chemical intermixing and epitaxial stabilization. An additional favorable factor is the segregation in metallic sublattice that reduces the number of Zr-Al bonds which might favor the metastable cubic phase stabilization of ZrAlN similar to what has been shown for TiAlN [40].

Beyond the critical layer thickness i.e. $l_{ZrAlN} > 10$ nm, the template effect is lost and AlN domains assume its stable wurtzite structure with incoherent interfaces to the distorted ZrN domains similar to the monolithic films. This leads to termination of epitaxial growth between the layers of ZrAlN and TiN.

A transition from the incoherent to semicoherent interfaces between *w*-AlN and the cubic phases (TiN and ZrN) in the long period multilayers is obtained by increasing the growth temperature to 900 °C. The semicoherent interfaces form because: (i) higher deposition temperature leads to a more pronounced segregation within the $Zr_{0.43}Al_{0.57}N$ layers (Fig. 7a), which reduces the solute induced distortion causing ZrN-rich domains to attain a cubic crystal structure, and (ii) the higher growth temperature provides sufficient adatom mobility for TiN and ZrN to attain 002 orientation in the growth direction and thus favouring semicoherent interfaces between *c*-ZrN (110) and *w*-AlN (10-10), driven by the interface energy minimization. These two surfaces have similar in plane symmetry (Fig. 9b).

The importance of the material selection to promote semicoherent interfaces with *w*-AlN is noticeable here. For example, studies on TiAlN/MgO (001) performed under similar growth conditions as used in this study showed segregated domains of *c*-TiN and *w*-AlN with incoherent interfaces [45]. Our calculations also confirm higher thermodynamic stability of the coherent interfaces between *w*-AlN (10-10) and *c*-ZrN (110) compared to *c*-TiN (110), as the later one generates relatively higher misfit strain.

In addition, the orientation of *w*-AlN (0001) and *c*-ZrN (002) in the growth direction, also minimize the growth front (film-vacuum interface) surface energy. Subsequently, the nanoscale domains of *c*-ZrN/*w*-AlN grow simultaneously by adapting a *coupled growth* similar to what has been observed for directionally solidified eutectic systems for a wide range of materials [46]. This results in a chemically modulated structure (Fig. 6e) with non-isostructural semicoherent interfaces between *c*-ZrN and *w*-AlN inherited across the TiN layer and form *type 1* interfaces with a misfit strain of 7 %.

Further reduction of the strain energy occur through a competitive *type II* interface formation where the *c*-TiN (111) grows epitaxial to *w*-AlN (0001) with a misfit strain of 4 %. The MgO (001) surface promotes *type I* interfaces and the evolution of *type II* interfaces is attributed to a higher thermodynamic stability in agreement with the theoretical predictions.

4.2 Thermal stability of semicoherent interfaces

The thermal stability is an important criteria to qualify semicoherent interface structural archetype for elevated temperature applications. The competition between the strain and interface energy, bulk free energy sets a critical domain size, above which the semicoherency is likely to breakdown. At elevated temperature, coalescence of *w*-AlN results in larger domains which may lead to semicoherency breakdown to relive the strain energy. For the isostructurally decomposed c-TiN and c-AlN, the critical domain size for coherency breakdown is ~15 nm [47]. This relatively small critical size is an effect of *c*-AlN being a metastable phase with an energy penalty of 0.18 eV/atom with respect to its thermodynamic equilibrium structure [48]. In contrast, for the semicoherent *w*-AlN domains in the TiN/ZrAlN multilayer, the only driving force for the coherency breakdown stems from the strain energy. Therefore, the critical size of *w*-AlN domains to commence coherency breakdown is expected to be significantly larger and consequently results in higher thermal stability of the interfaces.

In short, the retained coherency at the interfaces after isothermal annealing at 1150 °C in the TiN/ZrAlN multilayers is ascribed to: (i) relatively higher thermodynamic stability of semicoherent *type 1* interfaces compared to the isostructural interfaces, (ii) evolution of *type II* interfaces to lower the strain energy of the film, (iii) inter-diffusion between ZrN and TiN generating compositionally graded interfaces to further reduces the misfit strain for *type II* interface as the in-plane lattice parameter misfit between *c*-Ti(Zr)N (111) and *w*-AlN (0001) becomes smaller, and (iv) constrained coalescence of *w*-AlN domains by confining them between the immiscible cubic phases both in the growth and lateral directions, thereby keeping the domains smaller than the critical size.

Previous first principle calculations at 0 K indicate that the TiN-ZrN material system is immiscible with positive enthalpy of mixing in the tune of 0.06 eV/atom [49–51] asociated with a lattice mismatch about 7%. However, the current study reveals interdiffusion between TiN and ZrN during elevated temperature annealing. At the annealing temperature of 1150 °C, it is likely that the entropy of mixing (ΔS_{mix}) supersedes the enthalpy of mixing (ΔH_{mix}), thus the miscibility gap closes and provides the thermodynamic drive for the intermixing. This analysis is in line with the recent theoretical predictions [24] and previous observation by Rogström et

al.[52]. This is further complementary to the experimentally observed high thermal stability of TiZrN alloy over wide composition range in spite of the calculated positive enthalpy of mixing [51].

4.3 Influence of interface structure on the mechanical properties

Monolithic $Zr_{0.43}Al_{0.57}N$ shows significantly lower H and E compared to the rest of the films. The lower hardness is likely caused by a coordinated shear displacement, similar to what has been shown for the nanostructured TMN thin films with incoherent interfaces [53,54]. The lower elastic modulus is a combined effect of higher volume fraction of *w*-AlN phase which has a higher compliance compared to cubic TiN and AlN [22] , and also that the distorted ZrN domains cause elastic softening similar to nanostructured metals [55].

The hardness varies systematically in the multilayers upon varying the $Zr_{0.43}Al_{0.57}N$ layer thickness (Fig. 11a). For the short period multilayers consisting coherent interfaces the spatial fluctuation in elastic properties across the layers and within the $Zr_{0.43}Al_{0.57}N$ layer offer Koehler [56] strengthening while the lattice misfit between the isostructural coherent interfaces results in coherency hardening [57]. Both strengthening mechanisms become more prominent for the multilayers with 5 nm $l_{ZrAlN,}$ resulting in the highest H value of 35±2 GPa.

The long period multilayers ($l_{ZrAlN} \geq 10$ nm) display a decrease in H as a function of $Zr_{0.43}Al_{0.57}N$ layer thickness. Here the incoherent interfaces between the nanoscale segregated domains of *w*-AlN and distorted ZrN domains offer relatively lower shear resistance similar to the monolithic $Zr_{0.43}Al_{0.57}N$ film. For the multilayers l_{ZrAlN} =15 nm, grown at 900 °C, the evolution of semicoherent interfaces between *w*-AlN and *c*-TMN domains (Fig. 6f) make them more resistant to the coordinated shear displacement which results in higher hardness (Fig. 11b). The key significance of these multilayer structures is that the hardness (34 ± 1.5 GPa) is stable even after isothermal annealing at experimentally constrained temperature of 1150 °C and further high temperature studies are needed to probe the ultimate thermal endurance limit of the semicoherent structure.

We suggest that the thermally stable semicoherent interfaces between *w*-AlN and *c*-TMN domains offer both Koehler and coherency hardening similar to the isostructural interfaces between *c*-TiN and *c*-AlN. In addition, the non-isostructural semicoherent interfaces provide an additional obstacles to dislocation glide due to the

misorientation between the active glide planes *c*-TiN {110} and *w*-AlN $\{0001\},\{10\bar{1}1\}$ [58,59]. A high hardness combined with the relatively low elastic modulus of the *c*-TMN/*w*-AlN structural archetypes is likely to cause superior wear resistance similar to what has been observed for other hard coatings [60].

5. Conclusions

Multilayer structures consisting TiN and $Zr_{0.43}Al_{0.57}N$ nanocomposite layers were grown using magnetron sputtering on MgO (001) substrates. The interfaces between the layers and between ZrN and AlN domains were tuned from coherent, semicoherent to incoherent, by varying the multilayer design and the growth temperature.

AlN-rich domains assume a metastable cubic structure in the multilayers with $l_{ZrAlN} \leq 5$ and the stable wurtzite structure in the multilayers with $l_{ZrAlN} > 10$ nm and in the monolithic film. The metastable phase formation in the short period multilayers is suggested to be a combined effect of chemical intermixing and epitaxial stabilization, yielding multilayers with high hardness.

For the wurtzite phase containing films the growth temperatures around 700 °C are found to be inadequate to obtain complete segregation within ZrAlN layer and the presence of Al in the ZrN-rich domains causes a distorted ZrN structure, which leads to the formation of incoherent interfaces between ZrN domains and the *w*-AlN lattice. Higher growth temperature of 900 °C facilitates pronounced segregation of *w*-AlN and *c*-ZrN domains, and the interface energy minimization of the nanoscale modulated structure leads to evolution of semicoherent interfaces between *w*-AlN and cubic phases (TiN and ZrN). Two types of coherency relations are found, where $c\text{-ZrN}_{(110)[001]} \parallel w\text{-AlN}_{(10\text{-}10)[001]}$ interfaces are promoted by a MgO (001) template effect and the $c\text{-TiN}_{(111)[10\text{-}1]} \parallel w\text{-AlN}_{(0001)[11\text{-}20]}$ interfaces are promoted by the higher thermodynamic stability.

The semicoherent interfaces offer both Koehler and coherency hardening mechanisms. Due to higher thermodynamic stability of the interface structures and limited domain growth of *w*-AlN provided through confinement between TiN layers and ZrN domains, the coherency and thus the hardness retains at ~ 34 ± 1.5 GPa after elevated temperature annealing.

These findings show the potential of improving the shear strength of materials by modifying the interface structure between the thermodynamically stable *c*-TMN-*w*-

AlN phases. We believe that in parallel to the efforts of improving the stability of metastable phases, the approach of designing thermally stable multiphase materials with tailored interface structures provides a complete new dimension for thin film materials to be used at elevated temperatures.

Acknowledgements

The Swedish research council (VR grant no 621- 2012-4401), Swedish Foundation for Strategic Research (SSF) through the program MultiFilms (RMA08-0069), Swedish government strategic research area grant in material science AFM – SFO MatLiU (2009-00971), EU's Erasmus Mundus graduate school in Material Science and Engineering (DocMASE), the Swedish Governmental Agency for Innovation Systems (Vinnova grants VINNMer 2011-03464 and M – Era.net 2013-02355), are gratefully acknowledged for their financial support. The EU-funded project AME-Lab (European Regional Development Fund C/4-EFRE-13/2009/Br) is acknowledged for the FIB/SEM use. The APT was financed by the DFG and the federal state government of Saarland (INST 256/298-1 FUGG).

References:

[1] W. D. Münz, Titanium aluminum nitride films: A new alternative to TiN coatings, J. Vac. Sci. Technol. A. 4 (1986) 2717.

[2] S. Paldey, S.C. Dee, Single layer and multilayer wear resistant coatings of (Ti,Al) N : a review, Mater. Sci. Eng. A. 342 (2003) 58–79.

[3] M.I. Yousaf, V.O. Pelenovich, B. Yang, C.S. Liu, D.J. Fu, Effect of bilayer period on structural and mechanical properties of nanocomposite TiAlN/MoN multilayer films synthesized by cathodic arc ion-plating, Surf. Coatings Technol. 282 (2015) 94–102.

[4] P.H. Mayrhofer, D. Music, J.M. Schneider, Ab initio calculated binodal and spinodal of cubic $Ti_{1-x}Al_xN$, Appl. Phys. Lett. 88 (2006) 071922.

[5] A. Hörling, L. Hultman, M. Odeń, J. Sjo̲leń, L. Karlsson, Thermal stability of arc evaporated high aluminum-content $Ti_{[1-x]}Al_{[x]}N$ thin films, J. Vac. Sci. Technol. A. 20 (2002) 1815.

[6] P.H. Mayrhofer, A. Hörling, L. Karlsson, J. Sjo̲leń, T. Larsson, C. Mitterer, L. Hultman, Self-organized nanostructures in the Ti–Al–N system, Appl. Phys. Lett. 83 (2003) 2049.

[7] A. Knutsson, J. Ullbrand, L. Rogström, N. Norrby, L.J.S. Johnson, L. Hultman, J. Almer, M. P. Johansson Jöesaar, B. Jansson, M. Odén, Microstructure evolution during the

isostructural decomposition of TiAlN- A combined in-situ small angle x-ray scattering and phase field study, J. Appl. Phys. 113 (2013) 213518.

[8] P.E. Hovsepian, D.B. Lewis, W.D. Münz, Recent progress in large scale manufacturing of multilayer/superlattice hard coatings, Surf. Coatings Technol. 133-134 (2000) 166–175.

[9] D. Music, R.W. Geyer, J.M. Schneider, Recent progress and new directions in density functional theory based design of hard coatings, Surf. Coatings Technol. 286 (2016) 178–190.

[10] H.W. Hugosson, H. Högberg, M. Algren, M. Rodmar, T.I. Selinder, Theory of the effects of substitutions on the phase stabilities of $Ti_{1-x}Al_xN$, J. Appl. Phys. 93 (2003) 4505–4511.

[11] F. Rovere, D. Music, S. Ershov, M. Baben, H. Gerd fuss,P.H. Mayrhofer, J.M. Schneider, Experimental and computational study on the phase stability of Al- containing cubic transition metal nitrides, J. Phys. D: Appl. Phys. 43 (2010) 035302.

[12] L. Chen, D. Holec, Y. Du, P.H. Mayrhofer, Influence of Zr on structure, mechanical and thermal properties of Ti-Al-N, Thin Solid Films. 519 (2011) 5503–5510.

[13] R. Rachbauer, A. Blutmager, D. Holec, P.H. Mayrhofer, Effect of Hf on structure and age hardening of Ti-Al-N thin films, Surf. Coatings Technol. 206 (2012) 2667–2672.

[14] F. Wang, I.A. Abrikosov, S.I. Simak, M. Odén, F. Mücklich, F. Tasnádi, Coherency effects on the mixing thermodynamics of cubic $Ti_{1-x}Al_xN$/TiN(001) multilayers, Phys. Rev. B. 93 (2016) 174201.

[15] A. Knutsson, M.P. Johansson, L. Karlsson, M. Odén, Thermally enhanced mechanical properties of arc evaporated $Ti_{[0.34]}Al_{[0.66]}N$/TiN multilayer coatings, J. Appl. Phys. 108 (2010) 044312.

[16] R. Forsén, N. Ghafoor, M. Odén, Coherency strain engineered decomposition of unstable multilayer alloys for improved thermal stability, J. Appl. Phys. 114 (2013) 244303.

[17] Q. Xia, H. Xia, A.L. Ruoff, Pressure-induced rocksalt phase of aluminum nitride: A metastable structure at ambient condition, J. Appl. Phys. 73 (1993) 8198.

[18] N. Ghafoor, L.J.S. Johnson, D.O. Klenov, J. Demeulemeester, P. Desjardins, I. Petrov, L. Hultman, M. Odén, Nanolabyrinthine ZrAlN thin films by self-organization of interwoven single-crystal cubic and hexagonal phases, APL Mater. 1 (2013) 022105.

[19] A. Karimi, G. Allidi, R. Sanjines, Relative orientation of the constituents on the degree of crystallographic coherence in AlN/TiN superlattices, Surf. Coatings Technol. 201 (2006) 4062–4067.

[20] D. Rafaja, A. Poklad, V. Klemm, G. Schreiber, D. Heger, M. Šíma, M. Dopita, Some consequences of the partial crystallographic coherence between nanocrystalline domains in

Ti–Al–N and Ti–Al–Si–N coatings, Thin Solid Films. 514 (2006) 240–249.

[21] K. Yalamanchili, I.C. Schramm, E. Jiménez-Piqué, L. Rogström, F. Mücklich, M. Odén, N. Ghafoor, Tuning hardness and fracture resistance of ZrN/$Zr_{0.63}Al_{0.37}N$ nanoscale multilayers by stress-induced transformation toughening, Acta Mater. 89 (2015) 22–31.

[22] A.J. Wang, S.L. Shang, Y. Du, Y. Kong, L.J. Zhang, L. Chen, D.D Zhao, Z.K. Liu, Structural and elastic properties of cubic and hexagonal TiN and AlN from first-principles calculations, Comput. Mater. Sci. 48 (2010) 705–709.

[23] M. Wen, H. Huang, K. Zhang, Q. Meng, X. Li, L. Kong, C. Hu, W. Zheng, The AlN layer thickness dependent coherent epitaxial growth, stress and hardness in NbN/AlN nanostructured multilayer films, Surface. Coatings Technol. 235 (2013) 367-375.

[24] H. Lind, R. Pilemalm, L. Rogström, F. Tasnadi, N. Ghafoor, R. Forsén, L.J.S. Johnson, M.P. Johansson-Jöesaar, M. Odén, I.A. Abrikosov, High temperature phase decomposition in TixZryAlzN, AIP Adv. 4 (2014) 127147.

[25] D. Holec, R. Rachbauer, L. Chen, L. Wang, D. Luef, P.H. Mayrhofer, Surface & Coatings Technology Phase stability and alloy-related trends in Ti – Al – N , Zr – Al – N and Hf – Al – N systems from fi rst principles, Surf. Coat. Technol. 206 (2011) 1698–1704.

[26] A. Madan, I.W. Kim, S.C. Cheng, P. Yashar, V.P. Dravid, S.A. Barnett, Stabilization of Cubic AlN in Epitaxial AlN -TiN Superlattices, Phy. Rev. Let. 78 (1997) 1743–1746.

[27] C. Stampfl, A.J. Freeman, Structure and stability of transition metal nitride interfaces from first-principles: AlN/VN, AlN/TiN, and VN/TiN, Appl. Surf. Sci. 258 (2012) 5638–5645.

[28] M. Schlögl, B. Mayer, J. Paulitsch, P.H. Mayrhofer, Influence of CrN and AlN layer thicknesses on structure and mechanical properties of CrN/AlN superlattices, Thin Solid Films. 545 (2013) 375–379.

[29] N. Ghafoor, F. Eriksson, P.O.Å. Persson, L. Hultman, J. Birch, Effects of ion-assisted growth on the layer definition in Cr/Sc multilayers, Thin Solid Films. 516 (2008) 982–990.

[30] M.S. Janson, CONTES Conversion of Time-Energy Spectra—a program for ERDA data/analysis. Internal report, Uppsala University, 2004.

[31] M.K. Miller, K.F. Russell, Atom probe specimen preparation with a dual beam SEM/FIB miller, Ultramicroscopy. 107 (2007) 761–6.

[32] P. Bas, A. Bostel, B. Deconihout, D. Blavette, A general protocol for the reconstruction of 3D atom probe data, Appl. Surf. Sci. 87-88 (1995) 298–304.

[33] P.E. Blöchl, Projector augmented-wave method, Phys. Rev. B. 50 (1994) 17953–17979.

[34] G. Kresse, Efficient iterative schemes for ab initio total-energy calculations using a plane-

wave basis set, Phys. Rev. B. 54 (1996) 11169–11186.

[35] J.P. Perdew, K. Burke, M. Ernzerhof, Quantum Theory Group Tulane University, Generalized Gradient Approximation Made Simple, Phys. Rev. Lett. 77 (1996) 3865–3868.

[36] J.D. Pack, H.J. Monkhorst, Special points for Brillouin-zone integrations, Phys. Rev. B. 16 (1977) 1748–1749.

[37] W.C. Oliver, G.M. Pharr, Measurement of hardness and elastic modulus by instrumented indentation: Advances in understanding and refinements to methodology, J. Mater. Res. 19 (2011) 3–20.

[38] B.M. Howe, E. Sammann, J.G. Wen, T. Spila, J.E. Greene, L. Hultman, I. Petrov, Real-time control of AlN incorporation in epitaxial $Hf_{1-x}Al_xN$ using high-flux, low-energy (10–40eV) ion bombardment during reactive magnetron sputter deposition from a $Hf_{0.7}Al_{0.3}$ alloy target, Acta Mater. 59 (2011) 421–428.

[39] PDF-card No. 01-073-7288. JCPDS- International centre for diffraction data, 1998.

[40] P.H. Mayrhofer, D. Music, J.M. Schneider, Influence of the Al distribution on the structure, elastic properties, and phase stability of supersaturated $Ti_{1-x}Al_xN$, J. Appl. Phys. 100 (2006) 094906.

[41] L. Hultman, U. Helmersson, S.A. Barnett, J.E. Sundgren, J.E. Greene, Low-energy ion irradiation during film growth for reducing defect densities in epitaxial TiN(100) films deposited by reactive-magnetron sputtering, J. Appl. Phys. 61 (1987) 552.

[42] D.G. Sangiovanni, D. Edström, L. Hultman, I. Petrov, J.E. Greene, V. Chirita, Ti adatom diffusion on TiN(001): Ab initio and classical molecular dynamics simulations, Surf. Sci. 627 (2014) 34–41.

[43] L. Rogström, L.J.S. Johnson, M.P. Johansson, M. Ahlgren, L. Hultman, M. Odén, Thermal stability and mechanical properties of arc evaporated ZrN/ZrAlN multilayers, Thin Solid Films. 519 (2010) 694–699.

[44] V. Chawla, D. Holec, P.H. Mayrhofer, Stabilization criteria for cubic AlN in TiN/AlN and CrN/AlN bi-layer systems, J. Phys. D. Appl. Phys. 46 (2013) 045305.

[45] F. Adibi, I. Petrov, L. Hultman, U. Wahlström, T. Shimizu, D. McIntyre, J.E. Greene, J.E. Sundgren, Defect structure and phase transitions in epitaxial metastable cubic $Ti_{0.5}Al_{0.5}N$ alloys grown on MgO(001) by ultra-high-vacuum magnetron sputter deposition, J. Appl. Phys. 69 (1991) 6437–6450.

[46] J. Llorca, V.M. Orera, Directionally solidified eutectic ceramic oxides, Prog. Mater. Sci. 51 (2006) 711–809.

[47] N. Norrby, L. Rogström, M.P. Johansson-Jõesaar, N. Schell, M. Odén, In situ X-ray

scattering study of the cubic to hexagonal transformation of AlN in $Ti_{1-x}Al_xN$, Acta Mater. 73 (2014) 205–214.

[48] V. Chawla, D. Holec, P.H. Mayrhofer, The effect of interlayer composition and thickness on the stabilization of cubic AlN in AlN / Ti – Al – N superlattices, Thin Solid Films. 565 (2014) 94–100.

[49] V. Ivashchenko, S. Veprek, A. Pogrebnjak, B. Postolnyi, First-principles quantum molecular dynamics study of $Ti_x Zr_{1-x} N(111)/SiN_y$ heterostructures and comparison with experimental results, Sci. Technol. Adv. Mater. 15 (2014) 025007.

[50] G. Abadias, V.I. Ivashchenko, L. Belliard, P. Djemia, Structure, phase stability and elastic properties in the $Ti_{1-x}Zr_xN$ thin-film system: Experimental and computational studies, Acta Mater. 60 (2012) 5601–5614.

[51] A. Hörling, J. Sjölén, H. Willmann, T. Larsson, M. Odén, L. Hultman, Thermal stability, microstructure and mechanical properties of $Ti_{1-x}Zr_xN$ thin films, Thin Solid Films. 516 (2008) 6421–6431.

[52] L. Rogström, N. Ghafoor, M. Ahlgren, M. Odén, Auto-organizing ZrAlN/ZrAlTiN/TiN multilayers, Thin Solid Films. 520 (2012) 6451–6454.

[53] Z.B. Qi, P. Sun, F.P. Zhu, Z.C. Wang, D.L. Peng, C.H. Wu, The inverse Hall-Petch effect in nanocrystalline ZrN coatings, Surf. Coatings Technol. 205 (2011) 3692–3697.

[54] K. Yalamanchili, R. Forsén, E. Jiménez-Piqué, M.P. Johansson Jöesaar, J.J. Roa, N. Ghafoor, M. Odén, Structure, deformation and fracture of arc evaporated Zr–Si–N hard films, Surf. Coatings Technol. 258 (2014) 1100–1107.

[55] P. Sharma, S. Ganti, On the grain-size-dependent elastic modulus of nanocrystalline materials with and without grain-boundary sliding, J. Mater. Res. 18 (2011) 1823–1826.

[56] J.S. Koehler, Attempt to Design a Strong Solid, J. Phys. Rev. B 2 (1970) 547.

[57] J.W. Cahn, Hardening by spinodal decomposition, Acta Metal. 11 (1963) 1275.

[58] M. Odén, H. Ljungcrantz, L. Hultman, Characterization of the Induced Plastic Zone in a Single Crystal TiN(001) Film by Nanoindentation and Transmission Electron Microscopy, J. Mater. Res. 12 (1997) 2134–2142.

[59] S.R. Jian, Y.C. Tseng, I.J. Teng, J.Y. Juang, Dislocation Energetics and Pop-Ins in AlN Thin Films by Berkovich Nanoindentation, Materials. 6 (2013) 4259–4267.

[60] Y.X. Ou, J. Lin, H.L. Che, J.J. Moore, W.D. Sproul, M.K. Lei, Mechanical and tribological properties of CrN/TiN superlattice coatings deposited by pulsed dc magnetron sputtering, Surf. Coatings Technol. 276 (2015) 152-159.

Annexure 1

Exploring high entropy alloy design in (AlTiVNbCr)N alloy

K. Yalamanchili, F. Wang, I.C. Schramm, J.M. Andersson, M.P. Johansson Jöesaar, F. Tasnadi, N.Ghafoor, M. Odén,

Submitted

Exploring the high entropy alloy concept in (AlTiVNbCr)N

K. Yalamanchili[1], F. Wang [1,2], I.C. Schramm [1,2], J.M. Andersson [3], M.P. Johansson Jöesaar[1,3], F. Tasnádi[1], F. Mücklich [2], N. Ghafoor[1], and M. Odén[1]

1. Department of Physics, Chemistry, and Biology (IFM), Linköping University, Linköping, Sweden.

2. Functional Materials, Department of Materials Science, Saarland University, Saarbrucken, Germany.

3. Seco Tools AB, SE 737 82 Fagersta, Sweden

Absract

We have explored the high entropy alloy (HEA) concept in a transition metal-aluminum-nitride (TM-Al-N) material system. We show that the (AlTiVNbCr)N alloys synthesized by a reactive arc deposition process is closely an ideal cubic solid solution with positive mean-field enthalpy of mixing of the order of 0.06 eV/atom. Entropy stabilization is predicted to make the solid solution thermodynamically stable relative to the binary nitrides at temperatures above 1000 K. However, the annealing experiments show that the solid solution decomposes to w-AlN and c-(TiVNbCr)N at a temperature above 1100 K. The limited thermal stability of the solid solution is investigated in relation to several thermodynamic parameters. Finally we suggest that the HEA designed multiprincipal element TM-Al-N solid solution, is rather in a metastable state.

Graphical abstract

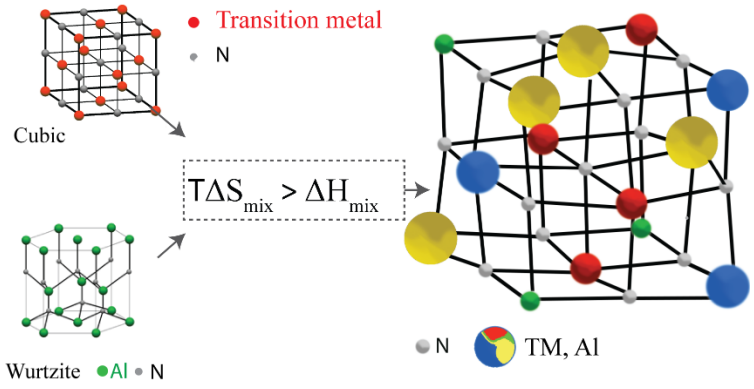

Graphical representation of entropy stabilized solid solution between immiscible c-TMN and w-AlN

High entropy alloys (HEA), defined as multiprincipal element alloys consisting of at least 5 elements, each with concentrations between 5 and 35 at. % [1], are reported to have fascinating structural and mechanical properties [2,3].

Yeh et al. proposed that the configurational entropy of mixing in a metallic alloy consisting of at least five principal elements is considerably higher than the enthalpy of their intermetallic compounds [4]; and therefore the formation of a solid solution is favored via a decrease in Gibbs free energy of mixing ΔG_{mix}.

$$\Delta G_{mix} = \Delta H_{mix} - T\Delta S_{mix} \quad (1)$$

where, ΔH_{mix} is enthalpy of mixing, ΔS_{mix} is entropy of mixing, and T is temperature. This concept has received great attention, and resulted in an upsurge of synthetic efforts to realize metallic multiprincipal high entropy alloys [5].

Recent studies report entropy stabilized solid solution formation between the non-isostructural oxides of MgO, CoO, NiO, CuO and ZnO with an estimated positive enthalpy of mixing of about 0.1 eV/atom [6]. This suggests that the HEA design concept might be extended to ceramic materials such as carbides, nitrides and oxides by having a multielement metallic sublattice, and here we have explored this possibility in transition metal nitrides.

Transition metal nitrides (TMN) are important materials with a wide range of applications from wear resistant coatings [7] to micromechanical devices for energy storage, and energy harvesting [8,9]. Forming a thermally stable solid solution through the HEA design concept in an alloy with positive enthalpy of mixing such as TM-Al-N may have significant technological impact, especially for high temperature applications. Transition metal nitrides such as TiN, CrN, VN, and NbN have cubic B1 structure under ambient conditions and the ΔH_{mix} between these isostructural TMN is relatively low [10]. The equilibrium structure of AlN at ambient conditions is wurtzite B4 structure and it has a high interaction energy to c-TMN resulting in a positive ΔH_{mix} with a value between 0.06 and 0.15 eV/atom [11] depending on the material system. However, if a multiprincipal element TM-Al-N alloy is formed, the high configurational entropy may overcome the positive enthalpy of maxing, and an entropy stabilized solid solution might be achieved at elevated temperature. This is schematically illustrated in the graphical abstract.

Previously, several thin films multicomponent TMN alloys have been formed as single phase cubic solid solutions and studied in terms of microstructure and mechanical property evolution

[12–15]. However, detailed thermal stability studies and thermodynamic assessments of their single phase solid solutions with respective to their enthalpy and entropy of mixing is lacking.

In the current study, the HEA design is explored in two different single phase solid solution alloys of (AlTiCrVNb)N. The alloys are synthesized in thin film form by a reactive arc deposition process. Both alloys have comparable configurational entropy, but the Al concentration is varied to tune their enthalpies. A complete thermodynamic assessment of such (quasi-) quinary solid solution should include at least 10^4 competing reference states [16], considering a coarse mesh of 10 at. % difference in any one of the element to distinguish between two different states. Hence, a preliminary thermodynamic assessment of the solid solution is performed with respect to their binaries. The calculation suggests relatively high thermodynamic stabilities for the solid solutions above 1000 K. This is experimentally tested by extracting the films from their substrates and subjecting the resulting powder to isothermal annealing experiments up to 1573 K. The resulting structures are then characterized by X-ray diffractometry (XRD) and atom probe tomography (APT). These results are further complemented with thermal analysis (DSC) of both alloys in comparison to a binary alloy that has a similar mixing enthalpy, but a lower configurational entropy. Experimental and computational details are provided in the supplement.

Table 1 shows the composition and mean-field thermodynamic properties for both alloys. The composition is shown only for the metallic sublattice, and the nitrogen content is found to be close to stoichiometric. The 0 K mixing enthalpy value ΔH^0_{mix} for the (quasi-) quinary cubic solid solution is calculated relative to their binaries of cubic TiN, VN, CrN and NbN and wurtzite AlN. See supplementary materials for details and Ref. [sup.10] for justifying the approximation of $\Delta H_{mix} \approx \Delta H^0_{mix}$ in nitride alloys. The configurational entropy of mixing is calculated as, $\Delta S_{conf.} = -R \sum_{i=1}^{n} Xi \ln Xi$, where R is the gas constant, Xi the molar fraction of i^{th} element, and n is the total number of constituent elements. Calculations result in positive ΔH_{mix} for both alloys with respect to their binaries.

	Al, at. %	Ti, at. %	V, at. %	Cr, at. %	Nb, at. %	ΔH^0_{mix}, eV/atom	Temperature in K, where $T\Delta S_{conf.} > \Delta H_{mix}$,
Alloy 1	17.4	40.2	14.4	3.8	24.2	0.06	700
Alloy 2	31.1	33.50	12.53	5.48	17.4	0.10	1000

Table 1. Composition and calculated thermodynamic parameters

However, the estimated value of $T\Delta S_{conf.}$ is higher than ΔH_{mix} at temperatures above 700 K and 1000 K respectively for alloy 1 and alloy 2. This indicates a possibility of entropy stabilized solid solution as shown in graphical abstract. Note that the enthalpy of mixing for both alloys is lower than the previously reported HEA oxide [6]. Figure 1. shows XRD profiles and the averaged lattice parameter extracted from diffraction lines corresponding to 111, 200, 220, 311 and 222 lattice planes of alloy1 and 2 in both the as deposited and annealed states. Both alloys show only cubic diffraction peaks in the as deposited state, suggesting a cubic crystalline solid solution. The measured lattice parameter in the as deposited state is 4.23 Å, and 4.20 Å that is close to the estimated lattice parameters by Vegard's law of 4.24 Å and 4.22 Å for alloy 1 and 2, respectively.

After high temperature annealing, the diffractograms display low intensity peaks of *w*-AlN, and the cubic peaks shift to lower diffraction angles at a temperature above 1100 °C for both alloys. This indicates that the cubic solid solutions decompose. The measured lattice parameters (Fig. 1c) reflect these structural changes, i.e. an abrupt increase in lattice parameter at annealing temperatures between 900 and 1100 °C and at 1300 °C and a constant value is reached suggesting that the decomposition is completed. Based on the fact that this (quasi-) quinary solid solution, characterized with high configurational entropy and having a $\Delta H_{mix.}$ lower than that of the entropy stabilized oxide alloy [6], the observed decomposing is unexpected.

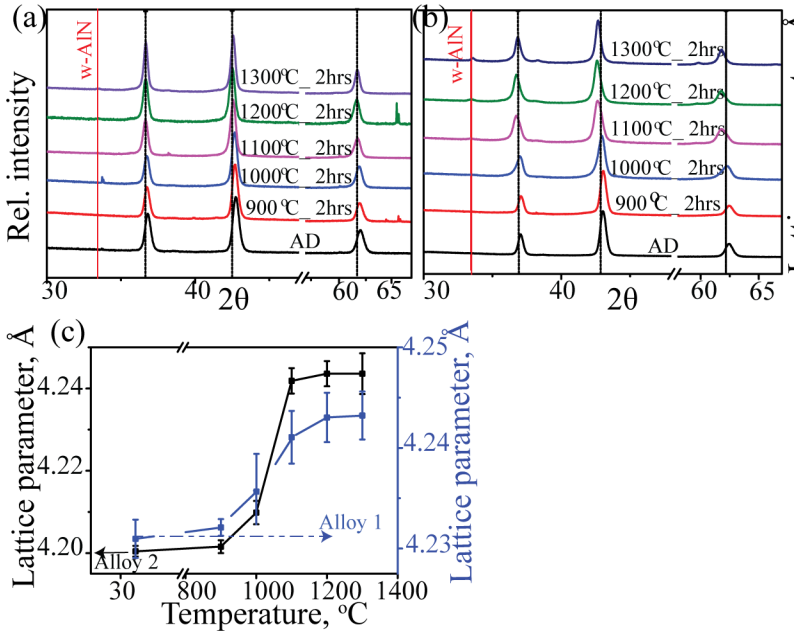

Figure 1. X-ray diffractogram (a, b) and extracted lattice parameters (c) of alloy 1 (a), and 2 (b), in the as deposited (AD) and annealed states. The dotted line in Fig. a and b corresponds to the calculated peak positions of the cubic solid solution by Vegard's law.

Possible explanations for this behavior could be (a) a lower value of $S_{conf.}$ of the alloy compared to our estimations, (b) the HEA design concept is incompletely described in terms of competing phases with higher thermodynamic stability, and (c) other entropy contributions offsetting the configurational entropy effects. The relative contribution of the individual factors are discussed in the following section.

a) Reduced value of $S_{conf.}$

Previous studies suggest that the value of $S_{conf.}$ may be reduced in the fabricated alloy compared to the estimated value due to a deviation from a random atomic distribution [17]. Furthermore, a maximum configurational entropy is expected for an equimolar alloy [18], which is not the case in the current study. The contribution of both these factors are evaluated by atom probe analysis.

Figure 2a. shows a reconstructed atom probe tip of the as deposited alloy 1, revealing no cluster formation in the measured volume of 80 x 60 x 60 nm^3. This is further complemented with the frequency distribution analysis of the alloying elements that matches closely with a standard binomial function (Fig. 2b). The deviation from the binomial distribution is further quantified by the Pierson coefficient μ [19], with a value close to 0 for all the elements on the metallic sublattice, indicating a random solid solution.

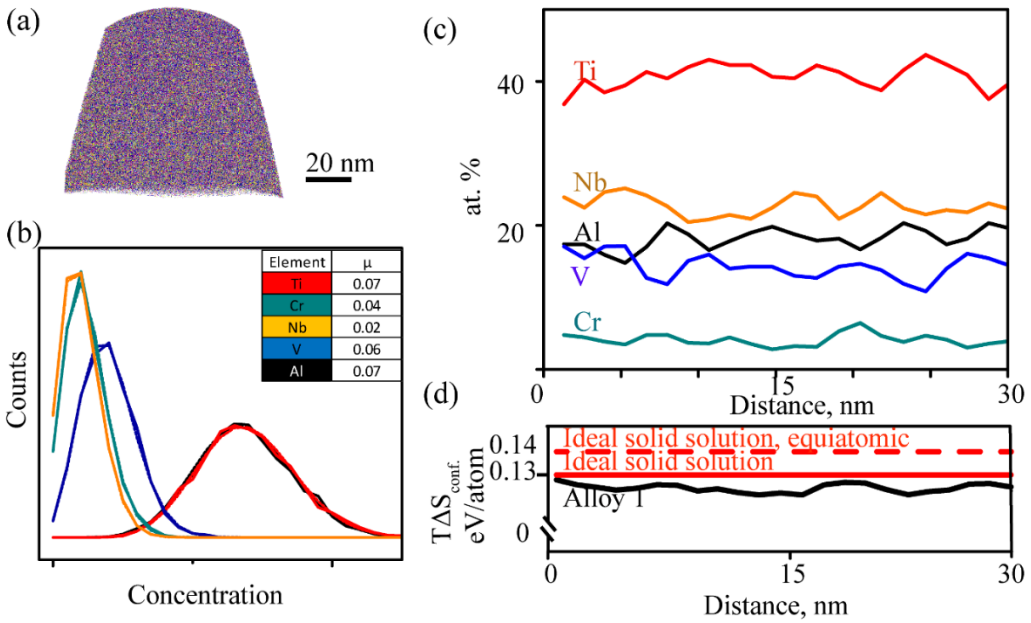

Figure 2. Multicomponent alloy 1, (a) reconstructed APT tip, (b) frequency distribution analysis of single ion elements in the as deposited state, (c) 1D line concentration profile (nitrogen not included), and (d) estimated $T\Delta S_{conf.}$ at 1000 K.

Figure 2c shows 1D line concentration profile of individual elements, from which $T\Delta S_{conf.}$ of the alloy is estimated at a temperature of 1000 K and compared with an ideal solid solution having the same composition (Fig. 2d). The data reveals that the estimated value of $T\Delta S_{conf.}$ of alloy 1 is 92% of the ideal solid solution and hence we rule out the possibility of a reduced value of $T\Delta S_{conf.}$ caused by a deviation from the ideal solution as a contributing factor for the observed decomposition. Furthermore, the difference in $T\Delta S_{conf.}$ between an equiatomic alloy and the nonequiatomic alloy 1 is only 0.015eV/atom at 1000 K. Therefore, the deviation of the multiprinicipal element alloy composition from the equiatomic concentration cannot explain the decomposition of the solid solution. A similar situation exists for alloy 2 as expected from their similar growth conditions.

b) Competing phases with higher thermodynamic stability

Thermodynamic assessment of all the 10^4 competing phases is not practical as previously mentioned. Instead, the decomposed alloy composition is evaluated by APT analysis and the thermodynamic parameters are compared between the solid solution and the decomposed state for both alloys.

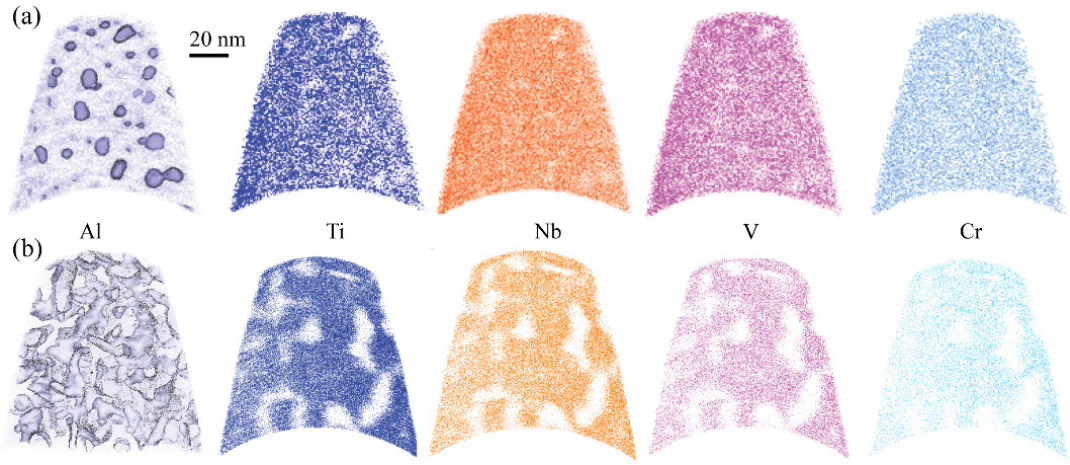

Figure 3. APT reconstruction (5 nm thin slice), revealing elemental distribution after annealing at 1100 °C, 2hrs for (a) alloy 1, and (b) alloy 2. For Al, APT analysis also shows isoconcentration surface at 25 at. %.

Figure 3. shows 5 nm thin slices of an APT reconstruction, visualizing the elemental distribution of alloy 1 and 2 after being subjected to annealing at a temperature of 1100 °C. The APT analysis reveals precipitation of AlN in a homogeneous solid solution of TiN, VN, CrN, and NbN. XRD analysis (Fig. 1) shows that the AlN domains are formed in the wurtzite structure, while the solid solution is retained the cubic structure. We also note that the decomposition is more prominent for alloy 2 with large domains of AlN, attributed to its higher positive enthalpy

of mixing. The AlN in alloy 2 forms elongated domains interconnected in a network, which is different compared to the isolated spherical morphology in alloy 1.

The APT compositional analysis (only metallic sublattice) of the decomposed alloy is extracted from the proximity histograms and shown in table 2 for the two different phases. At 1100 ^{o}C, the TMN alloy has a considerable amount of Al and the AlN-precipitates contains all the other elements. In contrast, at 1300 ^{o}C they are almost pure indicating their equilibrium state. This is in agreement with the measured lattice parameter of the cubic phase that reaches steady state at 1300 ^{o}C (Fig. 1c). The impurity level in w-AlN domains is measured to 3 at. % and the amount of AlN in cubic phase is 4 at. %. This is comparable to the previously reported equilibrium solubility limit of 2 at. % of AlN in TiN at 1073 K [20]. These observations underlines that the solubility of AlN in TMN alloy is not considerably affected by its higher configurational entropy.

Temperature	Alloy	Location	Al, at. %	Ti, at. %	Nb, at. %	V, at. %	Cr, at. %
1100 ^{o}C	Alloy 1	AlN	0.87	Cum. 0.13			
		TMN	0.07	0.44	0.28	0.17	0.04
	Alloy 2	AlN	0.96	Cum. 0.04			
		TMN	0.12	0.46	0.23	0.13	0.06
1300 ^{o}C	Alloy 1	AlN	0.96	Cum.0.04			
		TMN	0.03	0.48	0.28	0.16	0.05
	Alloy 2	AlN	0.96	Cum.0.04			
		TMN	0.03	0.48	0.24	0.17	0.08

Table 2: Composition of TMN, and AlN domains extracted from APT analysis at annealing temperatures of 1100 ^{o}C and 1300 ^{o}C

To evaluate the thermodynamic driving force for the precipitation of w-AlN the configurational entropy and reduced free energy, estimated as $G_{red.} = H - TS_{conf.}$, are compared between the solid solution and the decomposed state, i.e., for a mixture of w-AlN and c-(Ti,Nb,V,Cr)N with a composition extracted from the APT analysis at 1300 ^{o}C. The results are shown for the two alloys as a function of temperature in Fig.4. The difference in $TS_{conf.}$ for both alloys at a temperature about 1200 ^{o}C (Fig. 4a, b) are of the order of 0.02 eV/atom. This is less than the mixing enthalpy differences between the (quasi-) quinary solid solution and the decomposed state, which are calculated to be 0.07 and 0.1 eV/atom for alloy 1 and alloy 2, respectively. As a consequence, $G_{red.}$ is lower for the decomposed state in both alloys, providing a thermodynamic driving force for the decomposition of the solid solution. This analysis shows that the thermodynamic stability of a multielement solid solution based on HEA design is not

set by the absolute value of entropy, as originally proposed [4], but rather by the difference in the entropy value between the competing phases in relation to their mixing enthalpy.

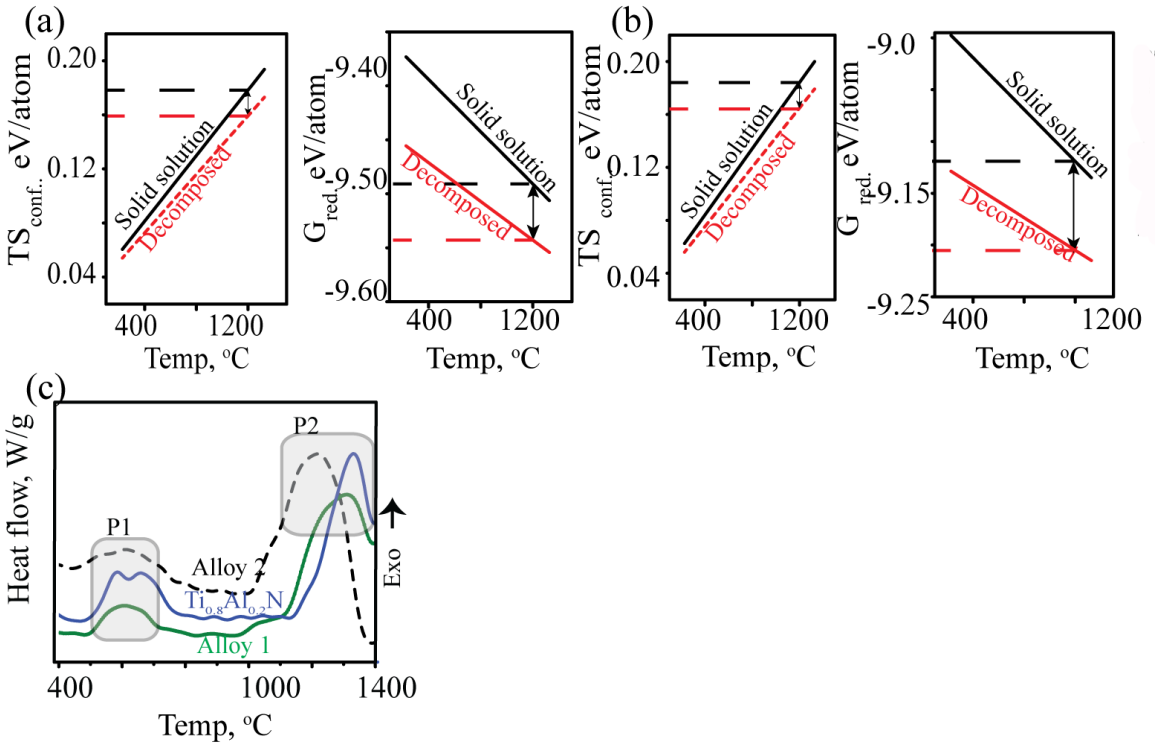

Figure 4. *Comparison of thermodynamic parameters between solid solution and decomposed states as a function of temperature for (a) alloy 1, (b) alloy 2, and (c) DSC signal for different alloys. Arrows in Fig. a and b with the dotted line are for visual reference to compare the thermodynamic parameters at 1200 °C.*

Here, we also note that after the decomposition, a (quasi-) quaternary cubic solid solution of c-(TiNbVCr)N is formed with minor concentration of AlN present. Its ΔH_{mix} with respect to the binaries is estimated to only 0.01 for both alloys.

To probe the effect of configurational entropy on the phase stability of the solid solution explicitly, thermal analysis is performed for alloy 1 and 2, and compared to the (quasi-) binary alloy of $Ti_{0.8}Al_{0.2}N$ alloy with a calculated ΔH^0_{mix} value of 0.08 eV/atom which is slightly higher than alloy1.

Figure 4c. shows differential scanning calorimetry (DSC) traces from alloy 2, alloy 1, and $Ti_{0.8}Al_{0.2}N$ using a heating rate of 20 °C/min. The DSC traces display two distinct exothermic reactions: the first peak at 600 °C is ascribed to defect annihilation and crystal recovery in line with the previous studies [22,23], and the second peak around 1200 °C to w-AlN precipitation. The latter is based on the chemical and structural changes observed during annealing by APT and XRD analysis. The transformation of AlN from its metastable cubic phase to stable wurtzite

phase is associated with an energy gain of 0.18 eV/atom [21], thus giving an exothermic peak in the DSC trace.

The temperatures corresponding to the maximum of peak 1 are similar for all the three alloys. In contrast, the maximum of peak 2 is alloy dependent, i.e. a temperature of 1220 ^{o}C, 1320 ^{o}C, and 1330 ^{o}C for alloy 2, alloy 1, and $Ti_{0.8}Al_{0.2}N$, respectively. The lower temperature for alloy 2 is explained by the higher difference in $G_{red.}$ between the solid solution and the decomposed alloy (Fig. 4) that provides a higher driving force for decomposition compared to alloy 1. Surprisingly, the temperatures corresponding to maximum precipitation of w-AlN are comparable between alloy 1 and $Ti_{0.8}Al_{0.2}N$ in spite of their significant difference in $S_{conf.}$ (1.41 and 0.5 K_B/atom, respectively, where K_B is the Boltzmann constant). These results further emphasize that the thermodynamic stability of the multicomponent solid solution is not govern by its absolute value of $S_{conf.}$ Instead the difference in $S_{conf.}$ between competing microstates in relation to ΔH_{mix} determines the stability. It means that for alloy 1 the decomposition reaction (AlTiVCrNb)N $\rightarrow$(TiVCrNb)N+ AlN is driven by lowering ΔH_{mix} by 0.07 eV/atom while reducing $S_{conf.}$ by 0.15 K_B/atom. In contrast, the decomposition reaction of TiAlN$\rightarrow$ TiN + AlN is driven by lowering ΔH_{mix} by 0.08 eV/atom while reducing $S_{conf.}$ by 0.23 K_B/atom. Note that the difference in $S_{conf.}$ between the solid solution and decomposed states is lower for the (quasi-) quinary alloy, thus offering a lower entropy stabilization of the solid solution compared to the (quasi-) binary alloy of TiAlN which is not expected from their absolute value of $S_{conf.}$

c) Other entropy contributions offsetting the configurational entropy effects:

The original HEA design concept is based on the assumption that the configurational entropy dominates over other entropy contributions in a multiprincipal element alloy [24]. However, recent studies indicate that vibrational entropy play a considerable role in determining the phase stabilities [25]. The precise estimation of vibrational entropy ($S_{vib.}$) for multicomponent alloys is an exhausting task at the moment. Instead the $S_{vib.}$ dependence on bulk modulus (B) based on the Debye-Grüneisen model [25] is used to compare the relative difference between the solid solution and the decomposed alloy. The model predicts a higher value of $S_{vib.}$ for the alloy with higher B values [25]. Table 3 shows calculated B values for the solid solution and the decomposed state for both the alloys. In case of alloy 1, the decomposed state has a higher $S_{vib.}$ compared to the solid solution, thereby offsetting the configurational entropy effects. Alloy 2 has a higher $S_{vib.}$ in the solid solution, indicating that it complements the configurational entropy.

	Bulk modulus of solid solution K, GPa	Bulk modulus of the decomposed alloy K, GPa
Alloy 1	240	249
Alloy 2	264	250

Table 3: Comparison of bulk modulus between solid solution and decomposed state

The results neither support nor rule out the possibility of $S_{vib.}$ offsetting $S_{conf.}$ but it shows that even in the case when $S_{vib.}$ is complementing $S_{conf.}$ (alloy 2), a solid solution decomposition is observed. Furthermore, recent first principle calculations of TiAlN and ZrAlN have shown that the region of miscibility gap shrinks when $S_{vib.}$ component is included in the calculations, indicating that the solid solution is characterized with high $S_{vib.}$ compared to the decomposed state for a wide range of Al concentrations [26]. The above analysis shows that the (quasi-) quinary solid solution decomposes even when vibrational entropy is enhancing the entropy of mixing.

In summary, even though the alloys of (AlTiVCrNb)N are grown with a nearly random solid solution with a value of $S_{conf.}$ close to 92 % of an ideal solid solution and when other entropy contributions such as $S_{vib.}$ are considered, keeping AlN in the cubic solid solution is unlikely under the thermodynamic conditions for the compositions studied here. Instead, the alloy transforms toward a global equilibrium configuration in such a way that the internal energy is reduced significantly with only a slight reduction in the configurational entropy by precipitating AlN in its stable wurtizte structure and retaining the solid solution between the TMN components with a low mixing enthalpy. This underlines that the thermodynamic stability of the multicomponent element solid solution based on the HEA design is not govern by the absolute value of the entropy as it was proposed originally [4]. Instead the decisive factor is the difference in the entropy value between the competing phases in relation to their enthalpy of mixing.

Finally, the entropy stabilized solid solution formation in a multicomponent alloy with positive enthalpy of mixing is only possible when the solid solution is located at the global minima in the free energy landscape. This situation is material specific, and might be the case for the previously reported entropy stabilized oxide alloy in spite of its high positive enthalpy of mixing. In contrast, for the TM-Al-N material system studied here, the (quasi-) quinary solid solution with $\Delta H_{mix} > 0.06$ is only a metastable state, and a competing microstate with a lower

free energy is readily available in the form of equilibrium mixture of w-AlN and c-(TiCrVNb)N.

Acknowledgements

The Swedish research council (VR grant no 621- 2012-4401), Swedish Foundation for Strategic Research (SSF) through the program MultiFilms (RMA08-0069), Swedish government strategic research area grant in material science AFM – SFO MatLiU (2009-00971), EU's Erasmus Mundus graduate school in Material Science and Engineering (DocMASE), the Swedish Governmental Agency for Innovation Systems (Vinnova grants VINNMer 2011-03464 and M – Era.net 2013-02355), are gratefully acknowledged for their financial support. The EU-funded project AME-Lab (European Regional Development Fund C/4-EFRE-13/2009/Br) is acknowledged for the FIB/SEM use. The APT was financed by the DFG and the federal state government of Saarland (INST 256/298-1 FUGG).

References:

[1] L.S. Zhang, G.L. Ma, L.C. Fu, J.Y. Tian, Recent Progress in High-Entropy Alloys, Adv. Mater. Res. 631-632 (2013) 227–232.

[2] Y. Zhang, T. Ting, Z. Tang, M.C. Gao, K.A. Dahmen, P.K. Liaw, Z.P. Lu, Microstructures and properties of high-entropy alloys, Progress in Materials Science 61 (2014) 1–93.

[3] Y. Zhang, T. Zuo, Y. Cheng, P.K. Liaw, High-entropy alloys with high saturation magnetization, electrical resistivity, and malleability, Sci. Rep. 3 (2013) 1455.

[4] J.W. Yeh, S.K. Chen, S.J. Lin, J.Y. Gan, T.S. Chin, T.T. Shun, C.H. Tsau, S.Y. Chang, Nanostructured High-Entropy Alloys with Multiple Principal Elements: Novel Alloy Design Concepts and Outcomes, Adv. Eng. Mater. 6 (2004) 299–303.

[5] Y.F. Ye, Q. Wang, J. Lu, C.T. Liu, Y. Yang, High-entropy alloy: Challenges and prospects, Mater. Today. 680 (2015) 1-14.

[6] C.M. Rost, E. Sachet, T. Borman, A. Moballegh, E.C. Dickey, D. Hou, J.L. Jones, S. Curtarolo, J.P. Maria, Entropy-stabilized oxides, Nat. Commun. 6 (2015) 8485.

[7] H. Holleck, Material selection for hard coatings, J. Vac. Sci. Technol. A. 4 (1986) 2661.

[8] S. Dong, X. Chen, X. Zhang, G. Cui, Nanostructured transition metal nitrides for energy storage and fuel cells, Coord. Chem. Rev. 257 (2013) 1946–1956.

[9] P. Eklund, S. Kerdsongpanya, B. Alling, Transition-metal-nitride-based thin films as novel energy harvesting materials, J. Mater. Chem. C. (2016).

[10] L. Zhou, D. Holec, P.H. Mayrhofer, Ab initio study of the alloying effect of transition metals on structure, stability and ductility of CrN, J. Phys. D. Appl. Phys. 46 (2013) 365301.

[11] B. Alling, T. Marten, I.A. Abrikosov, A. Karimi, Comparison of thermodynamic properties of cubic Cr_{1-x} Al_x N and Ti_{1-x} Al_x N from first-principles calculations, J. Appl. Phys. 102 (2007) 044314.

[12] C. Tsau, Y. Chang, Microstructures and Mechanical Properties of $TiCrZrNbN_x$ Alloy Nitride Thin Films, Entropy. (2013) 5012–5021.

[13] C. Lai, M. Tsai, S. Lin, J. Yeh, Influence of substrate temperature on structure and mechanical properties of multi-element (AlCrTaTiZr)N coatings, Surface & Coatings Technology. 201 (2007) 6993–6998.

[14] T.K. Chen, T.T. Shun, J.W. Yeh, M.S. Wong, Nanostructured nitride films of multi-element high-entropy alloys by reactive DC sputtering, Surface & Coatings Technology. 189 (2004) 193–200.

[15] M. Tsai, C. Wang, C. Lai, J. Yeh, J. Gan, Thermally stable amorphous (Al Mo Nb Si Ta Ti V Zr $)_{50}N_{50}$ nitride film as diffusion barrier in copper metallization, Appl. Phy. Let. 052109 (2008) 24–27.

[16] B. Cantor, Multicomponent and high entropy alloys, Entropy. 16 (2014) 4749–4768.

[17] H.K.D.H. Bhadeshia, High entropy alloys, Mater. Sci. Technol. 31 (2015) 1139–1141.

[18] Y. Zhang, Y.J. Zhou, J.P. Lin, G.L. Chen, P.K. Liaw, Solid-solution phase formation rules for multi-component alloys, Adv. Eng. Mater. 10 (2008) 534–538.

[19] M.P. Moody, L.T. Stephenson, A. V. Ceguerra, S.P. Ringer, Quantitative binomial distribution analyses of nanoscale like-solute atom clustering and segregation in atom probe tomography data, Microsc. Res. Tech. 71 (2008) 542–550.

[20] N. Shulumba, O. Hellman, Z. Raza, J. Barrirero, I. A. Abrikosov, F. Mücklich, I.A. Abrikosov, and M. Odén, Anharmonic impact on the solid solubility of the random alloy TiAlN at high temperatures, Phys. Rev. B: 89(2014) 174108.

[21] V. Chawla, D. Holec, P.H. Mayrhofer, The effect of interlayer composition and thickness on the stabilization of cubic AlN in AlN / Ti – Al – N superlattices, Thin solid films. 565 (2014) 94–100.

[22] A. Knutsson, M.P. Johansson, L. Karlsson, M. Odén, Thermally enhanced mechanical properties of arc evaporated $Ti_{0.34}Al_{0.66}N$/TiN multilayer coatings, J. Appl. Phys. 108 (2010) 0–7.

[23] P.H. Mayrhofer, A. Hörling, L. Karlsson, J. Sjölén, T. Larsson, C. Mitterer, L. Hultman, Self-organized nanostructures in the Ti-Al-N system, Appl. Phys. Lett. 83 (2003) 2049–2051.

[24] B.S. Murty, J.W. Yeh, S. Ranganathan, High-Entropy Alloys, first ed., Butterworth-Heinemann (2014) p 20.

[25] D. Ma, B. Grabowski, F. Körmann, J. Neugebauer, D. Raabe, Ab initio thermodynamics of the CoCrFeMnNi high entropy alloy: Importance of entropy contributions beyond the configurational one, Acta Mater. 100 (2015) 90–97.

[26] N. Shulumba, O. Hellman, R. Zamaan, I. Abrikosov, M. Oden, (Unpublished), dissertation no. 1718, Linköping Studies in Science and Technology, 2015.

Supplementary information

Alloy processing: Multiprinicipal element (AlTiVNbCr)N alloy thin films with two different compositions (table 1) on were reactively grown in a 5 Pa N-atmosphere on Fe-substrates in an Oerlikon Balzers Metaplas MZR-323 cathodic arc deposition system using composite $Ti_{0.3}Al_{0.6}Cr_{0.1}$ and $Ti_{0.4}Nb_{0.4}V_{0.2}$ cathodes. In addition, $Ti_{0.8}Al_{0.2}N$ alloys were grown by co-deposition from composite $Ti_{0.5}Al_{0.5}$ and pure Ti cathodes. The substrates were mounted in a vertical row such that plasma mixing from both the cathodes could be used to generate coatings with a range of compositions [REF to a similar set-up, for example [1]. The substrate holder was kept in static condition to suppress the rotation- induced artificial compositional modulation during the growth [2].

The Fe substrates were removed through mechanical polishing and subsequent dissolution in hydrochloric acid (37 %) at a temperature of 90 ^{o}C. The resulting powder of the coating material was then rinsed with deionized water and dried in an oven at 150 ^{o}C overnight.

Thermal stability of the alloys were investigated by isothermal annealing of the powder at 1300 ^{o}C in Ar atmosphere using a heating rate of 50 ^{o}C/min, followed by structural and compositional characterization. Thermal analysis was performed in a Netzsch STA 410 differential scanning calorimeter (DSC) using 25 mg of powder. A run consisted of heating the samples to the maximum temperature 1400 °C with a constant heating rate of 50 °C/min directly followed by cooling to room temperature. Directly after the first heating/cooling cycle an identical cycle was performed, which was used for the baseline correction. All DSC measurements were performed in a 50 ml/min protective Ar flow.

Computational method: We applied first principles calculations to determine the total energy of the *c*-(AlTiVNbCr)N multicomponent alloys and their binaries in their equilibrium structure. The B1-structure 3x3x3 supercells were built using the special quasirandom structure (SQS) approach [3]. We treated the magnetic disorder using a 6-component (Al; Ti; V; $Cr^{\uparrow}$; $Cr^{\downarrow}$; Nb) 216 atoms SQS approximation. The atomic configurations in the supercells were obtained by minimizing the Warren-Cowley pair short-range order (SRO) parameters [4, 5] up to the seventh nearest neighboring shells on the metal sublattice.

The energy calculations were performed using the projector augmented wave (PAW) method [6] within the Vienna Ab initio Simulation Package (VASP) [7-9]. The exchange correlation functional was approximated by the Perdew-Burke-Ernzerhof generalized gradient functional (PBE-GGA) [10]. We applied a plane-wave cutoff energy of 500 eV and the reciprocal-space

integration was performed within the Monkhorst-Pack scheme [11] using k-meshes of (4×4×4). Equilibrium lattice parameter was used to obtain the zero-pressure value of the total energy. Enthalpy of mixing of the alloys were obtained at 0 K, by $E_{c\text{-}(AlTiVNbCr)N} - E_{c\text{-}TiN} + E_{c\text{-}NbN} + E_{c\text{-}VN} + E_{c\text{-}CrN} + E_{w\text{-}AlN,}$ which was projected to finite temperatures up to 1500 K. A similar procedure was used for the $Ti_{0.8}Al_{0.2}N$ alloy. The temperature dependent variation of the calculated mixing enthalpy was considered to be negligible based on the recent studies of TiAlN, and ZrAlN [12]. For each alloy, bulk modulus was extracted by fitting Murnaghan's equation [13] to energy versus volume data from the ab-initio calculations using the VASP.

Characterization: Structural changes of the alloy were characterized by X-ray diffraction (XRD) with a Panalytical Empyrian diffractometer operated in Bragg-Brentano geometry using Cu-K_α radiation. Atom probe tomography (APT) was used to obtain quantitative compositional information in the as deposited state and after isothermal annealing. Atom probe specimen preparations were performed in a FEI dual-beam focused ion beam/SEM workstation implementing the *in situ* lift out technique [14]. A 200 nm thick Pt layer was electron beam deposited on the film surface to reduce Ga implantation during specimen preparation. The measurements were carried out using a LEAP™ 3000X HR CAMECA™ system in laser pulsing mode (532 nm wavelength) with repetition rates of 160 kHz, base temperatures of 40-50 K, and a laser pulse energies of 0.4-0.5 nJ. The data were reconstructed using the standard algorithm developed by Bas et al. [15] and analyzed with the software CAMECA™ IVAS 3.6.8.

References:

1. K. Yalamanchili, R. Forsén, E. Jiménez-Piqué, M.P. Johansson Jöesaar, J.J. Roa, N. Ghafoor, M. Odén, Surf. Coatings Technol. 258 (2014) 1100–1107.
2. A. Eriksson, J.Q. Zhu, N. Ghafoor, M.P. Johansson, J. Sjölén, J. Jensen, M. Odén, L. Hultman, J. Rosén, Surf. Coat. Technol. 205 (2011) 3923.
3. A. Zunger, S. H. Wei, L. Ferreira, and J. Bernard, Phys. Rev. Lett. 65, 353 (1990).
4. I. A. Abrikosov, S. I. Simak, B. Johansson, A. V. Ruban, and H. L. Skriver, Phys. Rev. B 56, 9319 (1997).
5. A. V. Ruban and I. A. Abrikosov, Reports Prog. Phys. 71, 046501 (2008).
6. P. E. Blöchl, Phys. Rev. B 50, 17953 (1994).
7. G. Kresse and J. Hafner, Phys. Rev. B 47, 558 (1993).
8. G. Kresse and J. Hafner, Phys. Rev. B 49, 14251 (1994).
9. G. Kresse and J. Furthmuller, Phys. Rev. B 54, 11169 (1996).

10. J. P. Perdew, K. Burke, and M. Ernzerhof, Phys. Rev. Lett. 77, 3865 (1996)
11. H. J. Monkhorst and J. D. Pack, Phys. Rev. B 16, 1748 (1976).
12. N. Shulumba, O. Hellman, Z. Raza, J. Barriero, B. Alling, F. Mücklich, I. A. Abrikosov and M. Odén, 2015, arXiv:1503.02459.
13. Poirier J.P, Introduction to the Physics of the Earth's Interior, Cambridge University Press, Cambridge, 1991.
14. M.K. Miller, K.F. Russell, Atom probe specimen preparation with a dual beam SEM/FIB miller, Ultramicroscopy. 107 (2007) 761–6
15. P. Bas, A. Bostel, B. Deconihout, D. Blavette, A general protocol for the reconstruction of 3D atom probe data, Appl. Surf. Sci. 87-88 (1995) 298–304.